TRACKING GALAXY GROWTH DURING THE PAST 11 BILLION YEARS WITH DEEP NEAR INFRARED SURVEYS

A Dissertation

by

ADAM R. TOMCZAK

Submitted to the Office of Graduate and Professional Studies of
Texas A&M University
in partial fulfillment of the requirements for the degree of

DOCTOR OF PHILOSOPHY

Chair of Committee,	Kim-Vy H. Tran
Co-Chair of Committee,	Casey J. Papovich
Committee Members,	Lucas M. Macri
	Wolfgang Bangerth
Head of Department,	George Welch

August 2015

Major Subject: Physics

ABSTRACT

Using observations from the FourStar Galaxy Evolution Survey (ZFOURGE), we obtain the deepest measurements to date of the galaxy stellar mass function (SMF) at $z < 3$. With these data, we find evidence for a steepening of the slope at the low-mass end of the SMF at $z \leq 2$, a feature that had only been identified at $z \leq 1$. These measurements also allow us for the first time to observe a rapid buildup of low-mass quiescent galaxies and help to constrain the growth rates of galaxies.

We next explore star-formation histories (SFHs) of galaxies based on the evolution of the correlation between the star-formation rate and stellar mass of galaxies (SFR$-M_*$) and compare to the buildup of stellar mass predicted from the evolution of the SMF. By integrating along the SFR$-M_*$ sequence we generate differential SFHs and estimate stellar mass-growth histories. We find that these integrated SFHs are in broad qualitative agreement with the SMF, but that they do disagree in detail. At early times the SFHs suggest mass-growth rates that are as much as 0.5 dex higher than inferred from the stellar mass function.

Lastly, we look into the prevalence of a possible source of feedback preventing star-formation using mid-IR data from the *Spitzer* Space Telescope with established color selection criteria to identify galaxies hosting active galactic nuclei (AGN). Of the 949 cluster galaxies in our IR-detected sample we identify 12 that are consistent with hosting AGN. We thus measure the fraction of cluster galaxies that host an IR-AGN for a magnitude-limited subsample ($f_{\rm IR-AGN}$) to be $\approx 0.6\%$ with a strong upper limit of 3.4% at the 99% confidence level at $z < 1$. Our results suggest that $f_{\rm IR-AGN}$ in massive galaxy clusters is not strongly correlated with star formation at $z < 1$, and that IR-AGN have a more prominent role at $z > 1$.

ACKNOWLEDGEMENTS

First and foremost I'd like to express my gratitude for my graduate advisor Kim-Vy Tran; you helped transform me from an inexperienced post-undergraduate student into a capable independent researcher. I'd also like to extend a special thanks to Casey Papovich who acted as an effective co-advisor to me at times. I'll always remember that time you turned a "yes-or-no" question into an hour-long discussion about statistics and random sampling.

My thanks go out to the ZFOURGE Collaboration for all their support and guidance through the majority of the work that this dissertation entails. In particular I'd like to thank Ivo Labbé for all the wisdom he imparted to me ranging from the small, such as versioning your data, to the complex, such as Principal Component Analysis and Nyquist sampling. I'd also like to thank Ryan Quadri for being a dedicated mentor throughout much of my work; among many things, you taught me the invaluable skill of self-scrutiny when it comes to one's own work which I hope to carry on with my to the future. Also thanks for refining my knowledge on how `EAZY` and `FAST` work after I crudely tried to teach myself. Special thanks also to Caroline Straatman, not only for creating the data catalogs on which most of this dissertation is based, but also in personally explaining to me how to use them properly. Other ZFOURGE'rs I'd like to recognize: Lee Spitler, Glenn Kacprzak, Michael Cowley, Karl Glazebrook, Rebecca Allen, Lalitwadee Kawinwanichakij, Nicola Mehrtens, Themiya Nanayakkara, and Glen Rees.

I'd also like to thank Kate Whitaker, Gabe Brammer, and Pieter van Dokkum from the 3D-HST team for their assistance with HST portion of this dissertation and for providing general feedback for the first two chapters.

To my fellow graduate comrades - Brett, Mike, Ryan, Jimmy, Steven, Ben, Heath, Leo, Andrew, Ting, Dan, and Wenlong - thanks for all the good times, and helping me through many of the trials.

Last, but of course not least, I'd like to thank my family - Lidia, Richard, Monika, and Eve - as well as my close hometown friends - Matt, Grant, Marc, and Sam - for all of their support during the many years that I spent traversing graduate school and preventing me from being overly engulfed by academia.

To anyone that I might have forgotten, my apologies, but thank you too.

NOMENCLATURE

AB	Absolute Bolometric
ACS	Advanced Camera for Surveys
AGES	AGN and Galaxy Evolution Survey
AGN	Active Galactic Nucleus
CANDELS	Cosmic Assembly Near-IR Deep Extragalactic Legacy Survey
CDF-S	Chandra Deep Field - South
CGM	Circum-Galactic Medium
CMD	Color-Magnitude Diagram
CMR	Color-Magnitude Relation
COSMOS	Cosmic Evolution Survey
EAZY	Easy and Accurate Redshifts from Yale
ELG	Emission Line Galaxy
FAST	Fitting and Assessment of Synthetic Templates
GOODS-S	Great Observatories Origins Deep Survey - South
HST	Hubble Space Telescope
ICM	Intra-Cluster Medium
IMF	Initial Mass Function
IR	Infrared
IRAC	Infrared Array Camera
IRX	Infrared Excess
ISM	Inter-Stellar Medium
kpc	Kiloparsec
MIPS	Multiband Imaging Photometer for Spitzer

MOPHONGO	Multi-Resolution Object Photometry on Galaxy Observations
Mpc	Megaparsec
NDS	Number Density Selection/Selected
NEWFIRM	NOAO Extremely Wide-Field Infrared Imager
NMBS	NEWFIRM Medium Band Survey
NOAO	National Optical Astronomy Observatory
PACS	Photodetecting Array Camera and Spectrometer
PAH	Polycyclic Aromatic Hydrocarbon
pc	Parsec
PDF	Probability Density Function
PSF	Point Spread Function
SDSS	Sloan Digital Sky Survey
SED	Spectral Energy Distribution
SFH	Star-Formation History
SFR	Star-Formation Rate
SMBH	Super-massive Black Hole
SMF	Stellar Mass Function
SSP	Single Stellar Population
UDS	Ultra Deep Survey
UV	Ultraviolet
WFPC-2	Wide Field and Planetary Camera 2
ZFOURGE	FourStar Galaxy Evolution Survey

TABLE OF CONTENTS

Page

LIST OF FIGURES

FIGURE Page

LIST OF TABLES

TABLE Page

1. INTRODUCTION

1.1 How Do Galaxies Evolve?

The formation and evolution of galaxies involves a wide variety of physical processes governing dark matter, baryons, and interactions between the two. Several properties and processes that have been found to be relevant include radiative transfer, morphology, environment, metallicity, mass of the host dark matter halo and hydrodynamical interactions with supernovae and active galactic nuclei. Galaxy formation starts with the collapse of dark matter halos, centralized distributions of dark matter, out of the initial density perturbations in the early universe. As halos continue to merge and grow they accrete gas, converting it to stars forming the stellar component of a galaxy. As stars evolve they enter various phases where they enrich the surrounding inter-stellar medium (ISM) and circum-galactic medium (CGM) with metals (Nomoto et al. 2013). This has an influence on following star-formation as radiative cooling proceeds more efficiently in gas clouds of higher metallicity.

However, a variety of feedback processes are known to inhibit star formation, but these processes are poorly understood and can generally only be observed indirectly. For example, many galaxies (if not all) are known to host super-massive black holes (SMBH) at their centers that are typically 0.1% of the stellar mass of their host (Häring & Rix 2004). Occasionally clouds of baryonic matter become captured by the SMBH, forming an accretion disk and releasing large amounts of high-energy radiation. The radiation produced by these objects, referred to as active galactic nuclei (AGN; Urry & Padovani 1995), is capable of coupling with the gas within its host galaxy and preventing star-formation (Fabian 2012).

Even various phases of stellar evolution can disrupt star-forming regions and the

accretion of gas onto a galaxy. These include feedback from galaxy-scale winds produced by individual stars and stellar explosions known as supernovae. Ultimately, the conversion of gas into stars over cosmological timescales is a highly complex problem depending on many correlated properties and is thus not completely understood.

1.2 Measuring the Growth of Stellar Mass

Matter constitutes roughly 30% of the present-day energy density of the universe (e.g. Planck Collaboration 2015), broken up into components of dark matter ($\approx 26\%$) and baryonic matter ($\approx 4\%$). Given that dark matter is the dominant component it is the most important quantity that governs the evolution of a galaxy. However, by its nature dark matter itself has no observational signatures, thus we must rely on tracers from baryonic matter (e.g. stars, AGN, dust) in order to study star formation and galaxy evolution. Over the past two decades our understanding of the buildup of stellar matter in the universe has advanced markedly through a wealth of multiwavelength galaxy surveys (for a review see Madau & Dickinson 2014).

One of the most fundamental and general ways to track these effects is to measure the evolution of the galaxy stellar mass function (SMF) over cosmic time. The SMF is the cosmic number density of galaxies as a function of their stellar mass (see Figure 3 of Moustakas et al. (2013) for an example). Observations of the SMF show that less massive galaxies are more numerous than higher mass galaxies. It is recognized that a low-mass threshold must exist below which discrete galaxies cannot form, however, current observations are not yet sensitive enough to reveal this threshold. Nevertheless, because galaxies grow with time, the number density of galaxies at fixed stellar mass will increase with time.

It is well-known that the SMF does not follow the mass function of dark matter halos; this disagreement points to differences in the pathways that galaxies accu-

mulate stellar mass and dark matter. Thus, measurements of the SMF provide constraints on the feedback processes that regulate star formation. Much work has gone into measuring the SMF in recent years, and the development of deep near-IR surveys has allowed these studies to push to higher redshifts and to lower stellar masses (e.g. Perez et al. 2008, Drory et al. 2009, Marchesini et al. 2009, Ilbert et al. 2010, Brammer et al. 2011, Santini et al. 2012, Moustakas et al. 2013, Muzzin et al. 2013). Some of the more recent studies have revealed that the luminosity- and stellar mass-functions are not well-characterized by a standard Schechter function (Schechter 1976) due to a steepening of the slope at stellar masses below $10^{10} M_{\odot}$ (e.g. Baldry et al. 2004, Blanton et al. 2005). Beyond $z \sim 1$, however, no survey has been deep and wide enough to accurately constrain the low-mass end of the SMF.

Computer simulations of galaxy evolution can help unveil how galaxies evolve in real time providing a valuable complement to observational studies which are limited to instantaneous snapshots throughout cosmic history. However, galaxy evolution is inherently governed by physics on both small scales(e.g. radiative transfer) and large scales (e.g. gravitational tidal forces). The relevant scales of these physical process span a dynamic range of many orders of magnitude; therefore, detailed simulations can become computationally expensive quickly. Nevertheless, many simulations have been performed and are constantly being updated as advances in technology improve computational power.

A comparison of a simulated SMF from the Munich Galaxy Formation Model to the observed SMF can be seen in Figure 2 of Henriques et al. (2014). Each of the four panels show snapshots of the SMF at different epochs of the universe. Interestingly, the simulations are able to accurately reproduce the abundances of galaxies at both early and late times, but tend to over-predict abundances at intermediate times. This discrepancy is inevitably tied to the treatment of how star formation is regulated

for individual galaxies. This discrepancy could be taken to suggest that either the regulation of star formation in simulations is incorrect or that estimates of stellar mass from observations are systematically low (or possibly a combination of both). Weinmann et al. (2012), for example, argue that star formation in simulated galaxies is too closely tied to the host dark matter halo causing this offset.

1.3 Extracting Histories of Star Formation

It is important to bear in mind that the galaxy stellar mass function is a superposition of the stellar masses of the entire cosmic galaxy population. Thus, the SMF is implicitly tied to the star-formation histories (SFHs) of individual galaxies. However, inferring the star-formation and mass-growth histories of galaxies from observations is non-trivial, and a variety of methods have been used in the literature. One class of methods involves archeological studies of nearby galaxies, either by studying resolved stellar populations or by detailed modeling of high signal-to-noise spectra (e.g. Dolphin et al. 2003, Heavens et al. 2004, Thomas et al. 2005). However degeneracies in age, metallicity, and extinction complicate modeling with these techniques. Furthermore, these techniques become difficult or impossible to apply at appreciable redshifts.

This has provided the motivation for "lookback" studies of galaxy evolution: techniques which utilize observed relations of galaxies at discrete epochs in the universe to infer how individual galaxies evolve. One such type of study is to trace the mass-growth of galaxies selected in bins of constant cumulative co-moving number density (e.g. van Dokkum et al. 2010, Papovich et al. 2011, Patel et al. 2013). Given that the universe is expanding, distances between galaxies are increasing which has the effect of decreasing the number density of galaxies with time. However, co-moving distance is defined to account for this expansion thus counteracting its effect on the

number density evolution of galaxies. Number density selection (NDS) of galaxies at different epochs in the universe assumes that the ordering of a population of galaxies by stellar mass does not change as they evolve with time (e.g. the most massive galaxy today is the descendent of the most massive galaxy in the past). Figure 1 of van Dokkum et al. (2010) illustrates how this method can be used to infer mass-growth histories. The advantage of this technique is that it is based entirely on the observed distribution of galaxies at different epochs and thus makes no inherent assumptions about how star formation proceeds in galaxies. In reality, however, this rank-ordering of galaxies *will* change with time due to mergers and stochastic variations in star-formation rates (e.g. the most massive galaxy today could be the descendent of two intermediate-mass galaxies that merged in the past) Nevertheless, it is possible to approximately correct for these effects using an evolving number density criterion (Leja et al. 2013, Behroozi et al. 2013).

Another type of "lookback" study involves using the observed correlation between stellar mass and star-formation rate, referred to as the SFR$-M_*$ relation (e.g. Brinchmann et al. 2004, Noeske et al. 2007, Gilbank et al. 2011, Whitaker et al. 2012, Speagle et al. 2014). The physical interpretation of this relation is that galaxies with larger masses, and thus larger gravitational potentials, are able to accrete gas for fueling star-formation more quickly. This correlation has been shown to hold over a large dynamic range of stellar mass and star-formation rates and evolves in a self similar way with time. Therefore, by tracing along this evolving star-forming sequence it is possible to extract the time-evolution of the star-formation rate for a mock galaxy (i.e. the star-formation history or SFH). Integrating these star-formation histories over time represents predictions for the growth of stellar mass in galaxies (e.g. Leitner 2012, Speagle et al. 2014). In general some disagreement between this approach and the number density selection (NDS) is expected since the former does not include

growth due to mergers; indeed, Drory & Alverez (2008) use this difference to derive the merger rate.

1.4 Regulating Star Formation via Feedback

Although it is possible to empirically derive SFHs from observations, galaxy evolution is inevitably driven in part by stochastic processes that will not be the same for every galaxy. Such processes include galaxy-galaxy mergers/interactions, variations in mass accretion rates, and feedback processes driven by stellar evolution and/or active galactic nuclei (AGN). Furthermore, recent models argue that these processes can act mechanisms to either trigger or truncate star-formation in a galaxy (Silk 2013, Merloni & Heinz 2008).

One fundamental observation is that dense environments at low redshifts are dominated by passive, early-type galaxies that define a narrow red sequence in an optical color-magnitude diagram (Sandage & Visvanathan 1978, Bower et al. 1992, Hogg et al. 2004), and studies of the cluster color-magnitude relation (CMR) show that the luminous red sequence members in galaxy clusters have not evolved significantly since $z \sim 0.8$ (Rudnick et al. 2009). In contrast, the less massive cluster members continue to migrate to the red sequence as studies at $z > 0.6$ show there are fewer faint red galaxies in clusters compared the field and to lower redshift clusters (De Lucia et al. 2007, Stott et al. 2007, Rudnick et al. 2009). Recent observations at $z > 1.4$ have now even found massive, star-forming galaxies in clusters (Tran et al. 2010, Hilton et al. 2010).

The question then remains as to what halts star formation in cluster galaxies? Possible environmental processes include ram-pressure stripping (Gunn & Gott 1972), tidal effects from the cluster potential (Farouki & Shapiro 1981), and galaxy-galaxy interactions (Richstone 1976), but none are completely effective at repro-

ducing the star formation histories and scaling relations observed in galaxy clusters. Semi-analytic models that include AGN are able to reproduce observed mass/luminosity functions (Croton et al. 2006, Bower et al. 2006, Lagos et al. 2008). AGN can also affect the intra-cluster medium (ICM) where models find that including AGN produces much better agreement with observations of X-ray properties of the ICM (Bower et al. 2008, Puchwein et al. 2008, McCarthy et al. 2010).

AGN feedback seems to be an ideal solution to resolve many outstanding discrepancies between models and observations (Gabor et al. 2010, Fontanot et al. 2010, Teyssier et al. 2011); however, there is not yet clear observational evidence that AGN contribute significantly to the quenching of star formation in cluster galaxies, making clusters into resting homes of passive galaxies. Several groups using primarily X-ray observations find the fractional density of X-ray selected active galactic nuclei (X-ray AGN) in cluster environments increases with redshift (Eastman et al. 2007, Martini et al. 2009). Similarly, using X-ray, infrared and radio selection at $z < 1.5$ Galametz et al. (2009) find that the AGN surface-density (N/arcmin^2) is greater for clusters than in the field and that the AGN volume-density (N/Mpc^3) for clusters increases with redshift. In contrast, a study of CL $0023+04$, a large scale system of four galaxy groups merging at $z \sim 0.83$, does not find an excess of X-ray sources relative to the field (Kocevski et al. 2009). In general, studies are hampered by the small number of X-ray AGN and the need to isolate a large sample of cluster galaxies at higher redshifts. Another important issue is that different diagnostics select different populations of AGN (Hart et al. 2009, Hickox et al. 2009, Griffith & Stern 2010) and so no single approach will be complete. Thus while CL $0023+04$ does not have an excess of X-ray sources, Lubin et al. (2009) do find a population of passive (no detectable Hα) members with [OII] emission that may be due to AGN.

In the first chapter of this dissertation we make use of two modern galaxy surveys

with complementary advantages in order to produce the most up-to-date measurement of the evolution of the galaxy stellar mass function over the past 11.5 billion years of the universe. The depth of these surveys will allow us to place constraints on the buildup of low-mass galaxies previously below the detection limits of preceding surveys. In the following chapter we utilize the evolution of the SMF in concert with the evolution of the SFR$-M_*$ relation of galaxies in order to extract star-formation and mass-growth histories of galaxies. In order to maintain internal consistency with the measurement of the SMF, we utilize the same galaxy surveys with ancillary data for estimating star-formation rates. Finally, we end this dissertation with a study of the prevalence of active galactic nuclei in the universe and their potential link to the quenching of star-formation in galaxies. For this analysis we make use of infrared data which have the advantage of being able to identify AGN that are obscured by large amounts of interstellar dust, and could subsequently be missed by other methods such as X-ray studies.

Throughout this dissertation we use a Chabrier (2003) initial mass function (IMF) and ΛCDM cosmological parameters of $\Omega_M = 0.3$, $\Omega_\Lambda = 0.7$ and $h = 0.7$. All magnitudes are in the absolute bolometric system (AB).

2. NEW INSIGHTS ON THE GALAXY STELLAR MASS FUNCTION: AN EXCESS OF LOW-MASS GALAXIES SINCE $z = 2$ AND THE RAPID BUILDUP OF QUIESCENT GALAXIES*

2.1 Background Information

Galaxy formation and evolution depend on the physics governing dark matter, baryons, and interactions between the two. The process starts with the collapse of dark matter halos out of the initial density perturbations in the early universe. As halos continue to merge and grow they accrete gas, converting it to stars forming the stellar mass of a galaxy. A variety of feedback processes are known to inhibit star formation, but these processes are poorly understood and can generally only be observed indirectly.

These effects in combination dictate the growth of a galaxy's stellar mass. One of the most fundamental ways to trace these effects is to measure the evolution of the galaxy stellar mass function (SMF) over cosmic time. It is well-known that the SMF does not follow the mass function of dark matter halos; this disagreement points to differences in the pathways that galaxies accumulate stellar mass and dark matter. Thus, measurements of the SMF provide constraints on the feedback processes that regulate star formation. Much work has gone into measuring the SMF in recent years, and the development of deep near-IR surveys has allowed these studies to push to higher redshifts and to lower stellar masses (e.g. Perez et al. 2008, Drory et al. 2009, Marchesini et al. 2009, Ilbert et al. 2010, Brammer et al. 2011, Santini et al. 2012, Moustakas et al. 2013, Muzzin et al. 2013).

* Reprinted with permission from "Galaxy Stellar Mass Functions from ZFOURGE/CANDELS: An Excess of Low-mass Galaxies since z = 2 and the Rapid Buildup of Quiescent Galaxies" by Tomczak et al., 2014. The AstroPhysical Journal, 783, 85-99, Copyright 2014 by Adam Tomczak.

In this chapter we extend measurements of the SMF to masses > 1 dex deeper than results from recent large surveys at $0.2 < z < 3$. Studies over the past decade have revealed that the luminosity function and the SMF are not well-characterized by a standard Schechter function (Schechter 197676) due to a steepening of the slope at stellar masses below $10^{10} M_{\odot}$ (e.g. Baldry et al. 2004, Blanton et al. 2005). Beyond $z \sim 1$ no survey has been deep and wide enough to accurately constrain the low-mass end of the SMF. Here we use new data from the FourStar Galaxy Evolution Survey (ZFOURGE) to construct the deepest measurement of the SMF to date. We find a visible upturn in the total SMF at $< 10^{10} M_{\odot}$ as early as $z = 2$. Furthermore, we measure the SMF of star-forming and quiescent galaxies separately, finding that these populations evolve differently with cosmic time. The star-forming SMF grows slowly, while the quiescent SMF grows much more rapidly, especially at low masses; we find that the quiescent fraction of $9 < \log(M_*/M_{\odot}) < 10$ galaxies increases by $\sim 5\times$ from $z \approx 2$ to $z \approx 0.1$ indicating that a large number of low-mass star-forming galaxies are becoming quenched. In this work we take into account uncertainties due to photometric redshifts, stellar mass estimates, the classification of galaxies at star-forming versus quiescent and cosmic variance.

2.2 Data and Methods

2.2.1 Photometry

We make use of the deep near-IR imaging from the FourStar Galaxy Evolution survey (ZFOURGE; Straatman et al. in prep) conducted using the FourStar imager Persson et al. (2013) on the 6.5m Magellan Baade telescope at Las Campanas Observatory. The use of medium-band filters in the near-IR (van Dokkum et al. 2009) allows us to accurately sample wavelengths bracketing the Balmer break of galaxies leading to more well-constrained photometric redshifts at $1 < z < 4$ than with

broadband filters alone. In conjunction with existing optical through mid-IR photometry, this dataset provides a comprehensive sampling of the 0.3 – 8μm spectral energy distribution (SED) of galaxies.

The ZFOURGE data and photometry are described in detail by Straatman et al. (in prep.). Here we provide a brief summary. ZFOURGE is composed of three $11' \times 11'$ pointings with coverage in the CDFS (Giacconi et al. 2002), COSMOS (Capak et al. 2007a) and UDS (Lawrence et al. 2007). The 5σ depth in a circular aperture of 0.6" diameter in K_s is 24.8, 25.2 and 24.6 in the CDFS, COSMOS and UDS fields respectively. Typical seeing was 0.8" or better in the ground based bands. All optical-NIR images were convolved to a moffat PSF with FWHM=0.75"; for some images this meant deconvolution from an originally larger PSF. Fluxes were then measured within a circular aperture of 0.8". Since image quality is much lower in the *Spitzer* IRAC bands this photometry was first deblended using the H_{160} image with the techniques of Labbé et al. (2006). Apart from the *Spitzer* IRAC imaging, blending and source confusion is a minor issue.

The ZFOURGE fields also benefit from HST imaging taken as part of the CANDELS survey (Grogin et al. 2011, Koekemoer et al. 2011). We utilize the J_{125} and H_{160} imaging which reach $\sim$26.5 mag, significantly deeper than our ground-based medium-band data. The high S/N photometry aids in photometric redshift estimates even though the filters are broader than our ground-based medium-band data. We also use the H_{160} data as our detection image. But because some of the faintest sources in the H_{160} images are not detected in our ground-based data – and thus will have poorly constrained SEDs – we limit our study to objects detected at $\mathrm{SNR}_{160} > 10$ (corresponding to $H_{160} \sim 25.9$) as a threshold to remove galaxies that are poorly detected at other wavelengths. The total area of our final sample with full coverage in ZFOURGE and CANDELS is $\sim$316 arcmin^2.

We also make use of data from the NEWFIRM Medium-Band Survey (NMBS; Whitaker et al. 2011) which includes imaging in the same set of medium-band near-IR filters as ZFOURGE. The similarity of the photometry helps reduce any inter-survey systematics. NMBS is composed of two $30' \times 30'$ pointings in the AEGIS (Davis et al. 2007) and COSMOS (Capak et al. 2007a) fields. The COSMOS pointing encompasses one of the ZFOURGE fields; in the region of overlap we make use of the higher-quality ZFOURGE data as opposed to the NMBS data. Photometric redshifts from NMBS are shown to have a scatter of $\sigma_z/(1+z) = 0.017$, 0.008 in the AEGIS and COSMOS fields respectively when compared to spectroscopic redshifts (Whitaker et al. 2011). Although NMBS is shallower than the rest of our sample, reaching depths of ∼24.5 mag in J_1, J_2, J_3 and ∼23.5 mag in H_s, H_l, K_s, including it increases our survey area by a factor of 5.3 allowing us to much better constrain the high-mass end of the SMF (see Brammer et al. 2011).

2.2.2 Photometric Redshifts & Stellar Masses

We use the public SED-fitting code `EAZY` (Brammer et al. 2008) to measure photometric redshifts and rest-frame colors. `EAZY` utilizes a default set of 6 spectral templates that include prescriptions for emission lines derived from the `PEGASE` models (Fioc & Rocca-Volmerange 1997) plus an additional dust-reddened template derived from the Maraston (2005) models. Linear combinations of these templates are fit to the 0.3 – 8μm photometry for each galaxy to estimate redshifts.

Figure 2.1 demonstrates the accuracy of our photometric redshifts in comparison to available spectroscopic redshifts. Only sources reported with secure spectroscopic detections are considered. Overall, we find a normalized median absolute deviation (NMAD) scatter of 1.8% in $\Delta z/(1+z_{spec})$. At $z < 1.5$ this scatter becomes 1.7% with about 2.7% of catastrophic failures ($|\Delta z/(1+z_{spec})| > 0.15$). As we push to

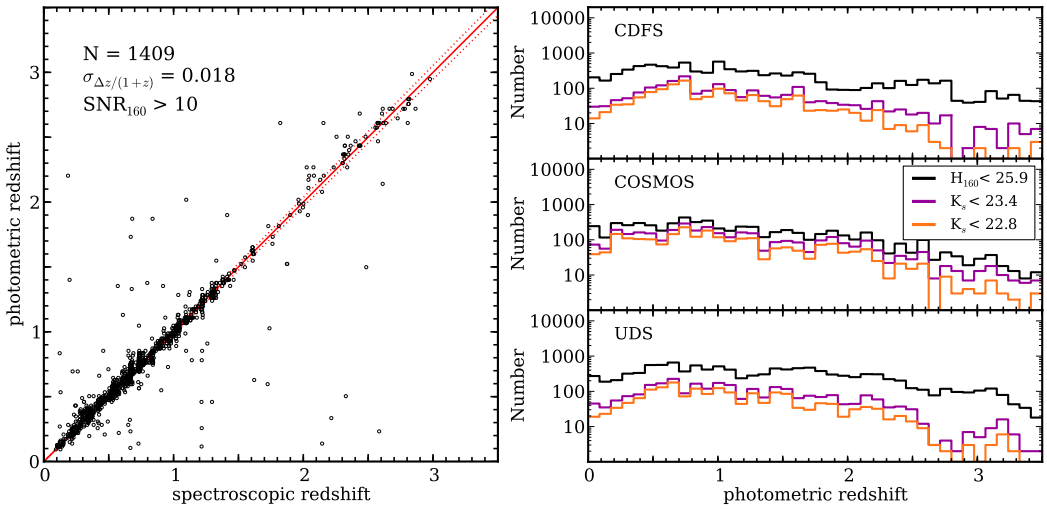

Figure 2.1: Spectroscopic vs. Photometric Redshifts.
Left: Comparison of spectroscopic to photometric redshifts across all three pointings of ZFOURGE. Only secure spectroscopic redshifts of objects at $\mathrm{SNR}_{160} > 10$ are considered. We find a NMAD scatter of 0.018 in $\Delta z/(1+z)$ shown by the red dotted lines with about 3% of sources being catastrophic outliers ($|\Delta z/(1+z_{spec})| > 0.15$). **Right:** Redshift distributions in each ZFOURGE field corresponding to our estimated magnitude limit (black) as well as the magnitude limits of UltraVISTA (purple; McCracken et al. 2012) and NMBS (orange; Brammer et al. 2011).

$z > 1.5$, where the Balmer break of galaxies redshifts into the medium-band NIR filters, this scatter becomes 2.2% with about 9% of catastrophic failures. We note here that this scatter is likely biased upward since objects with secure spectroscopic redshifts tend to be strongly star-forming systems with weak Balmer breaks, and thus do not benefit the most from the deep medium-band NIR photometry from ZFOURGE. Also shown in Figure 2.1 are redshift distributions in the three fields of ZFOURGE corresponding to our estimated magnitude limit as well as the magnitude limits of UltraVISTA (McCracken et al. 2012) and NMBS (Brammer et al. 2011) in black, purple and orange respectively. Spectroscopic redshifts from CDFS come from Vanzella et al. (2008), Le Fèvre et al. (2005), Szokoly et al. (2004), Doherty et al. (2005), Popesso et al. (2009), and Balestra et al. (2010). Spectroscopic redshifts from UDS come from Simpson et al. (2012) and Smail et al. (2008). Spectroscopic redshifts from COSMOS come from the NASA/IPAC Infrared Science Archive[‡‡].

However a comparison to spectroscopic samples can be of limited use, since the result of such comparisons depend strongly on how the spectroscopic objects were selected. Moreover, fainter objects and more distant objects, which are more difficult to detect spectroscopically, are also expected to have larger photometric redshift errors. We use the close-pairs analysis of Quadri & Williams (2010) to estimate the typical uncertainties for the full sample of objects in our catalog, finding $\sigma \approx 0.02$ at $z \sim 0.5$ and this increases to $\sigma \approx 0.05$ at $z \sim 2.5$.

To obtain stellar masses we use the `FAST` code (Kriek et al. 2009) which fits stellar population synthesis models to the measured SEDs of galaxies to infer various galactic properties. Specifically, we use models from Bruzual & Charlot (2003) following an exponentially declining star-formation history assuming a Chabrier (2003) initial mass function. We assume solar metallicity and allow A_V to vary between $[0, 4]$.

‡‡ http://irsa.ipac.caltech.edu/data/COSMOS/

We note here that stellar masses derived from SED-fitting are dependent on assumed parameters in the models (metallicity, dust law, stellar population models etc.). Variations in these assumptions have been shown to lead to systematic offsets in stellar masses as opposed to random errors (e.g Maraston 2005, Marchesini et al. 2009, Conroy et al. 2009), however a full investigation of these effects is beyond the scope of this dissertation.

2.2.3 Stellar Mass Completeness

Understanding the mass-completeness limits of our dataset is crucial to our analysis. Marchesini et al. (2009) describe a technique whereby a sample of galaxies below the nominal flux-completeness limit is taken from a deeper survey. These galaxies were then scaled up in flux and mass to the completeness limit of their survey. The resulting distribution in mass forms a representative sample of the most massive galaxies that could just escape detection in their sample. The upper envelope of this distribution will therefore represent an empirical determination of the redshift-dependent mass-completeness limit.

In the absence of deeper data, Quadri et al. (2012) modified this technique slightly by using a sample that lies above the flux completeness limit and scaling the fluxes and the masses down; this is the method adopted here. We start with all galaxies that are a factor 2 - 3$\times$ above our signal-to-noise threshold ($\mathrm{SNR}_{160} > 10$) and scale down their masses by the appropriate factor. From this scaled down sample we take the upper envelope that encompasses 80% of the galaxies as the redshift-dependent mass-completeness limit, shown in blue in Figure 2.2.

To obtain another measurement of the mass-completeness limit, we employ a similar technique to that described by Chang et al. (2013). First we estimate the magnitude limit corresponding to our SNR threshold to be $H_{160} \approx 25.9$. Then, in

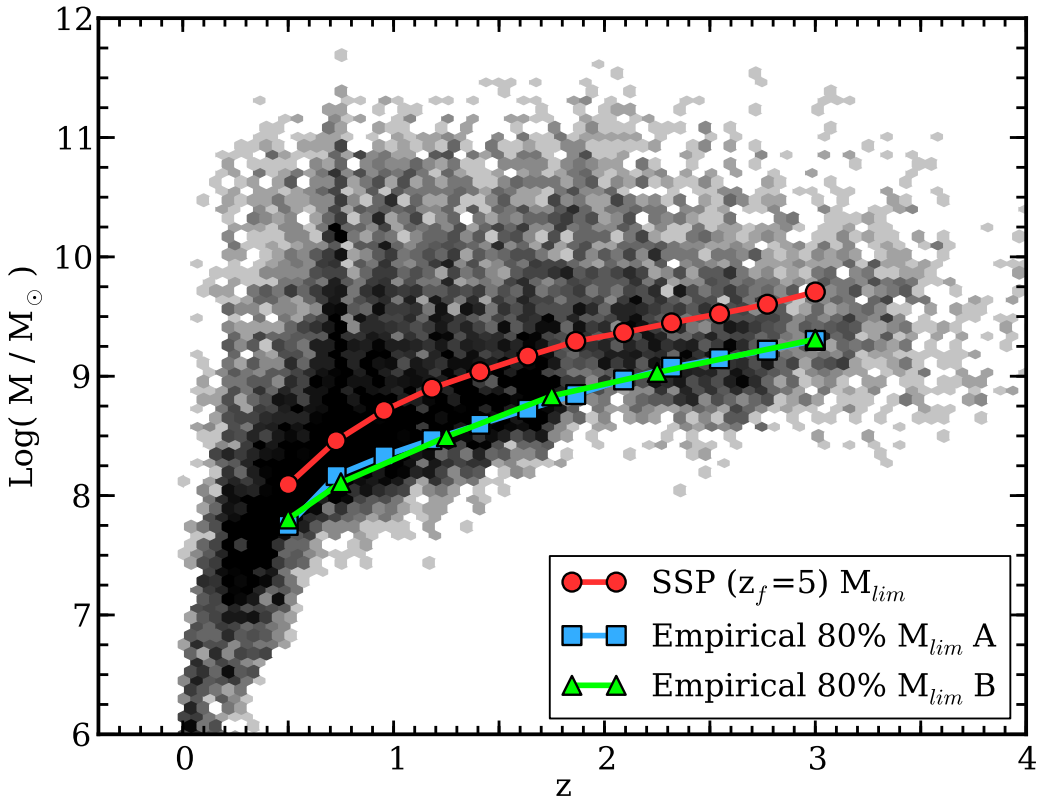

Figure 2.2: Mass Completeness.
Galaxy stellar mass as a function of redshift for our H_{160}-selected sample. The grayscale corresponds to the density of galaxies in cells of redshift and stellar mass. Galaxies at high redshift are more distant thus making it more challenging to detect lower-mass galaxies which are intrinisically faint. Because of this, we are unable to detect galaxies in the bottom-right portion of this diagram. The colored curves correspond to our estimated completeness limits, above which we trust we are detecting all galaxies present in the survey volume. Empirically derived 80% mass-completeness limits from down-scaling galaxies to our SNR limit and from magnitude-mass diagrams are shown in blue and green respectively (see section 2.2.3). Both techniques yield nearly identical limits. Because quiescent galaxies have higher mass-to-light ratios their mass-completeness limit is higher than for average galaxies. The red curve shows the completeness limit determined from passively evolving a SSP with a formation redshift $z_f = 5$ which we adopt as a separate mass-completeness limit for the quiescent population.

narrow bins of mass we calculate the fraction of galaxies that are brighter than this magnitude at all SNRs. At the highest stellar masses this is 100% but gradually decreases as we probe towards lower masses. We search for the mass-bin where this fraction is 80% at various redshifts, which we take as the mass-completeness limit. The results from this technique are shown in green in Figure 2.2.

Both of the empirical techniques above are performed on all galaxies (i.e. without distinguishing star-forming/quiescent) and yield nearly identical values which gives us confidence in our measurements. We use these mass-completeness limits for both the total and star-forming SMFs.

Finally, since quiescent galaxies have higher mass-to-light ratios than the general population, the corresponding mass-completeness limit will be higher. We calculate this mass-completeness limit from a stellar population synthesis model obtained from EzGal (Mancone & Gonzalez 2012). Specifically, we consider a single stellar population (SSP) following a Chabrier (2003) IMF, of solar metallicity formed at a redshift of $z_f = 5$. The mass-completeness limit derived from this approach is representative of the oldest galaxies at a given redshift since z_f. We adopt this as the mass-completeness limit for quiescent galaxies, shown in red in Figure 2.2.

Our data provide a view of the SMF to depths that have previously been inaccessible over significant areas. In Figure 2.3 we plot an example SMF as measured by ZFOURGE, UltraVISTA (Muzzin et al. 2013) and NMBS (Brammer et al. 2011) which reach K_s-band 5σ depths of about 24.9, 23.4 and 22.8 magnitudes respectively. Furthermore, since ZFOURGE is split into three independent pointings, errors due to cosmic variance are suppressed compared to a survey of equal area composed of one pointing. We show an example of field-to-field variance in Figure 2.4 where we plot the SMF measured from each ZFOURGE pointing individually.

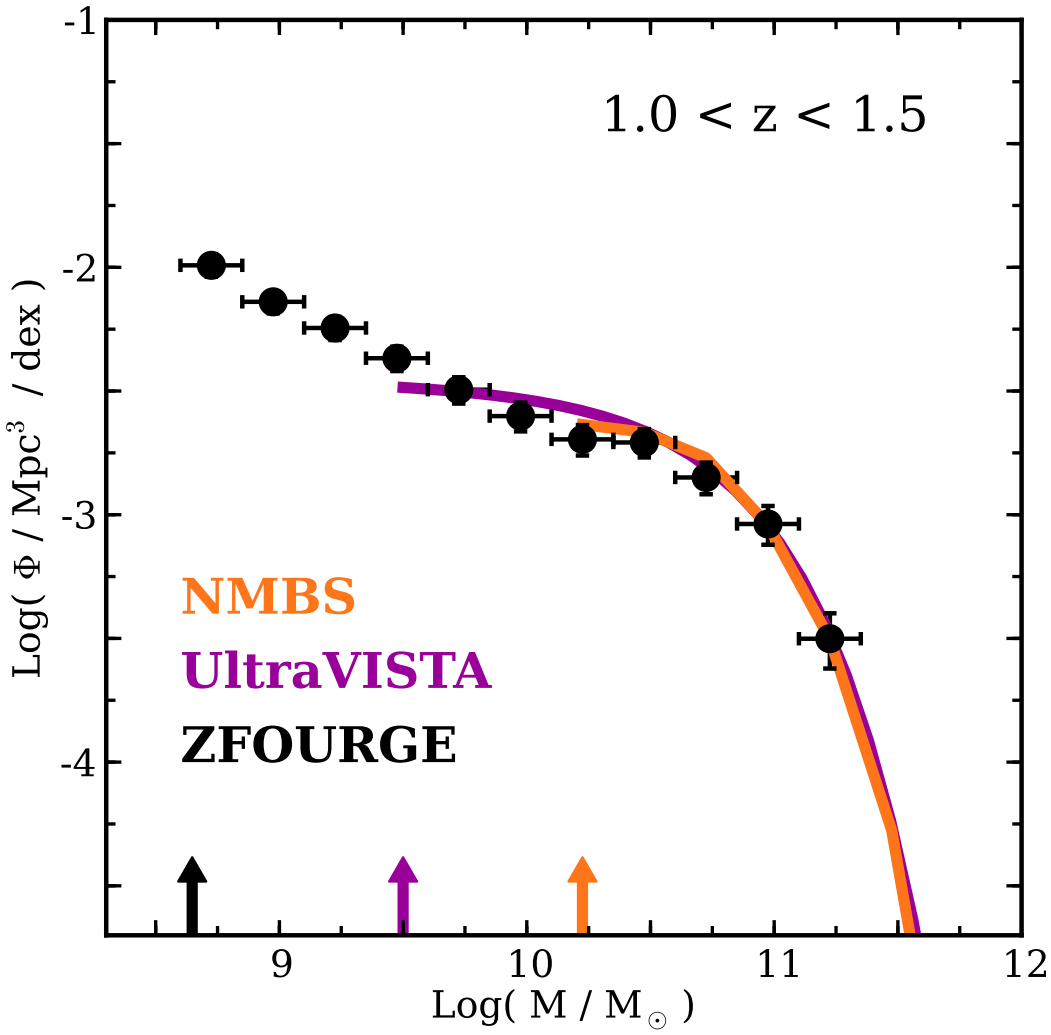

Figure 2.3: Stellar Mass Function Depths.
The stellar mass function at $z = [1.0, 1.5]$ as measured by recent deep surveys compared to ZFOURGE: NMBS (orange; Brammer et al. 2011) and UltraVISTA (purple; Muzzinb). The SMF represents the cosmic number density of galaxies in small bins of stellar mass, 0.25 dex in width for this example. Number densities are normalized by this value so that Φ is independent of the chosen bin width. Arrows indicate the respective mass-completeness limits. Errorbars shown here represent total 1σ errors as described in section 2.2.5. Previous studies were not able to reach a great enough depth over a significant area to reveal the steepening of the SMF.

2.2.4 Selection of Star-Forming & Quiescent Galaxies

In this work we divide the full galaxy sample into star-forming and quiescent populations. We separate these populations in a rest-frame $U - V$ vs. $V - J$ color-color diagram (hereafter UVJ diagram), which has been shown to effectively trace the galaxy color-bimodality as far as $z = 3$ (Labbé et al. 2005, Williams et al. 2009, Patel et al. 2012, Whitaker et al. 2011, Muzzin et al. 2013). The strength of this technique lies in its weak dependence on dust extinction, since the dust-reddening vector tends not to scatter galaxies across the selection boundary. This helps avoid contamination by dusty star-forming galaxies in typical red-sequence selection techniques.

We derive rest-frame $U - V$ and $V - J$ colors from the best-fit `EAZY` templates to the observed photometry. In Figure 2.5 we show UVJ diagrams for our galaxy sample at various redshifts. Only galaxies above their respective mass-completeness limit are shown. The bimodality can be seen to $z \sim 3$.

2.2.5 Uncertainties

The accuracy with which we are able to measure the SMF is dependent on multiple steps, each having its own uncertainty. Poisson uncertainties ($\sigma_{poisson}$) are calculated using prescriptions from Gehrels (1986). We also include cosmic variance (σ_{cv}) and uncertainties in the SED modeling used to estimate photometric redshifts, rest-frame colors and stellar masses (σ_{sed}).

We calculate cosmic variance as a function of redshift and mass using the `getcv` routine described in Moster et al. (2011). This yields cosmic variance uncertainties that range from ≈25% at $10^{11} M_{\odot}$ to ≈8% at $10^{8.5} M_{\odot}$. Cosmic variance can also be estimated from the scatter in the SMFs of the independent pointings from ZFOURGE (Figure 2.4). Overall, we find this scatter to be consistent with the predictions.

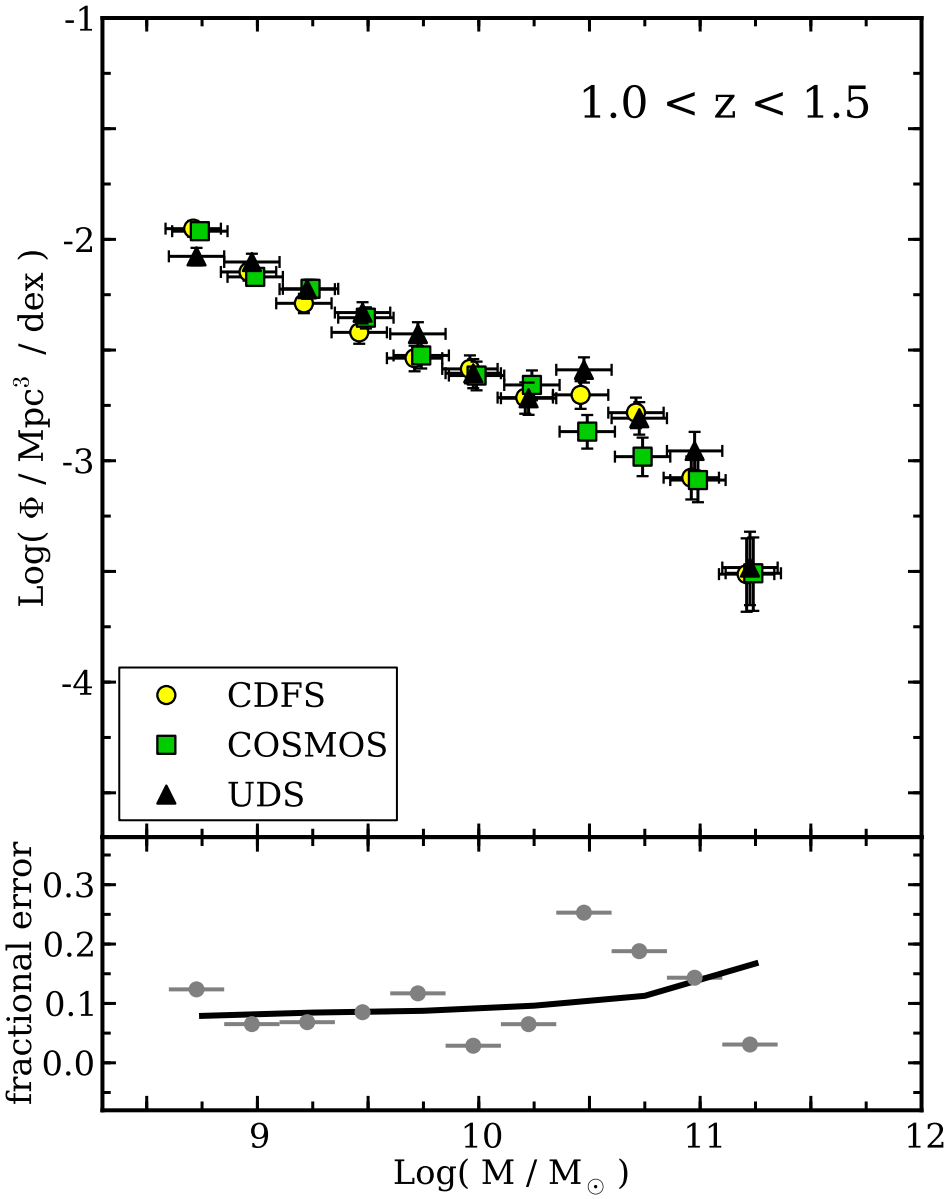

Figure 2.4: Cosmic Variance within ZFOURGE.
The stellar mass function at $z = [1.0, 1.5]$ measured independently in all three ZFOURGE subfields (excluding data from NMBS). Our total combined survey area is $\sim$316 arcmin^2. Errorbars shown here represent Poisson and SED-fitting uncertainties but exclude cosmic variance estimates. In the bottom panel we show the fractional uncertainty introduced by cosmic variance determined from the standard deviation in the SMF among the three fields (gray points). The black line shows the predicted uncertainty using prescriptions from Moster et al. (2011) which is in agreement with the scatter we see among our independent SMFs.

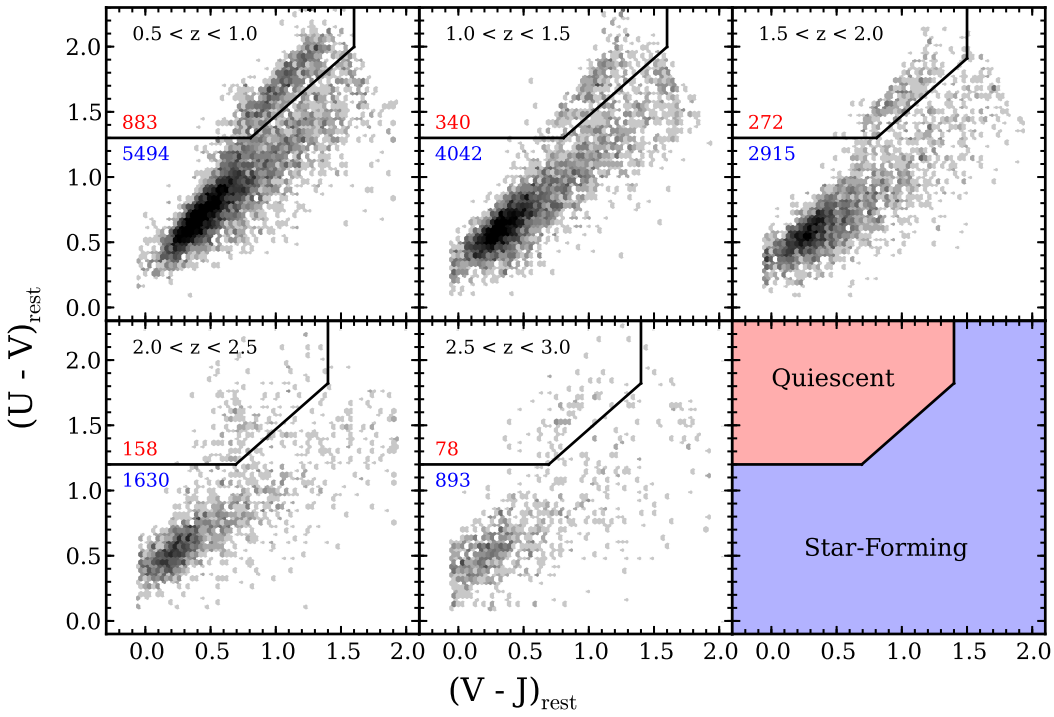

Figure 2.5: Selection of Star-forming vs. Quiescent Galaxies.
Rest-frame UVJ diagrams used to separate star-forming and quiescent galaxies as indicated in the bottom-right panel. Only galaxies above our mass-completeness limits are shown from all three ZFOURGE pointings (CDFS, COSMOS, UDS; the NMBS data are excluded). In each panel, the number of quiescent and star-forming galaxies are shown in the selection regions in red and blue respectively. Due to the similarity between our dataset and NMBS, we use the redshift-dependent selection regions (shown in black) determined in Whitaker et al. (2011).

To estimate the uncertainty contribution from SED modeling we conduct 100 Monte Carlo simulations on our catalogs. For each realization we independently perturb photometric redshifts and stellar masses using the 68% confidence limits output from `EAZY` and `FAST`. SMFs are then recalculated over the same redshift ranges used throughout. The 1σ scatter in the resulting SMFs is then taken as the redshift- and mass-dependent uncertainty. These uncertainties range from 5 - 15% over the span of redshifts in this study.

We consider another source of uncertainty involved in the classification of galaxies as star-forming vs. quiescent. Here, we evaluate the statistical uncertainty associated with the UVJ classification based on photometric uncertainties (σ_{uvj}). To do this we perform 100 Monte Carlo simulations on a sample of galaxies at $10 < \mathrm{SNR}_{160} < 200$, perturbing fluxes according to a Gaussian probability density function based on 1σ photometric uncertainties. Photometric redshifts and rest-frame colors were remeasured for each iteration, from which galaxies were reclassified as being star-forming or quiescent. We find that at fixed SNR_{160} more galaxies scatter into vs. out of the quiescent region, boosting the quiescent fraction. However this effect is small; we find that the quiescent fractions typically vary by $< 2\%$, and that this value has a scatter of $< 0.4\%$ between the simulations. A particular concern may be that the number density of quiescent sources at low masses may be significantly affected by a small fraction of the (much more abundant) star-forming galaxies scattering into the quiescent region, but we find that this is not a major concern. In total, our uncertainty budgets become:

$$\begin{aligned} \sigma_{\mathrm{tot}} &= \sqrt{\sigma^2_{poisson} + \sigma^2_{cv} + \sigma^2_{sed}} \\ \sigma_{\mathrm{sf/qui}} &= \sqrt{\sigma^2_{poisson} + \sigma^2_{cv} + \sigma^2_{sed} + \sigma^2_{uvj}} \end{aligned} \tag{2.1}$$

2.3 Results

2.3.1 Measuring the Stellar Mass Function

In Figure 2.6 we show our measurements of the total SMF over $0.2 < z < 3$. For comparison we have included corresponding measurements at similar redshifts intervals from recent works (Santini et al. 2012, Moustakas et al. 2013, Ilbert et al. 2013, Muzzin et al. 2013). We find excellent agreement in the regions of overlap,

Table 2.1: Stellar Mass Functions: Total.

	$0.2 < z < 0.5$	$0.5 < z < 0.75$	$0.75 < z < 1.0$	$1.0 < z < 1.25$	$1.25 < z < 1.5$	$1.5 < z < 2.0$	$2.0 < z < 2.5$	$2.5 < z < 3.0$
$\mathrm{Log}(\mathrm{M}/M_\odot)$	$\mathrm{Log}(\Phi)$	$\mathrm{Log}(\Phi)$	$\mathrm{Log}(\Phi)$	$\mathrm{Log}(\Phi)$	$\mathrm{Log}(\Phi)$	$\mathrm{Log}(\Phi)$	$\mathrm{Log}(\Phi)$	$\mathrm{Log}(\Phi)$
8.00	$-1.37^{+0.06}_{-0.07}$	—	—	—	—	—	—	—
8.25	$-1.53^{+0.06}_{-0.07}$	$-1.53^{+0.06}_{-0.07}$	—	—	—	—	—	—
8.50	$-1.71^{+0.07}_{-0.08}$	$-1.60^{+0.05}_{-0.06}$	$-1.70^{+0.05}_{-0.06}$	—	—	—	—	—
8.75	$-1.86^{+0.07}_{-0.08}$	$-1.76^{+0.06}_{-0.06}$	$-1.86^{+0.05}_{-0.06}$	$-1.99^{+0.06}_{-0.06}$	$-2.02^{+0.06}_{-0.07}$	—	—	—
9.00	$-2.03^{+0.08}_{-0.09}$	$-1.86^{+0.06}_{-0.07}$	$-2.01^{+0.06}_{-0.06}$	$-2.14^{+0.06}_{-0.07}$	$-2.14^{+0.06}_{-0.07}$	$-2.20^{+0.05}_{-0.06}$	—	—
9.25	$-2.01^{+0.07}_{-0.08}$	$-2.00^{+0.06}_{-0.07}$	$-2.10^{+0.06}_{-0.07}$	$-2.24^{+0.06}_{-0.07}$	$-2.28^{+0.06}_{-0.07}$	$-2.31^{+0.05}_{-0.06}$	$-2.53^{+0.06}_{-0.07}$	—
9.50	$-2.10^{+0.07}_{-0.09}$	$-2.12^{+0.07}_{-0.08}$	$-2.23^{+0.06}_{-0.07}$	$-2.29^{+0.06}_{-0.07}$	$-2.46^{+0.07}_{-0.08}$	$-2.41^{+0.05}_{-0.06}$	$-2.50^{+0.06}_{-0.07}$	$-2.65^{+0.06}_{-0.07}$
9.75	$-2.17^{+0.08}_{-0.10}$	$-2.21^{+0.06}_{-0.07}$	$-2.39^{+0.07}_{-0.08}$	$-2.48^{+0.07}_{-0.08}$	$-2.53^{+0.07}_{-0.08}$	$-2.54^{+0.06}_{-0.06}$	$-2.63^{+0.06}_{-0.07}$	$-2.78^{+0.07}_{-0.08}$
10.00	$-2.24^{+0.08}_{-0.10}$	$-2.25^{+0.06}_{-0.08}$	$-2.45^{+0.07}_{-0.09}$	$-2.59^{+0.08}_{-0.09}$	$-2.61^{+0.08}_{-0.09}$	$-2.67^{+0.06}_{-0.07}$	$-2.74^{+0.07}_{-0.08}$	$-3.02^{+0.08}_{-0.09}$
10.25	$-2.31^{+0.08}_{-0.09}$	$-2.35^{+0.07}_{-0.08}$	$-2.45^{+0.07}_{-0.09}$	$-2.73^{+0.08}_{-0.10}$	$-2.68^{+0.08}_{-0.09}$	$-2.76^{+0.06}_{-0.07}$	$-2.91^{+0.08}_{-0.09}$	$-3.21^{+0.09}_{-0.10}$
10.50	$-2.41^{+0.08}_{-0.10}$	$-2.45^{+0.07}_{-0.09}$	$-2.52^{+0.08}_{-0.09}$	$-2.64^{+0.07}_{-0.09}$	$-2.71^{+0.08}_{-0.09}$	$-2.87^{+0.07}_{-0.08}$	$-3.07^{+0.09}_{-0.10}$	$-3.35^{+0.10}_{-0.13}$
10.75	$-2.53^{+0.09}_{-0.11}$	$-2.55^{+0.08}_{-0.09}$	$-2.59^{+0.08}_{-0.10}$	$-2.72^{+0.08}_{-0.10}$	$-2.84^{+0.08}_{-0.10}$	$-3.03^{+0.08}_{-0.09}$	$-3.35^{+0.10}_{-0.13}$	$-3.74^{+0.13}_{-0.17}$
11.00	$-2.91^{+0.11}_{-0.15}$	$-2.82^{+0.09}_{-0.11}$	$-2.93^{+0.10}_{-0.13}$	$-3.01^{+0.10}_{-0.12}$	$-3.12^{+0.10}_{-0.13}$	$-3.13^{+0.08}_{-0.10}$	$-3.54^{+0.12}_{-0.16}$	$-4.00^{+0.18}_{-0.25}$
11.25	$-3.46^{+0.14}_{-0.18}$	$-3.32^{+0.10}_{-0.13}$	$-3.47^{+0.11}_{-0.15}$	$-3.62^{+0.11}_{-0.15}$	$-3.65^{+0.12}_{-0.16}$	$-3.56^{+0.10}_{-0.13}$	$-3.89^{+0.12}_{-0.17}$	$-4.14^{+0.17}_{-0.28}$
11.50	—	—	—	—	$-4.99^{+0.30}_{-0.41}$	$-4.27^{+0.12}_{-0.15}$	$-4.41^{+0.14}_{-0.19}$	$-4.73^{+0.31}_{-2.00}$

except with Santini et al. (2012) who measure higher densities of galaxies at $z > 2$.

In Figure 2.7 we subdivide the total SMF into star-forming and quiescent populations over the same range of redshifts as in Figure 2.6. The data are also presented in Tables 2.1 and 2.2. We reiterate that these mass functions have been supplemented by NMBS to provide better constraints at the high-mass end. Orange arrows show the mass-limits for the contribution of NMBS to each SMF in Figure 2.7. We also show the growth of each SMF (total, star-forming, and quiescent) in Figure 2.8 over our entire redshift range.

In calculating the SMF, we include only galaxies that lie above the mass-completeness limit corresponding to the upper redshift limit of each subsample. We follow the procedures outlined in Avni & Bahcall (1980) to combine the multiple fields of our survey in calculating SMFs. The SMF (Φ) is then simply calculated as:

$$\Phi(M) = \frac{1}{\Delta M} \sum_{i=1}^{N} \frac{1}{V_c} \tag{2.2}$$

where $M = \log(M_*/M_\odot)$, ΔM is the size of the mass-bin, N is the number of galaxies in the mass-bin between the redshift limits ($z_{\rm min}$, $z_{\rm max}$) and V_c is the comoving volume based on the survey area and redshift limits. We refrain from using the $1/V_{\rm max}$ formalism (Avni & Bahcall 1980) to avoid introducing any potential bias associated with evolution in the SMF over our relatively wide redshift bins. Since we do not apply a $1/V_{\rm max}$ correction, V_c is the same for all galaxies in a given redshift bin.

2.3.2 Fitting the Stellar Mass Function

The depth of our survey allows us to test for the shape of the SMF, namely we fit both single- and double-Schechter functions to determine the best fit. The single-Schechter (1976) function is defined as:

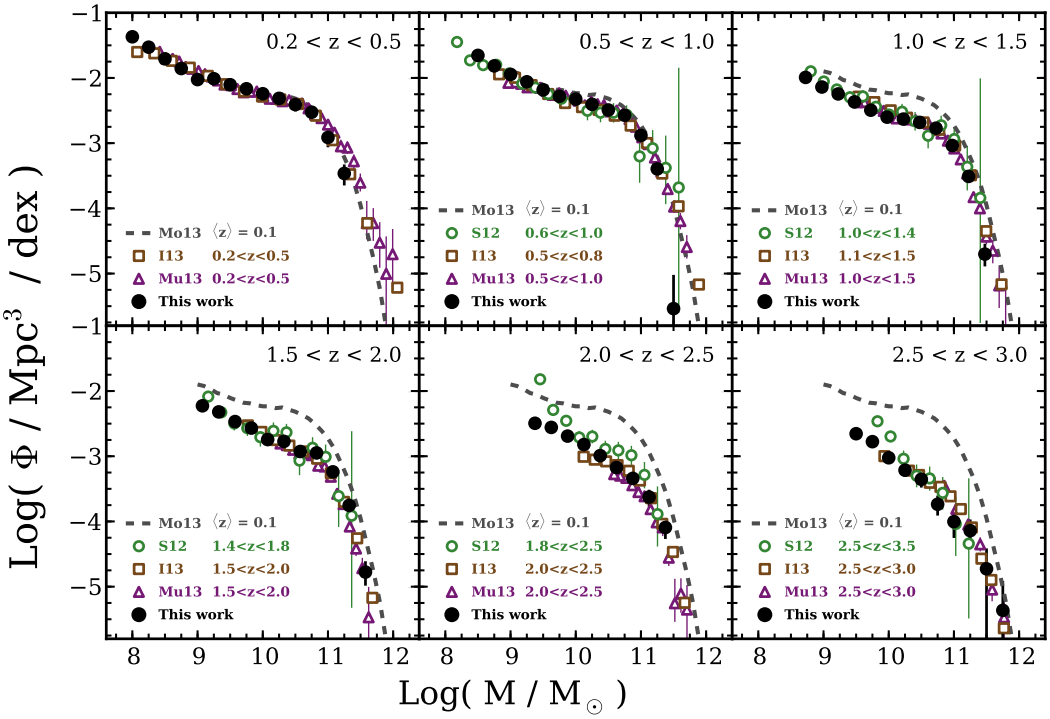

Figure 2.6: Galaxy Stellar Mass Functions: Total.
Stellar mass functions for all galaxies between $0.2 < z < 3$ with errorbars representing total 1σ uncertainties. We compare our SMFs to those from other recent studies: Moustakas et al. (2013, Mo13), Santini et al. (2012, S12), Ilbert et al. (2013, I13), and Muzzin et al. (2013, M13). Data are only shown above the reported mass-completeness limit for each study. There is excellent agreement where the SMFs overlap except with the $z > 2$ SMF from Santini et al. (2012).

Table 2.2: Stellar Mass Functions: Star-forming and Quiescent.

Star-Forming

Log(M/$M_\odot$)	$0.2 < z < 0.5$ Log(Φ)	$0.5 < z < 0.75$ Log(Φ)	$0.75 < z < 1.0$ Log(Φ)	$1.0 < z < 1.25$ Log(Φ)	$1.25 < z < 1.5$ Log(Φ)	$1.5 < z < 2.0$ Log(Φ)	$2.0 < z < 2.5$ Log(Φ)	$2.5 < z < 3.0$ Log(Φ)
8.00	$-1.42^{+0.06}_{-0.07}$	—	—	—	—	—	—	—
8.25	$-1.59^{+0.06}_{-0.07}$	$-1.60^{+0.06}_{-0.07}$	—	—	—	—	—	—
8.50	$-1.76^{+0.07}_{-0.08}$	$-1.67^{+0.05}_{-0.06}$	$-1.72^{+0.05}_{-0.06}$	—	—	—	—	—
8.75	$-1.91^{+0.07}_{-0.08}$	$-1.83^{+0.06}_{-0.06}$	$-1.88^{+0.05}_{-0.06}$	$-2.00^{+0.06}_{-0.06}$	$-2.03^{+0.06}_{-0.07}$	—	—	—
9.00	$-2.08^{+0.08}_{-0.09}$	$-1.92^{+0.06}_{-0.07}$	$-2.04^{+0.06}_{-0.06}$	$-2.16^{+0.06}_{-0.07}$	$-2.15^{+0.06}_{-0.07}$	$-2.20^{+0.05}_{-0.06}$	—	—
9.25	$-2.06^{+0.07}_{-0.08}$	$-2.09^{+0.06}_{-0.07}$	$-2.14^{+0.06}_{-0.07}$	$-2.26^{+0.06}_{-0.07}$	$-2.29^{+0.06}_{-0.07}$	$-2.32^{+0.05}_{-0.06}$	$-2.53^{+0.06}_{-0.07}$	—
9.50	$-2.17^{+0.07}_{-0.09}$	$-2.19^{+0.07}_{-0.08}$	$-2.27^{+0.06}_{-0.07}$	$-2.32^{+0.06}_{-0.07}$	$-2.48^{+0.07}_{-0.08}$	$-2.42^{+0.05}_{-0.06}$	$-2.51^{+0.06}_{-0.07}$	$-2.66^{+0.06}_{-0.07}$
9.75	$-2.25^{+0.08}_{-0.10}$	$-2.28^{+0.06}_{-0.07}$	$-2.47^{+0.07}_{-0.08}$	$-2.52^{+0.07}_{-0.08}$	$-2.55^{+0.07}_{-0.08}$	$-2.56^{+0.06}_{-0.06}$	$-2.67^{+0.06}_{-0.07}$	$-2.79^{+0.07}_{-0.08}$
10.00	$-2.36^{+0.08}_{-0.10}$	$-2.39^{+0.07}_{-0.08}$	$-2.55^{+0.08}_{-0.09}$	$-2.68^{+0.08}_{-0.09}$	$-2.68^{+0.08}_{-0.09}$	$-2.73^{+0.06}_{-0.07}$	$-2.78^{+0.07}_{-0.08}$	$-3.06^{+0.08}_{-0.09}$
10.25	$-2.50^{+0.08}_{-0.09}$	$-2.55^{+0.07}_{-0.08}$	$-2.60^{+0.07}_{-0.09}$	$-2.88^{+0.09}_{-0.10}$	$-2.75^{+0.08}_{-0.10}$	$-2.89^{+0.07}_{-0.07}$	$-3.00^{+0.08}_{-0.09}$	$-3.32^{+0.09}_{-0.11}$
10.50	$-2.63^{+0.09}_{-0.11}$	$-2.76^{+0.08}_{-0.09}$	$-2.77^{+0.08}_{-0.09}$	$-2.81^{+0.07}_{-0.09}$	$-2.87^{+0.08}_{-0.09}$	$-3.07^{+0.07}_{-0.09}$	$-3.26^{+0.09}_{-0.11}$	$-3.59^{+0.11}_{-0.14}$
10.75	$-2.91^{+0.10}_{-0.12}$	$-3.00^{+0.08}_{-0.10}$	$-2.91^{+0.09}_{-0.11}$	$-2.99^{+0.08}_{-0.10}$	$-3.07^{+0.08}_{-0.10}$	$-3.26^{+0.09}_{-0.10}$	$-3.54^{+0.11}_{-0.14}$	$-3.97^{+0.16}_{-0.20}$
11.00	$-3.43^{+0.13}_{-0.18}$	$-3.46^{+0.10}_{-0.13}$	$-3.37^{+0.10}_{-0.13}$	$-3.29^{+0.10}_{-0.13}$	$-3.39^{+0.10}_{-0.13}$	$-3.35^{+0.09}_{-0.11}$	$-3.69^{+0.13}_{-0.17}$	$-4.16^{+0.20}_{-0.28}$
11.25	$-4.39^{+0.30}_{-0.41}$	$-4.30^{+0.20}_{-0.25}$	$-4.17^{+0.16}_{-0.20}$	$-4.21^{+0.15}_{-0.20}$	$-3.95^{+0.13}_{-0.17}$	$-3.85^{+0.10}_{-0.13}$	$-4.00^{+0.13}_{-0.17}$	$-4.32^{+0.18}_{-0.29}$
11.50	—	—	—	—	$-5.17^{+0.37}_{-0.52}$	$-4.78^{+0.17}_{-0.21}$	$-4.59^{+0.15}_{-0.21}$	$-4.94^{+0.32}_{-2.00}$

Quiescent

Log(M/$M_\odot$)	$0.2 < z < 0.5$ Log(Φ)	$0.5 < z < 0.75$ Log(Φ)	$0.75 < z < 1.0$ Log(Φ)	$1.0 < z < 1.25$ Log(Φ)	$1.25 < z < 1.5$ Log(Φ)	$1.5 < z < 2.0$ Log(Φ)	$2.0 < z < 2.5$ Log(Φ)	$2.5 < z < 3.0$ Log(Φ)
8.25	$-2.41^{+0.08}_{-0.10}$	—	—	—	—	—	—	—
8.50	$-2.62^{+0.10}_{-0.11}$	$-2.42^{+0.07}_{-0.08}$	—	—	—	—	—	—
8.75	$-2.82^{+0.12}_{-0.14}$	$-2.58^{+0.07}_{-0.08}$	—	—	—	—	—	—
9.00	$-2.96^{+0.14}_{-0.16}$	$-2.77^{+0.09}_{-0.10}$	$-3.19^{+0.11}_{-0.12}$	$-3.46^{+0.12}_{-0.14}$	—	—	—	—
9.25	$-2.96^{+0.08}_{-0.10}$	$-2.75^{+0.09}_{-0.10}$	$-3.17^{+0.10}_{-0.12}$	$-3.65^{+0.15}_{-0.17}$	$-3.97^{+0.21}_{-0.24}$	—	—	—
9.50	$-2.98^{+0.09}_{-0.10}$	$-2.94^{+0.10}_{-0.11}$	$-3.33^{+0.12}_{-0.14}$	$-3.46^{+0.13}_{-0.14}$	$-3.79^{+0.17}_{-0.19}$	$-4.14^{+0.17}_{-0.19}$	—	—
9.75	$-2.91^{+0.09}_{-0.11}$	$-2.99^{+0.07}_{-0.08}$	$-3.16^{+0.11}_{-0.12}$	$-3.57^{+0.14}_{-0.16}$	$-3.75^{+0.16}_{-0.18}$	$-3.95^{+0.14}_{-0.15}$	$-3.72^{+0.11}_{-0.12}$	$-4.16^{+0.17}_{-0.20}$
10.00	$-2.86^{+0.09}_{-0.11}$	$-2.83^{+0.07}_{-0.08}$	$-3.16^{+0.11}_{-0.12}$	$-3.37^{+0.12}_{-0.14}$	$-3.45^{+0.12}_{-0.14}$	$-3.55^{+0.09}_{-0.11}$	$-3.76^{+0.11}_{-0.13}$	$-4.08^{+0.16}_{-0.18}$
10.25	$-2.78^{+0.08}_{-0.10}$	$-2.78^{+0.07}_{-0.09}$	$-2.97^{+0.08}_{-0.09}$	$-3.26^{+0.11}_{-0.13}$	$-3.52^{+0.13}_{-0.15}$	$-3.35^{+0.08}_{-0.09}$	$-3.64^{+0.11}_{-0.12}$	$-3.89^{+0.13}_{-0.15}$
10.50	$-2.80^{+0.09}_{-0.11}$	$-2.75^{+0.08}_{-0.09}$	$-2.89^{+0.08}_{-0.10}$	$-3.11^{+0.08}_{-0.09}$	$-3.24^{+0.08}_{-0.10}$	$-3.30^{+0.08}_{-0.09}$	$-3.53^{+0.10}_{-0.12}$	$-3.74^{+0.12}_{-0.15}$
10.75	$-2.76^{+0.09}_{-0.12}$	$-2.75^{+0.08}_{-0.10}$	$-2.87^{+0.09}_{-0.11}$	$-3.05^{+0.08}_{-0.10}$	$-3.23^{+0.09}_{-0.11}$	$-3.40^{+0.09}_{-0.11}$	$-3.82^{+0.13}_{-0.16}$	$-4.12^{+0.18}_{-0.22}$
11.00	$-3.07^{+0.12}_{-0.16}$	$-2.93^{+0.09}_{-0.11}$	$-3.12^{+0.10}_{-0.13}$	$-3.33^{+0.10}_{-0.13}$	$-3.46^{+0.10}_{-0.13}$	$-3.54^{+0.09}_{-0.11}$	$-4.08^{+0.17}_{-0.22}$	$-4.51^{+0.27}_{-0.38}$
11.25	$-3.52^{+0.14}_{-0.19}$	$-3.37^{+0.11}_{-0.14}$	$-3.57^{+0.12}_{-0.15}$	$-3.75^{+0.12}_{-0.16}$	$-3.95^{+0.13}_{-0.17}$	$-3.87^{+0.10}_{-0.13}$	$-4.54^{+0.15}_{-0.21}$	$-4.61^{+0.19}_{-0.32}$
11.50	—	—	—	—	$-5.47^{+0.52}_{-0.90}$	$-4.44^{+0.13}_{-0.16}$	$-4.89^{+0.19}_{-0.26}$	$-5.14^{+0.34}_{-2.00}$

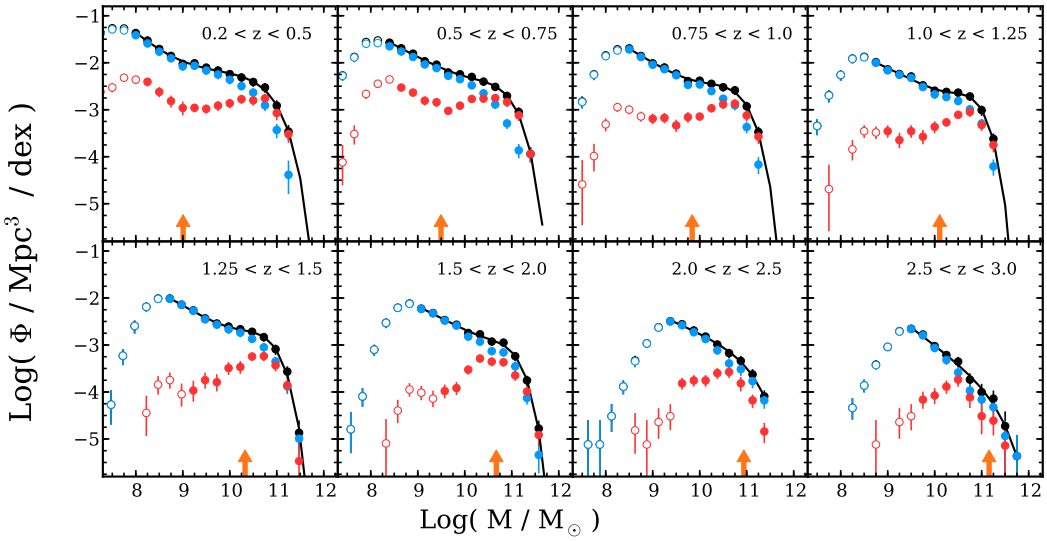

Figure 2.7: Galaxy Stellar Mass Functions: Star-forming & Quiescent. Stellar mass functions in sequential redshift bins for all (black), star-forming (blue) and quiescent (red) galaxies. Open symbols correspond to data below each subsample's respective mass-completeness limit. We have used data from NMBS to supplement the high-mass end of each SMF down to the limits indicated by the orange arrows. Best-fit Schechter functions to the total SMF are plotted as black lines. Even as far as $z \sim 2$ the total SMF exhibits a low-mass upturn. Furthermore, we show a clear decline in the quiescent SMF below M^* towards high-z, which cannot be attributed to incompleteness.

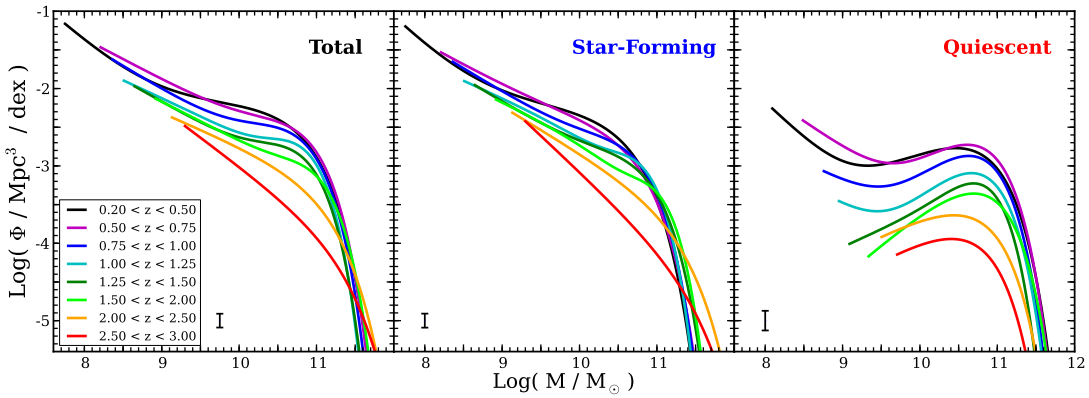

Figure 2.8: Best-fit Schechter Functions.
Evolution of our total (**left**), star-forming (**middle**) and quiescent (**right**) SMFs between $0.2 < z < 3$. For each redshift bin we only plot where we are above the corresponding mass-completeness limit. Errorbars in the lower-left of each panel show representative 1σ uncertainties that include Poisson errors, cosmic variance and SED-fitting uncertainties. Double-Schechter fits are used at $z < 2$ for the total and star-forming SMFs and at $z < 1.5$ for the quiescent SMF.

$$\Phi(M)dM = \ln(10)\ \Phi^*\left[10^{(M-M^*)(1+\alpha)}\right]\exp(-10^{(M-M^*)})dM \tag{2.3}$$

where again $M = \log(M_*/M_\odot)$, α is the slope of the power-law at low masses, Φ^* is the normalization and M^* is the characteristic mass. The double-Schechter function is defined as:

$$\begin{aligned}\Phi(M)dM &= \Phi_1(M)dM + \Phi_2(M)dM \\ &= \ln(10)\exp\left(-10^{(M-M^*)}\right)10^{(M-M^*)} \\ &\quad\times\left[\Phi_1^* 10^{(M-M^*)\alpha_1} + \Phi_2^* 10^{(M-M^*)\alpha_2}\right]dM\end{aligned} \tag{2.4}$$

where again $M = \log(M_*/M_\odot)$, $(\alpha_1,\ \alpha_2)$ are the slopes and $(\Phi_1^*,\ \Phi_2^*)$ are the normalizations of the constituent Schechter functions respectively, and M^* again is the

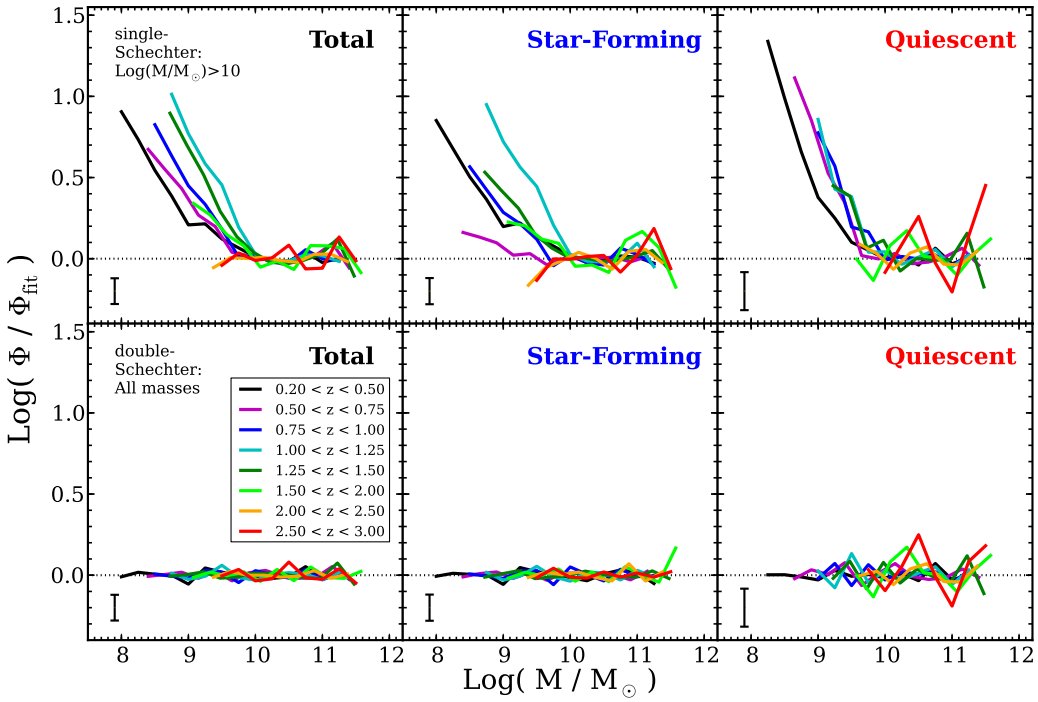

Figure 2.9: Best-fit Schechter Residuals.
Residuals from functional fits to our total, star-forming and quiescent SMFs. Errorbars in the lower-left of each panel show representative 1σ uncertainties. The top three panels correspond to single-Schechter functions fit at $\mathrm{Log}(\mathrm{M}/M_{\odot}) > 10$. Residuals here clearly show the presence of the low-mass upturn at $z < 2$ in the total and star-forming SMFs and at $z < 1.5$ in the quiescent SMF. The bottom three panels correspond to double-Schechter functions fit at all masses. Residuals here are consistent with random noise, indicating that the double-Schechter function is an accurate description of the SMF. However, although the double-Schechter function provides a good fit, a single-Schechter function is sufficient for our SMFs at $z > 2$.

characteristic mass. Note that one value for M^* is used for both constituents in the double-Schechter function. This functional form of the double-Schechter function is the same as in Baldry et al. (2008).

Recent measurements of the total SMF at $z < 1.5$ have shown that the SMF steepens at M $< 10^{10} M_{\odot}$ (e.g. Baldry et al. 2008, Li et al. 2009, Drory et al. 2009, Pozzetti et al. 2010, Moustakas et al. 2013,Ilbert et al. 2013, Muzzin et al. 2013). We fit each of our mass functions with both single- and double-Schechter functions. We show best-fit parameters as well as reduced chi-squared values for each in Tables 2.3 and 2.4. From the reduced chi-squared values we find that the total SMF is much better fit by a double-Schechter function at $z \leq 2$. At $z > 2$ we find that a single-Schechter function is sufficient, however this may be because we do not go deep enough to detect significant structure at low masses.

This is clearly shown in Figure 2.9 where we plot the residuals of both single- and double-Schechter fits to the total SMF. A prominent upturn is revealed in the top three panels where we fit single-Schechter functions at $\log(M_*/M_{\odot}) > 10$ only. In the bottom three panels we show the residuals from fitting double-Schechter functions at all masses, which are consistent within our measurement uncertainties. However, although the double-Schechter provides a good fit at all redshifts, we find that a single-Schechter works just as well at $z > 1.5$ for the quiescent SMF and at $z > 2$ for the total and star-forming SMFs. We observe the same behavior even if the NMBS data is excluded from the calculation, proving that the steepening of the low-mass slope is not caused by a systematic offset between the surveys we use. In fact there is evidence for a steepening in each of the three ZFOURGE fields independently.

Table 2.3: Best-fit double-Schechter Parameters.

Total

Redshift	$\mathrm{Log}(M^*)$	α_1	$\mathrm{Log}(\Phi_1^*)$	α_2	$\mathrm{Log}(\Phi_2^*)$	χ^2_{red}
$0.20 < z < 0.50$	10.78 ± 0.11	-0.98 ± 0.24	-2.54 ± 0.12	-1.90 ± 0.36	-4.29 ± 0.55	0.3
$0.50 < z < 0.75$	10.70 ± 0.10	-0.39 ± 0.50	-2.55 ± 0.09	-1.53 ± 0.12	-3.15 ± 0.23	0.5
$0.75 < z < 1.00$	10.66 ± 0.13	-0.37 ± 0.49	-2.56 ± 0.09	-1.61 ± 0.16	-3.39 ± 0.28	0.6
$1.00 < z < 1.25$	10.54 ± 0.12	0.30 ± 0.65	-2.72 ± 0.10	-1.45 ± 0.12	-3.17 ± 0.19	0.8
$1.25 < z < 1.50$	10.61 ± 0.08	-0.12 ± 0.49	-2.78 ± 0.08	-1.56 ± 0.16	-3.43 ± 0.23	0.3
$1.50 < z < 2.00$	10.74 ± 0.09	0.04 ± 0.62	-3.05 ± 0.11	-1.49 ± 0.14	-3.38 ± 0.20	0.8
$2.00 < z < 2.50$	10.69 ± 0.29	1.03 ± 1.64	-3.80 ± 0.30	-1.33 ± 0.18	-3.26 ± 0.23	0.4
$2.50 < z < 3.00$	10.74 ± 0.31	1.62 ± 1.88	-4.54 ± 0.41	-1.57 ± 0.20	-3.69 ± 0.28	1.3

Star-Forming

Redshift	$\mathrm{Log}(M^*)$	α_1	$\mathrm{Log}(\Phi_1^*)$	α_2	$\mathrm{Log}(\Phi_2^*)$	χ^2_{red}
$0.20 < z < 0.50$	10.59 ± 0.09	-1.08 ± 0.23	-2.67 ± 0.11	-2.00 ± 0.49	-4.46 ± 0.63	0.3
$0.50 < z < 0.75$	10.65 ± 0.23	-0.97 ± 1.32	-2.97 ± 0.28	-1.58 ± 0.54	-3.34 ± 0.67	0.3
$0.75 < z < 1.00$	10.56 ± 0.13	-0.46 ± 0.63	-2.81 ± 0.10	-1.61 ± 0.17	-3.36 ± 0.28	0.9
$1.00 < z < 1.25$	10.44 ± 0.11	0.53 ± 0.73	-2.98 ± 0.14	-1.44 ± 0.11	-3.11 ± 0.16	0.8
$1.25 < z < 1.50$	10.69 ± 0.12	-0.55 ± 0.69	-3.04 ± 0.12	-1.62 ± 0.24	-3.59 ± 0.35	0.2
$1.50 < z < 2.00$	10.59 ± 0.10	0.75 ± 0.70	-3.37 ± 0.16	-1.47 ± 0.10	-3.28 ± 0.13	0.9
$2.00 < z < 2.50$	10.58 ± 0.18	2.06 ± 1.43	-4.30 ± 0.39	-1.38 ± 0.15	-3.28 ± 0.18	0.7
$2.50 < z < 3.00$	10.61 ± 0.22	2.36 ± 1.84	-4.95 ± 0.49	-1.67 ± 0.19	-3.71 ± 0.25	0.8

Quiescent

Redshift	$\mathrm{Log}(M^*)$	α_1	$\mathrm{Log}(\Phi_1^*)$	α_2	$\mathrm{Log}(\Phi_2^*)$	χ^2_{red}
$0.20 < z < 0.50$	10.75 ± 0.10	-0.47 ± 0.20	-2.76 ± 0.09	-1.97 ± 0.34	-5.21 ± 0.48	0.2
$0.50 < z < 0.75$	10.68 ± 0.07	-0.10 ± 0.27	-2.67 ± 0.05	-1.69 ± 0.24	-4.29 ± 0.33	0.9
$0.75 < z < 1.00$	10.63 ± 0.12	0.04 ± 0.44	-2.81 ± 0.05	-1.51 ± 0.67	-4.40 ± 0.56	0.4
$1.00 < z < 1.25$	10.63 ± 0.12	0.11 ± 0.44	-3.03 ± 0.05	-1.57 ± 0.81	-4.80 ± 0.61	0.8
$1.25 < z < 1.50$	10.49 ± 0.11	0.85 ± 1.07	-3.36 ± 0.30	-0.54 ± 0.66	-3.72 ± 0.44	0.6
$1.50 < z < 2.00$	10.77 ± 0.18	-0.19 ± 0.96	-3.41 ± 0.23	-0.18 ± 1.21	-3.91 ± 0.51	1.9
$2.00 < z < 2.50$	10.69 ± 0.14	-0.37 ± 0.52	-3.59 ± 0.10	-3.07 ± 16.13	-6.95 ± 1.66	0.7
$2.50 < z < 3.00$	9.95 ± 0.23	-0.62 ± 2.63	-4.22 ± 0.41	2.51 ± 2.43	-4.51 ± 0.62	1.7

[a] In units of $M_\odot$
[b] In units of Mpc^{-3}

Table 2.4: Best-fit single-Schechter Parameters.

Total

Redshift	Log(M^*)[a]	α	Log(Φ^*)[b]	$\chi^2_{\rm red}$
$0.20 < z < 0.50$	11.05 ± 0.10	-1.35 ± 0.04	-2.96 ± 0.10	3.3
$0.50 < z < 0.75$	11.00 ± 0.06	-1.35 ± 0.04	-2.93 ± 0.07	4.6
$0.75 < z < 1.00$	11.16 ± 0.12	-1.38 ± 0.04	-3.17 ± 0.11	4.5
$1.00 < z < 1.25$	11.09 ± 0.10	-1.33 ± 0.05	-3.19 ± 0.11	4.2
$1.25 < z < 1.50$	10.88 ± 0.05	-1.29 ± 0.05	-3.11 ± 0.08	5.6
$1.50 < z < 2.00$	11.03 ± 0.05	-1.33 ± 0.05	-3.28 ± 0.08	4.5
$2.00 < z < 2.50$	11.13 ± 0.13	-1.43 ± 0.08	-3.59 ± 0.14	0.3
$2.50 < z < 3.00$	11.35 ± 0.33	-1.74 ± 0.12	-4.36 ± 0.29	1.0

Star-Forming

Redshift	Log(M^*)	α	Log(Φ^*)	$\chi^2_{\rm red}$
$0.20 < z < 0.50$	10.73 ± 0.06	-1.37 ± 0.04	-2.94 ± 0.08	2.4
$0.50 < z < 0.75$	10.79 ± 0.07	-1.42 ± 0.04	-3.04 ± 0.08	0.7
$0.75 < z < 1.00$	10.86 ± 0.07	-1.43 ± 0.04	-3.16 ± 0.09	3.0
$1.00 < z < 1.25$	10.85 ± 0.07	-1.37 ± 0.05	-3.20 ± 0.09	3.2
$1.25 < z < 1.50$	10.89 ± 0.05	-1.38 ± 0.05	-3.27 ± 0.08	2.1
$1.50 < z < 2.00$	10.97 ± 0.05	-1.45 ± 0.05	-3.44 ± 0.08	4.2
$2.00 < z < 2.50$	11.28 ± 0.19	-1.60 ± 0.08	-3.96 ± 0.19	1.3
$2.50 < z < 3.00$	11.49 ± 0.46	-1.93 ± 0.12	-4.82 ± 0.38	1.4

Quiescent

Redshift	Log(M^*)	α	Log(Φ^*)	$\chi^2_{\rm red}$
$0.20 < z < 0.50$	11.11 ± 0.14	-0.98 ± 0.07	-3.18 ± 0.10	4.1
$0.50 < z < 0.75$	11.03 ± 0.08	-0.98 ± 0.07	-3.15 ± 0.09	9.9
$0.75 < z < 1.00$	10.88 ± 0.09	-0.59 ± 0.10	-3.00 ± 0.08	2.1
$1.00 < z < 1.25$	10.84 ± 0.09	-0.47 ± 0.11	-3.16 ± 0.07	2.1
$1.25 < z < 1.50$	10.60 ± 0.04	-0.03 ± 0.14	-3.17 ± 0.05	0.9
$1.50 < z < 2.00$	10.76 ± 0.05	-0.14 ± 0.12	-3.29 ± 0.05	1.8
$2.00 < z < 2.50$	10.73 ± 0.08	-0.49 ± 0.18	-3.63 ± 0.09	0.4
$2.50 < z < 3.00$	10.65 ± 0.19	-0.43 ± 0.34	-3.92 ± 0.14	1.6

[a] In units of $M_\odot$

[b] In units of Mpc^{-3}

2.3.3 The Weakly-Evolving Shape of the Total Stellar Mass Function

The left panel of Figure 2.10 shows the best-fit values for M^* as a function of redshift. There is little statistically significant evolution in M^* at $z < 2$, in agreement with other studies (Marchesini et al. 2009, Santini et al. 2012, Muzzin et al. 2013). We note that our values of M^* are $\sim$0.2 dex lower than these previous studies. We find that this offset is the result of comparing single- versus double-Schechter fits to the SMF. The weak evolution in M^* suggests that the physical mechanism(s) responsible for the exponential cutoff in the SMF has a mass scale that is independent of redshift (see also Peng et al. 2010).

We show the best-fit values for the faint-end slope α as a function of redshift in the middle panel of Figure 2.10. We plot only the steeper slope of (α_1, α_2) which dominates at the lowest masses. We find no statistically significant evolution in the low-mass slope within our redshift range. Some evolution in alpha may be suggested when comparing to the $z \sim 0$ SMF from Moustakas et al. (2013), however we note that those authors do not probe below $10^9 M_\odot$, and thus do not strongly constrain the slope at the lowest masses. We do find better agreement with the $z \sim 0$ SMF from Baldry et al. (2012), who reach lower masses.

In the last panel of Figure 2.10 we show the redshift evolution of $\Phi_1^* + \Phi_2^*$. In contrast with the apparent constancy of M^* and α, we find clear evolution in Φ^*. Thus to rough approximation the shape of the total SMF does not evolve over $0 < z < 2$, but the normalization does. Moustakas et al. (2013) do not report parameters for functional fits to their measured SMF; therefore, we fit our own doube-Schechter function to their $z \approx 0.1$ SMF. The best-fit parameters we find for Log(M^*) , α_1, Log(Φ_1^*), α_2, Log(Φ_2^*) are 10.79, -0.74, -2.44, -1.75, -3.69 respectively.

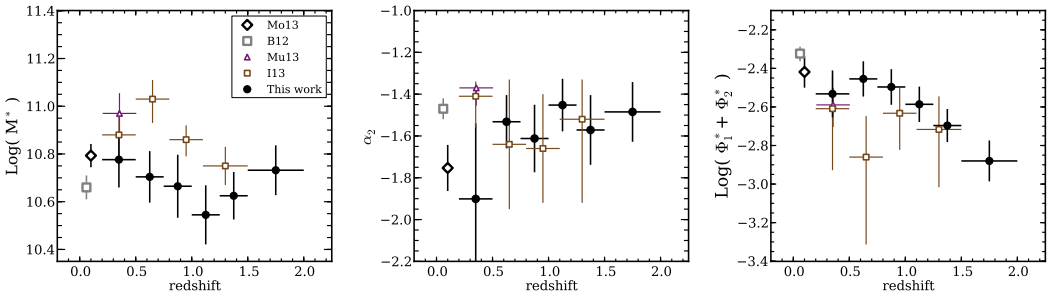

Figure 2.10: Evolution of Best-fit Schechter Parameters.
Redshift evolution in the best-fit Schechter parameters for total SMFs at all redshifts where a double-Schechter function provides a better fit. **Left:** Best-fit values for the characteristic mass M^* **Center:** Best-fit values for the low-mass slope α_2. **Right:** Sum of the best-fit values for the normalizations (Φ_1^*, Φ_2^*). For comparison we also show measurements from other studies that found the double-Schechter to provide a better fit: Moustakas et al. (2013) (Mo13), Baldry et al. (2012) (B12), Muzzin et al. (2013) (Mu13), Ilbert et al. (2013) (I13). We note that we fit a double-Schechter function to the SMF from Moustakas et al. (2013) ourselves as no such parameters were reported. The parameters we assume are given in section 2.3.3. The only statistically significant evolution we find in our data is in Log($\Phi_1^* + \Phi_2^*$) indicating that the shape of the SMF remains mostly constant but increases in normalization with time.

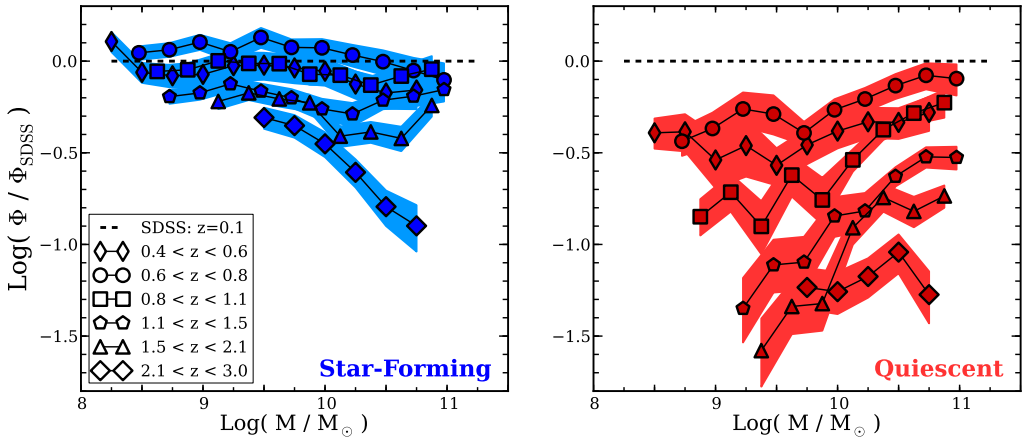

Figure 2.11: Evolution of Star-forming and Quiescent SMFs.
Growth in the star-forming (**left**) and quiescent (**right**) SMFs relative to the $z \approx 0$ star-forming and quiescent SMFs from Moustakas et al. (2013). Shaded regions show 1σ Poisson and SED-fitting uncertainties. Cosmic variance uncertainties are neglected for clarity, but range between 0.05 and 0.14 dex. Each redshift interval here at $z \geq 0.4$ has been chosen to span roughly 1.2 Gyr of galaxy evolution. We find that the growth in the number density of star-forming galaxies is remarkably uniform at $\log(M_*/M_\odot) < 10$. The quiescent SMF, however, exhibits a rapid increase towards lower stellar masses. Specifically, at $\log(M_*/M_\odot) \leq 10$ quiescent galaxies increase in number by a factor of 15 - 30 whereas star-forming galaxies increase by only a factor of 1.5 - 2. Despite the large difference in these growth rates, star-forming galaxies still remain the dominant population at low masses at all redshifts.

2.3.4 Buildup of the Star-Forming and Quiescent Populations

In Figure 2.11 we show the growth in the number density of galaxies as a function of mass in several redshift bins for the star-forming and quiescent subpopulations. We show this growth by normalizing our star-forming/quiescent SMFs to the most recent measurements of the star-forming/quiescent SMFs at $z \approx 0$ from SDSS (Moustakas et al. 2013). The redshift ranges at $z > 0.4$ in Figure 2.11 are chosen to track the evolution in similar time intervals of approximately 1.2 Gyr.

At $\log(M_*/M_\odot) < 11$, where we have sufficient statistics to trace the evolution of the mass function, we find that the SMF of star forming galaxies grows moderately with cosmic time, by 1.5 - 2.5$\times$ since $z \sim 2$. There is a hint that it actually decreases with time at $z < 0.6$. Only between $2 < z < 3$ do we observe a large jump in the number of star-forming galaxies at $\log(M_*/M_\odot) > 10$. These results are consistent with previous works which have generally found that the star-forming SMF evolves relatively weakly with redshift (Arnouts et al. 2007, Bell et al. 2007, Pozzetti et al. 2010, Brammer et al. 2011, Muzzin et al. 2013).

The growth of quiescent galaxies since $z \approx 2$ is much more rapid than that of star-forming galaxies (e.g. Arnouts et al. 2007, Bell et al. 2007). At masses greater than $10^{10} M_\odot$ we find roughly a factor of 6 increase between $z = 2$ and $z = 0$ in agreement with previous studies, however, at lower masses there is a 15 - 30$\times$ increase. This is the first clear detection of a rapid increase in the low-mass quiescent population over the past 10 billion years that is not affected by incompleteness. This rapid evolution causes the quiescent fraction to increase by about a factor of 5 for low-mass galaxies ($< 10^{10} M_\odot$) from $\approx$7% at $z = 2$ to $\approx$34% at $z = 0$.

2.3.5 Cosmic Stellar Mass Density

Obtaining a precise estimate of the integrated stellar mass density in the universe requires probing the SMF well below M^*. Most recent attempts at intermediate redshifts have been made using near-infrared selected surveys, which make it possible to define highly-complete samples down to some stellar mass limit. However if this limit does not reach significantly below M^* then the integrated stellar mass density depends on an extrapolation of the observed SMF using the best-fit Schechter parameters (e.g. Marchesini et al. 2009, Santini et al. 2012, Ilbert et al. 2013, Muzzin et al. 2013), which may be poorly constrained and may depend sensitively on the exact — and uncertain — level of completeness near the nominal mass-completeness limit.

In Figure 2.12 we show our measurements for the evolution of the cosmic stellar mass densities (ρ) of all, star-forming and quiescent galaxies. Previous studies have typically integrated best-fit Schechter functions between $8 < \log(M_*/M_\odot) < 13$, extrapolating below mass-completeness limits wherever necessary. We choose to integrate our best-fits between $9 < \log(M_*/M_\odot) < 13$ since this is only marginally below our completeness limit in our highest redshift bin. We note here that using $10^9 M_\odot$ as opposed to $10^8 M_\odot$ as a lower-limit decreases ρ by $< 5\%$.

Uncertainties are evaluated from 500 Monte Carlo simulations of the measured SMFs. For each iteration we perturb all data points using the combined uncertainties as described in section 2.2.5. We then refit Schechter functions to recalculate ρ, taking the resulting scatter as the uncertainty. We parameterize our measurements of the redshift evolution of the total stellar mass density as follows:

$$\mathrm{Log}(\rho) = a(1+z) + b \tag{2.5}$$

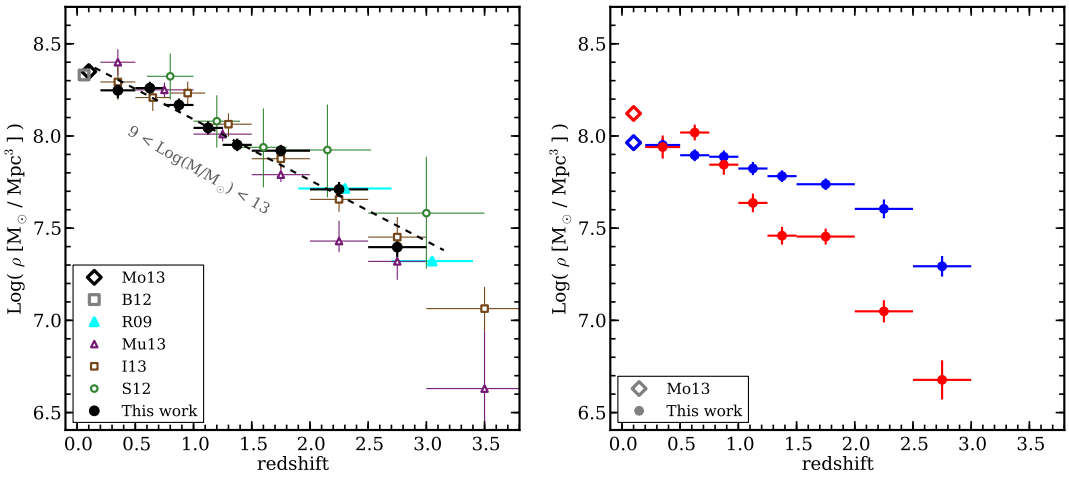

Figure 2.12: Growth of the Cosmic Stellar Mass Density.
Cosmic stellar mass densities as a function of redshift evaluated from the best-fit Schechter functions to the total SMF (**left**) and the star-forming and quiescent SMFs in blue and red respectively (**right**). We show the total stellar mass density (integrated over $9 < \log(M_*/M_\odot) < 13$) with 1σ uncertainties determined from Monte Carlo simulations on our SMFs. Other symbols show results from previous works from deep NIR surveys: black diamond; Moustakas et al. (2013) (Mo13), gray square; Baldry et al. (2012) (B12), purple triangles; Muzzin et al. (2013) (Mu13), brown squares; Ilbert et al. (2013) (I13) and green circles; Santini et al. (2012) (S12). The dashed black line is a least-squares fit to the ZFOURGE data: $\mathrm{Log}(\rho) = -0.33(1+z) + 8.75$. Also shown are high-redshift mass densities inferred from a UV-selected galaxy sample with a correction for incompleteness at low masses (cyan triangles Reddy & Steidel 2009; R09). Our measured mass densities are in good agreement with these previous works.

where ρ is the total stellar mass density in units of $M_{\odot}/\mathrm{Mpc}^3$. From a least-squares fit we find best-fit values of $a = -0.33 \pm 0.03$ and $b = 8.75 \pm 0.07$.

Figure 2.12 also shows results from recent deep and large-area surveys which are in overall agreement with our measurements. Santini et al. (2012) present results using data from CANDELS Early Release Science program in conjunction with deep ($K_s \sim 25.5$) imaging from Hawk-I. Although their work covers significantly less area than we present here (33 arcmin^2 versus 316 arcmin^2) our measurements agree within 1σ uncertainties. Measurements from the recent UltraVISTA survey (McCracken et al. 2012) which covers $\sim$1.6 deg^2 to a depth of $K_s = 23.4$ are presented in Ilbert et al. (2013) and Muzzin et al. (2013). Our results are in excellent agreement at all redshifts except $1.5 < z < 2.5$ with Muzzin et al. (2013). The difference between our result and Muzzin et al. (2013) is mostly due to the large difference in the faint end slope: Muzzin et al. (2013) measure a slope of ~ -0.9 whereas we find -1.33 for the best-fit single-Schechter function at $1.5 < z < 2.0$. Muzzin et al. (2013) note that α is not well constrained by their data, and do not rule out a low-mass slope as steep as ours.

Another estimate of the stellar mass density was provided by Reddy & Steidel (2009), who used an optically-selected sample of star-forming galaxies at $1.9 < z < 3.4$ to argue that the low-mass end of the SMF is quite steep and may have been underestimated by previous studies; they concluded that a large fraction of the stellar mass budget of the universe was locked up in dwarf galaxies. However these authors were not able to probe the SMF directly given the nature of their sample and their limited NIR and IR data, so they inferred the SMF by performing large corrections for incompleteness. Given the depth of our NIR-selected sample, we are able to probe down to similarly low masses ($\sim 10^9 M_{\odot}$) for *complete* samples.

We compare our $z > 2$ measurements to estimates based on the Reddy & Steidel

(2009) measurements in Figure 2.12. We obtain their value by integrating the SMF shown in their Fig. 12, and after converting from a Salpeter IMF (N. Reddy, private communication). The agreement is excellent, however, as noted by those authors, their sample is incomplete for galaxies with red colors. Thus the good agreement that we find is partially due to the steeper slope of their inferred SMF which is balanced by incompleteness at high masses.* Nonetheless, it is encouraging that similar results are obtained using very different types of datasets and different methods.

* Reddy & Steidel (2009) estimate that faint galaxies that lie below typical ground-based flux limits contain a roughly similar amount of mass as do the bright galaxies that are usually observed. At first glance this may seem to contradict our finding in Figure 2.12 that dwarf galaxies are sub-dominant. There are several possible explanations for this difference. One is the difference in the slopes of our SMFs (~ -1.7 versus ~ -1.4). Another is that we limit our integration to $\log(M_*/M_\odot) > 9$, where we are highly complete; if we were to integrate further down the SMF then the contribution of dwarfs would be larger. Finally, another likely contributing factor is that Reddy & Steidel (2009) select their sample based on the rest-frame UV emission; because of the weak correlation between stellar mass and UV emission, it is expected that UV-faint galaxies that lie below typical flux limits should still contain significant stellar mass.

3. THE SFR$-M_*$ RELATION AND EMPIRICAL STAR FORMATION HISTORIES AT $0.5 < Z < 4$

3.1 Background Information

Over the past two decades our understanding of the buildup of stellar matter in the universe has advanced markedly through a wealth of multiwavelength galaxy surveys (for a review see Madau & DIckenson 2014). However, inferring star formation and mass growth histories of individual galaxies is a non-trivial undertaking, and a variety of methods have been used in the literature. One class of methods involves archeological studies of nearby galaxies, either by studying resolved stellar populations or by detailed modeling of high signal-to-noise spectra (e.g. Dolphin et al. 2003, Heavens et al 2004, Thomas et al. 2005). However degeneracies in age, metallicity, and extinction complicate modeling with these techniques. Furthermore, these techniques become difficult or impossible to apply at appreciable redshifts.

This has provided the motivation for "lookback" studies of galaxy evolution: techniques which utilize observed relations of galaxies at discrete epochs in the universe to infer how individual galaxies evolve. One such type of study is to trace the mass-growth of galaxies selected in bins of constant cumulative co-moving number density (e.g. van Dokkum et al. 2010, Papovich et al. 2011, Patel et al. 2013). This method assumes that the ordering of a population of galaxies by stellar mass does not change as they evolve with time. In reality this rank-ordering *will* change due to mergers and stochastic variations in star-formation rates, but it is possible to approximately correct for these effects using an evolving number density criterion (Leja et al. 2013, Behroozi et al. 2013).

Another type of "lookback" study involves using the observed correlation between

stellar mass and star-formation rate, hereafter referred to as the SFR$-M_*$ relation (e.g. Brinchmannet al. 2004, Noeske et al. 2007, Gilbank wt al. 2011, Whitakeret al. 2012, Speagle et al. 2014). By tracing along this evolving star-forming sequence it is possible to predict how galaxies should evolve due to star-formation (e.g. Leitner 2012, Speagle et al. 2014). In general some disagreement between this approach and the number density selection (NDS) is expected since the former does not include growth due to mergers; indeed, Drory & Alverez (2008) use this difference to derive the merger rate. Disagreements may also be caused by systematic errors in mass and/or SFR estimates, as emphasized by Weinmann et al. (2012) and Leja et al. (2015).

The most commonly used parameterization for the SFR$-M_*$ relation throughout literature has been a power law of the form $\log(\Psi) = \alpha \log(M_*) + \beta$ with α and β representing the slope and normalization respectively. At low stellar masses ($< 10^{10}$ $M_\odot$) this slope needs to be close to unity in order to maintain the roughly constant low-mass slope in the observed galaxy stellar mass function (SMF). Many early studies, however, typically find a significantly shallower slope (see Table 4 of Speagle et al. 2014). Furthermore, Leja et al. (2015) argue that the sequence must also flatten at higher masses in order to be consistent with the SMF. Fortunately, recent new measurements of the SFR$-M_*$ relation find it to be more consistent with this picture (Whitaker et al. 2014, Lee et al. 2015, Schreiber et al. 2015).

Many early works relied on estimating SFRs from rest-frame UV with assumed correction factors to account for extinction from dust. The launch of the *Spitzer* Space Telescope (Werner et al. 2004) for the first time allowed us to directly probe the attenuated UV light of star-forming regions in galaxies emitted in the far-IR for statistically large samples of galaxies at $z > 1$. However, due to technical challenges, data quality in the far-IR were much poorer than in the optical/near-IR. The launch

of the *Herschel* Space Observatory (Pilbratt et al. 2010) expanded observational studies in the far-IR with improved data quality at longer wavelengths. Combinations of *Spitzer* and *Herschel* data make it possible to constrain IR SEDs for large enough samples of galaxies to complement modern optical/near-IR galaxy surveys (e.g. Elbaz et al. 2011, Wuyts et al. 2011).

Utilizing the FourStar Galaxy Evolution Survey (ZFOURGE) in concert with deep far-IR imaging from *Spitzer* and *Herschel* we perform a new analysis of the two "lookback" studies mentioned earlier. The longer wavelength data from *Spitzer* and *Herschel* allow for robust SFR measurements. Combining this with accurate photometric redshifts and deep stellar mass functions provided by ZFOURGE leads to improved constraints on the evolution of the SFR$-M_*$ relation and galaxy growth histories. With this dataset we present new measurements of the evolving SFR$-M_*$ sequence.

3.2 Data and Methods

3.2.1 ZFOURGE

The FourStar Galaxy Evolution Survey (ZFOURGE*) is a deep near-IR survey conducted with the FourStar imager (Persson et al. 2013) covering one 11' $\times$11' pointing in each of the three legacy fields CDF-S (Giacconi et al. 2002), COSMOS (Capak et al. 2007) and UDS (Lawrence et al. 2007) reaching depths of $\sim$26 mag in J_1, J_2, J_3, and $\sim$25 mag in H_s, H_l, and K_s (5σ in d=0.″6 apertures). The medium-bandwidth filters utilized by this survey offer spectral resolutions $\lambda/\Delta\lambda \approx 10$, roughly twice that of their broadband counterparts. This increase provides for finer sampling of the Balmer/4000Å spectral break at $1 < z < 4$, leading to well-constrained photometric redshifts. In combination with ancillary imaging, the full photometric dataset

* http://zfourge.tamu.edu

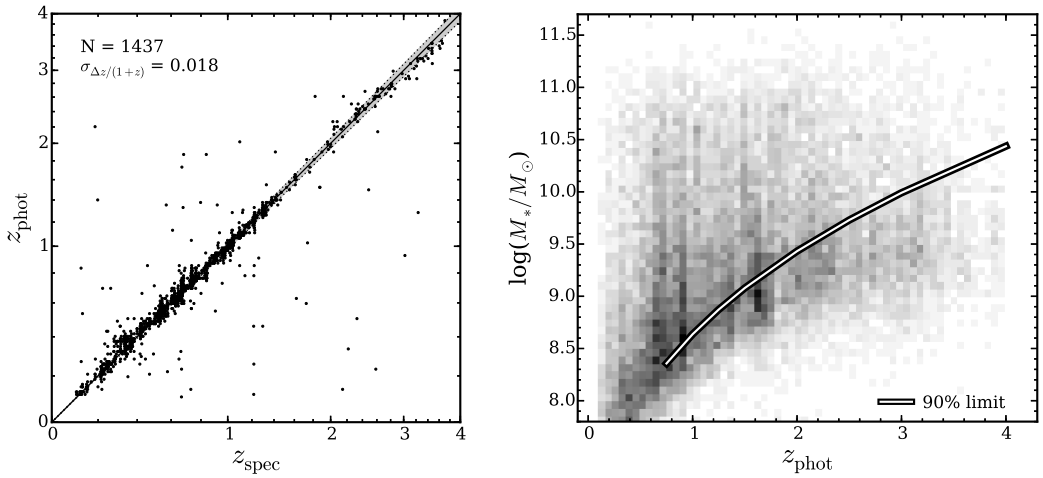

Figure 3.1: Redshift Accuracy and Stellar Mass Completeness.
Left: Comparison of spectroscopic to photometric redshifts for 1437 objects with secure spectroscopic detections. We estimate the NMAD scatter of $\Delta z/(1+z_{\rm spec})$ to be 0.018 as shown by the gray shaded region. **Right:** Stellar mass vs. photometric redshift for galaxies with S/N > 5 in the K_s band. The solid line shows our estimated 90% mass-completeness limit obtained by estimating the distribution of M/L ratios of galaxies that are slightly above the ZFOURGE magnitude limit $K_s = 25$ and assuming the distribution is similar at the magnitude limit.

covers the observed $0.3-8\mu$m wavelength range.

3.2.2 Redshifts and Stellar Masses

Photometric redshifts and rest-frame colors were measured using the public SED-fitting code `EAZY` (Brammer et al. 2008) on PSF-matched optical-NIR photometry. `EAZY` utilizes a default set of six spectral templates that include prescriptions for emission lines derived from the PEGASE models (Fioc & Rocca-Volmerange 1997) plus an additional dust-reddened template derived from the Maraston (2005) models. Linear combinations of these templates are fit to the $0.3-8\mu$m photometry for each galaxy to estimate redshifts. A comparison of our derived photometric redshifts to a sample of 1437 galaxies with secure spectroscopic redshifts is shown in Figure 3.1. We calculate a scatter of $\Delta z\ /\ (1+z_{\rm spec}) = 1.7\%$ at $z < 1.5$ and fraction of catastrophic outliers ($|\Delta z/(1+z_{spec})| > 0.15$) of 2.7%. At $z > 1.5$ these rise to 2.2% and 9% respectively. An additional analysis of $z_{\rm phot}$ accuracy can be found in section 2 of Kawinwanichakij et al. (2014). Spectroscopic redshifts from CDF-S are taken from Vanzella et al. (2008), LeFevre et al. (2005), Szokoly et al. (2004), Doherty et al. (2005), Popesso et al. (2009), and Balestra et al. (2010). For COSMOS spectroscopic redshifts come from Lilly et al. (2009) and Trump et al. (2009). Spectroscopic redshifts for UDS come from Simpson et al. (2012) and Smail et al. (2008).

Stellar masses were derived by fitting stellar population synthesis templates to the $0.3-8\mu$m photometry using the SED-fitting code `FAST` (Kriek et al. 2009). `FAST` was run using a grid of Bruzual & Charlot (2003) models assuming a Chabrier (2003) IMF with solar metallicity. Exponentially declining star-formation histories ($\Psi \propto e^{-t/\tau}$) are used with $\log(\tau/\mathrm{yr})$ ranging between $7-11$ in steps of 0.2 allowing $\log(\mathrm{age/yr})$ to vary between $7.5-10.1$ in steps of 0.1. A Calzetti (2000) extinction

law is also incorporated with values of A_V varying between $0 - 4$ in steps of 0.1.

Mass-completeness limits are estimated using a method similar to Quadri et al. (2012). Briefly, we estimate the distribution of mass-to-light ratios of galaxies that are somewhat above our $K_s = 25$ magnitude limit, and use this distribution to estimate the 90% mass-completeness limit of galaxies at $K_s = 25$. These mass-completeness limits are shown in Figure 3.1 along with the distribution of stellar masses and redshifts of galaxies in the ZFOURGE catalogs.

3.2.3 Spitzer and Herschel

We make use of *Spizer*/MIPS (GOODS-S: PI Dickinson, COSMOS: PI Scoville, UDS: PI Dunlop) and *Herschel*/PACS data (GOODS-S: PI Dickinson, COSMOS & UDS: Elbaz et al. 2011) for measuring total infrared luminosities (L_{IR}) for deriving SFRs. Imaging from these observatories used in this study include 24, 100 and 160μm. The relative depth between each image for a given field is approximately constant, though we note that the CDF-S field is roughly $2-3$ times deeper than COSMOS and UDS. Median 1σ flux uncertainties for CDF-S/COSMOS/UDS are approximately 3.9/10.3/10.1 μJy in the 24μm imaging, 0.20/0.43/0.45 mJy in the 100μm imaging and 0.35/0.70/0.93 mJy in the 160μm imaging respectively.

Due to the large PSFs of the MIPS/PACS imaging (FWHM $>$ 4") source blending is a considerable effect. As such is the case, we utilize the Multi-Resolution Object PHotometry oN Galaxy Observations (MOPHONGO) code written by I. Labbé to extract deblended photometry in these far-IR data (for a detailed discussion see Labbé et al 2006, Wuyts et al. 2007). The algorithm uses higher resolution imaging to generate a segmentation map containing information on the locations, sizes and extents of objects. In this work we use deep K_s band as the prior (FWHM = 0.46"). Point-sources coincident in both images are used to construct a convolution kernel

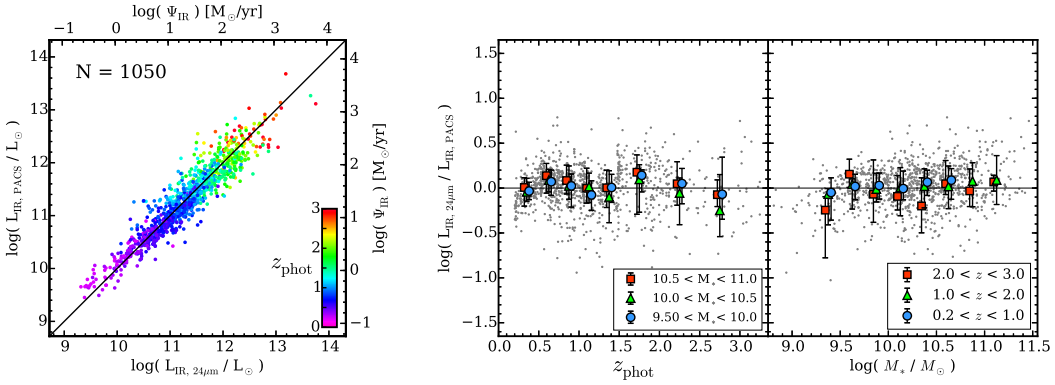

Figure 3.2: Measuring Infrared Luminosities.
Comparison between the estimated rest-frame $L_{IR}(8-1000\mu m)$ based on MIPS-only versus PACS-only data. L_{IR} is obtained by scaling the IR template presented by Wuyts et al. (2008) to the MIPS 24μm data ($L_{IR,\,24\mu m}$) or PACS 100 and 160μm data ($L_{IR,\,PACS}$) respectively for individually detected galaxies (see section 3.3 for more details). Only galaxies with S/N > 3 in all three bandpasses are considered for this comparison. In general we obtain consistent estimates for L_{IR} across a broad range of redshift and stellar mass as shown in the two **right** panels ($m_\star \equiv \log(M_*/M_\odot)$).

that maps between the high and low resolution PSFs. Objects used to construct this kernel need to be hand selected as many point-sources in the K_s imaging are frequently undetected at far-IR wavelengths. A model of each far-IR image is generated by convolving the high-resolution segmentation map with the corresponding kernel allowing the intensities of individual objects to vary freely. Background and RMS maps are generated locally for each object on scales that are three times the 30" tile-size used. By subtracting the modeled light of neighboring sources, "cleaned" image tiles of individual objects are produced which will be used in the stacking analysis discussed in the following section.

3.2.4 Sample Selection and Stacking

Modern near-infrared galaxy surveys have made it possible to detect large mass-complete samples of galaxies to high redshifts ($z \approx 4$). Unfortunately however,

imaging used to probe obscured star-formation (typically far-IR and radio) rarely ever reach complementary depths. Thus, many studies over the past several years have turned to measuring SFRs from stacked data in order to compensate for this disparity (e.g. Dunne et al. 2009, Rodighiero et al. 2010, Karim et al. 2011, Whitaker et al. 2014, Schreiber et al. 2015). Stacking has the advantage of increasing the sensitivity of SFR metrics for samples of galaxies with low levels of star-formation. However it is important to keep in mind that the interpretation of stacked results may be complicated by the fact that the intrinsic distribution of SFRs may not be unimodal or symmetric.

We classify galaxies as either actively star-forming or quiescent using the UVJ color-color diagram (Labbé et al. 2005, Wuyts et al. 2007, Williams et al. 2009). The rest-frame (U−V) and (V−J) colors are estimated using `EAZY` (section 3.2.2) The advantage of this diagram is that it effectively separates the two reddening vectors caused by aging and dust extinction, decreasing the likelihood of dust-enshrouded star-forming galaxies being identified as quiescent. The UVJ diagram is thus a more effective tool for categorizing galaxies into star-forming and quiescent subsamples than a simple color-magnitude criterion.

The deep near-IR photometry ($K_s \approx 25$) of ZFOURGE allows us to reliably select galaxies based on stellar mass. Across the entire redshift range considered in this work ($0.5 < z < 4$) we detect 8,290 galaxies in the K_s band imaging that lie above our estimated mass-completeness limits. From this mass-complete sample, we find that 2,990 (36%), 5,027 (61%) and 5,160 (62%) are not detected in the 24, 100 and 160μm images respectively (where detection is defined as S/N > 1). As such, we resort to stacking of the far-IR photometry for our K_s-selected sample in order to more precisely measure fluxes for ensembles of galaxies. In bins of redshift and stellar mass, we average-combine the "cleaned" image tiles (see section 3.2.3) of individual galaxies

for each of the far-IR bandpasses. Stacking of "cleaned" imaging has been shown to significantly improve constraints on background estimation (see also Fumagalli et al. 2014 and Whitaker et al. 2014). Finally, photometry is measured in apertures of 3.5", 4.0", and 6.0" for the 24, 100 and 160μm respectively with a background subtraction as measured from an annulus of radii 15"$-$19" on each stack. PSFs generated from bright objects and used to derive aperture corrections of 2.21, 1.76, and 1.61 respectively for the 24, 100 and 160μm imaging. Because these PSFs were constructed on the same 30" tile-size these are not corrections to total flux, thus, we adopt additional correction factors of 1.2, 1.38, and 1.54 to account for flux that falls outside the tile. In order to estimate the error on the mean flux measured for each stack we perform 100 bootstrap resamplings on each mass-redshift subsample. It is worth mentioning that fluxes measured from stacking are subject to biases due to the clustering of galaxies. However, detailed simulations have shown this effect to be negligible at the image resolution of our dataset (Viero et al. 2013, Schreiber et al. 2015).

We remove sources suspected of being dominated by active galactic nuclei (AGN) from all samples based on radio, X-ray and IR indicators. Radio AGN are identified as sources with 1.4 GHz excess having $\Psi_{1.4}/\Psi_{\rm IR} \geq 3$ where $\Psi_{1.4}$ is the radio-inferred SFR based on equation 6 of Bell (2003) and $\Psi_{\rm IR}$ is the IR-inferred SFR discussed in section 3.2.5. Unobscured X-ray AGN are identified as having $10^{42} \leq {\rm L_X} \leq 10^{44}$ and ${\rm HR} < -0.2$ where $\rm L_X$ and HR are the rest-frame X-ray luminosity in erg/s and hardness ratio respectively. Infrared AGN are identified based on an adaptation from the criteria of Messias et al. (2012) and will be presented in more detail in Cowley et al. (in prep).

3.2.5 Star-Formation Rate Measurements

We calculate total star-formation rates by adding contributions from UV and IR light. This approach assumes that the IR emission of galaxies (L_{IR}) originates from dust heated by the obscured UV light of young, massive stars. Thus by adding its contribution to that of the unobscured UV luminosity (L_{UV}) the total SFR for galaxies can be calculated. We use the conversion from Bell et al. (2005) scaled to a Chabrier (2003) IMF to derive SFRs from our data:

$$\Psi_{\rm UV+IR}\,[M_\odot/{\rm yr}] = 1.09 \times 10^{-10}\,(L_{\rm IR} + 2.2 L_{\rm UV}) \tag{3.1}$$

where L_{IR} is the integrated $8-1000\mu$m luminosity and $L_{UV} = 1.5\,\nu\,L_{\nu,2800}$ represents the rest-frame 1216$-$3000Å luminosity, both in units of $L_\odot$.

We estimate bolometric infrared luminosities ($L_{IR} \equiv L_{8-1000\mu m}$) by fitting an IR spectral template to the stacked 24-160μm photometry. The template introduced by Wuyts et al. (2008), hereafter referred to as the W08 template, was constructed by averaging the logarithm of the spectral template library from Dale & Helou (2002) motivated by results from Papovich et al. (2007). Muzzin et al. (2010) demonstrate the validity of this luminosity-independent conversion by comparing SFRs derived from Hα versus 24μm fluxes for a sample of galaxies at $z \sim 2$. Furthermore, Wuyts et al. (2011) find that at $0 < z < 3$ that this luminosity-independent conversion yields consistent L_{IR} estimates from 24μm when compared to L_{IR} derived from PACS photometry from the *Herschel* PEP survey (Lutz et al. 2011). For our stacking analysis, we smooth the W08 template by the redshift distribution of the associated galaxies for each mass-redshift bin prior to fitting.

We test the W08 template against the present dataset using a sample of 1050 well-detected galaxies (S/N $>$ 3 in all FIR bands). For each galaxy we fit the W08 template separately to the MIPS (24μm) and the PACS (100+160μm) photometry. In Figure 3.2 we show a comparison between the MIPS-only and PACS-only cases. Although we observe a general scatter of $\sim$0.2 dex we find an overall consistency with no dominant systematic trends. Even when subsampling in redshift and stellar mass the mean offset is nearly always within the scatter. We do note, however, the presence of a weak systematic trend with redshift in the middle panel of Figure 3.2 which is likely caused by various PAH features shifting through the MIPS 24μm passband. Nevertheless, the consistency between the MIPS-only and the PACS-only estimates of L_{IR} suggests that the W08 template effectively describes the average IR SED of galaxies. It further suggests that reasonably reliable SFR estimates can be made with just a single IR band.

3.3 The SFR$-M_*$ Relation

In Figure 3.3 we show our measurements of the SFR$-M_*$ relation for all galaxies in eight redshift bins spanning $0.5 < z < 4$. Evaluating completeness limits for Ψ_{UV+IR} is complicated since the depth of the far-IR imaging in CDF-S is deeper than in COSMOS and UDS. Furthermore, the ratio of IR to UV flux (infrared excess: IRX $\equiv L_{IR}/L_{UV}$) is strongly correlated with mass (e.g. Papovich et al. 2006), therefore, the completeness in Ψ_{UV+IR} will also be a function of stellar mass. Thus, to provide a visual guide in Figure 3.3 we plot the 1σ MIPS 24μm flux uncertainty converted to Ψ_{IR} as horizontal dashed lines. Due to the different depths in the three fields we use the average of the estimated 1σ flux variances in each of the fields for this conversion: $^1/_3\sqrt{3.9^2 + 10.3^2 + 10.1^2} = 6\mu$Jy. We then scale the W08 template to this flux value, shifted to the upper redshift of each bin to calculate approximate limiting SFRs.

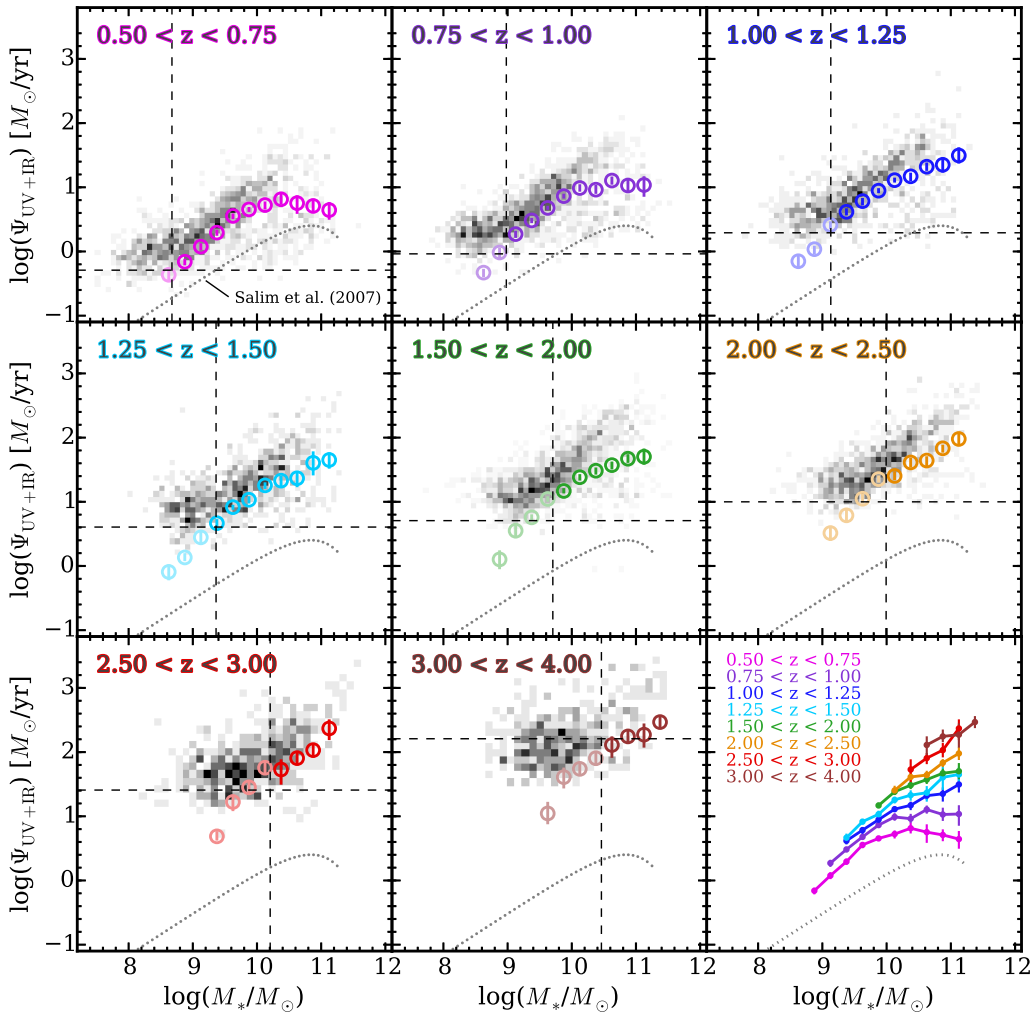

Figure 3.3: SFR$-M_*$ Relations.
Star-formation rate vs. stellar mass relations for all galaxies. Colored points represent stacked SFRs whereas the gray-scale shows the distribution of 24μm-detected galaxies ($\equiv$ S/N$_{24\mu\mathrm{m}}$ $>$ 1). Vertical and horizontal dashed lines show estimated mass-completeness limits and median 1σ 24μm flux uncertainties respectively. The final panel shows all stacked measurements above the estimated mass-completeness limits. The dotted line is the $z \approx 0.1$ measurement from Salim et al. (2007).

Errorbars on stacked SFRs are determined from 100 bootstrap resamplings of the respective UV+IR stacks described earlier.

3.3.1 Comparison to Literature

In Figure 3.4 we compare our SFR$-M_*$ relation to recent results from the literature The various SFR$-M_*$ relations come from Rodighiero et al. (2010), Karim et al. (2011), Whitaker et al. (2014), Speagle et al. (2014), and Schreiber et al. (2015). All works have been scaled to a Chabrier (2003) IMF for consistency. Overall there is broad agreement among all of the measurements presented in Figure 3.4. For the full sample of galaxies (star-forming and quiescent), the median inter-survey discrepancy at fixed stellar mass is 0.2, 0.17, 0.15, 0.16, 0.21, and 0.13 dex in the redshift bins $(0.5 < z < 1)$, $(1 < z < 1.5)$, $(1.5 < z < 2)$, $(2 < z < 2.5)$, $(2.5 < z < 3)$, and $(3 < z < 4)$ respectively. For the star-forming sample these median discrepancies are 0.24, 0.17, 0.32, 0.17, 0.30, and 0.17 dex respectively. Differences of this order are comparable to variations in stellar mass estimates produced by SED fitting assuming different stellar population synthesis models (Conroy 2013).

We do note, however, that at $> 10^{10.5}$ $M_\odot$ in the two highest redshift bins for the full sample our SFRs are systematically below the others. This offset goes away when we recalculate $\Psi_{\rm UV+IR}$ from our sample excluding the *Herschel* PACS 100 & 160μm photometry but keeping the *Spitzer* MIPS 24μm photometry. In Figure 3.5 we further investigate the impact that the *Herschel* PACS imaging has on SFRs estimated from stacks. For this comparison we only consider star-forming galaxies. We first perform an internal comparison where we calculate $\Psi_{\rm UV+IR}$ both including and excluding the *Herschel* stacks. Interestingly we find a systematic trend wherein the SFRs of higher mass galaxies tend to be overestimated when relying on the MIPS 24μm stacks alone for the IR contribution. This result contrasts what was

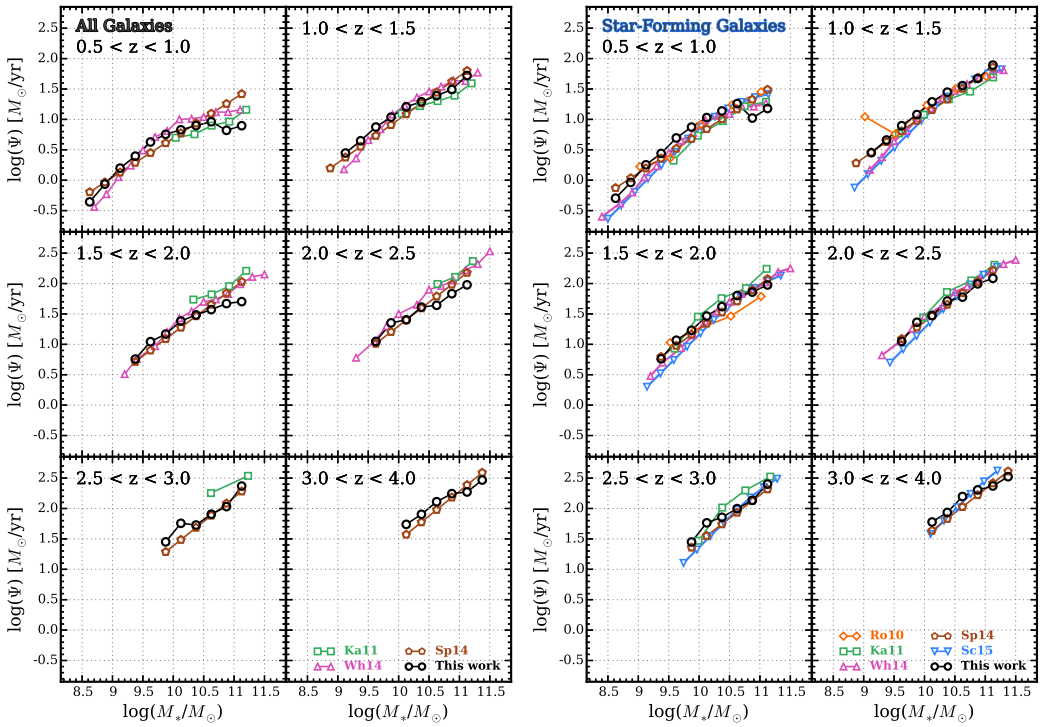

Figure 3.4: Comparing SFR$-M_*$ Relations to Literature.
Comparison of our SFR$-M_*$ relations to recent measurements from literature that also employ stacking approaches: Rodighiero et al. (2010, R10), Karim et al. (2011, K11), Whitaker et al. (2014, Wh14), Speagle et al. (2014, Sp14), and Schreiber et al (2015, Sc15). Panels on the **left** correspond to the full galaxy sample whereas panels on the **right** correspond to the active star-forming galaxies. All sequences shown here have been converted to a Chabrier (2003) IMF. Curves for the Schreiber et al. (2015) relations come from their parameterization evaluated at the central redshift of each bin shown here (see their section 4.1). Similarly, the curves for Speagle et al. (2014) correspond to parameterizations from their Table 9: "All" and "Mixed" for the all- and star-forming galaxy samples shown here. We also note that the redshift bins of the Karim et al. (2011) relations are different than those indicated at the top: $0.6 < z < 0.8$, $1.0 < z < 1.2$, $1.6 < z < 2.0$, $2.0 < z < 2.5$, and $2.5 < z < 3.0$ respectively.

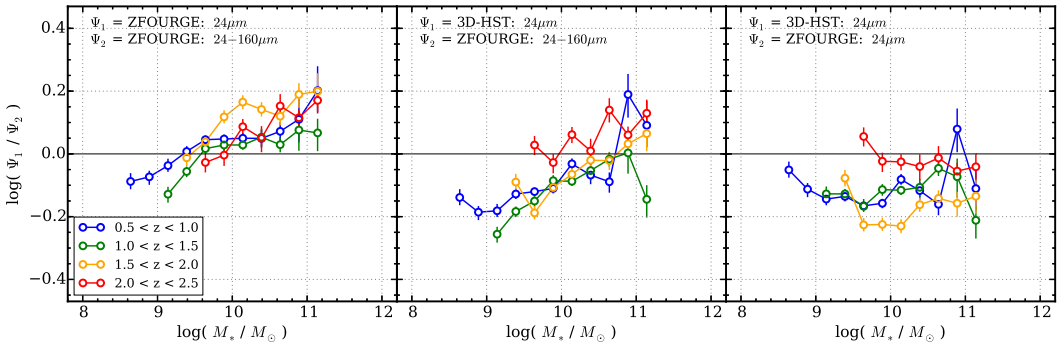

Figure 3.5: Comparing Effects of 24μm vs. 100-160μm Photometry on L_{IR}. Comparison of stacked UV+IR star-formation rates using 24−160μm vs. 24μm−only photometry. Only UVJ-selected star-forming galaxies are considered for this comparison. The **left** panel shows an internal comparison from the present dataset and reveals a clear trend where the estimated star-formation rates of more massive galaxies (typically with higher L_{IR}) decrease when including PACs photometry. This result is at odds with our findings for individually FIR-detected galaxies (see Fig. 3.2) implying that galaxies with low L_{IR} have different infrared SEDs than galaxies with high L_{IR}. The **middle** panel shows a similar systematic trend for an external comparison of our UV+IR SFRs (24−160μm) to those of 3D-HST (Whitaker et al. 2014) which only utilize 24μm photometry in the IR. Finally, the panel on the **right** shows the comparison of 24μm-only UV+IR star-formation rates.

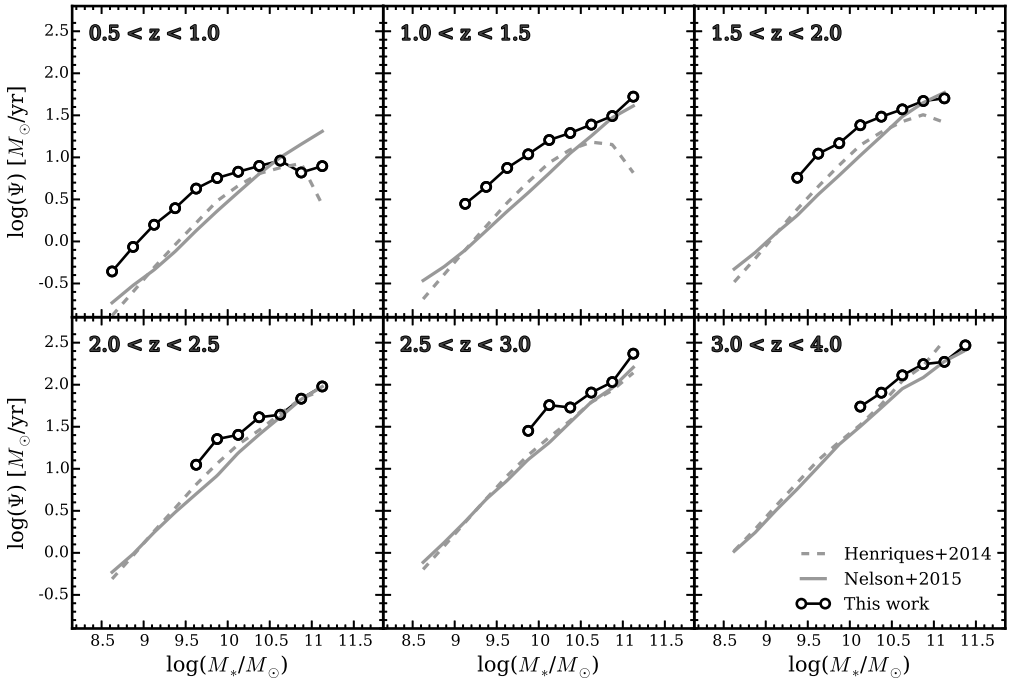

Figure 3.6: Comparing SFR$-M_*$ Relations to Simulations.
Comparison of our measured SFR$-M_*$ relations of all galaxies (black points) to those of recent cosmological simulations. The solid and dashed gray lines show mean star-formation rates of galaxies in bins of stellar mass from the Illustris-1 simulation (Nelson et al. 2015) and the Munich galaxy formation model (Henriques et al. 2014) respectively. At $\log(M_*/M_\odot) < 10.5$ the simulations produce SFR$-M_*$ relations with a very similar slope to the observations, although with a distinct offset to lower SFR at fixed stellar mass. Similar to Sparre et al. (2015), we find this offset ranges from 0.27 to 0.45 dex and decreases with redshift.

found for galaxies that are individually detected in the far-IR images which show no strong evidence of a systematic trend (see Fig. 3.2). This suggests that the fainter, non-detected galaxies have SEDs that are not consistent with their more luminous counterparts (Muzzin et al. 2010, Wuyts et al. 2011). Nevertheless, this discrepancy is not dominant, but comparable to the level of scatter between surveys noted earlier (< 0.2 dex).

The differences between the 24μm-derived star-formation rates for 3D-HST and ZFOURGE are particularly interesting. These surveys cover the same fields (although ZFOURGE only covers half the area), rely on much of the same public imaging in the optical and IR bands, have had photometry performed using similar methods, and use the same conversions to calculate the star-formation rate from the 2800Å and 24μm flux. Thus the systematic differences in star-formation rates are indicative of the minimal differences that can be expected in inter-survey comparisons.

Lastly, in Figure 3.6, we compare our measured SFR$-M_*$ relations for the full sample with results from a recent hydrodynamic simulation (Illustris: Nelson et al. 2015) and the semi-analytic Munich galaxy formation model (Henriques et al. 2014). Gray lines correspond to the mean SFR in bins of stellar mass for each redshift interval indicated. Except at $\log(M_*/M_\odot) > 10.5$, both simulations are consistently in good agreement with each other (for further discussion of this point see Weinmann et al. 2012). In general, the simulations reproduce the roughly constant slope at $M_* < 10^{10}\ M_\odot$ albeit with an offset. This offset ranges between $0.17 - 0.45$ dex at fixed stellar mass and decreases with redshift (Sparre et al. 2015). At higher masses, however, Illustris and the Munich galaxy formation model tend to under-predict and over-predict the strength of the turnover at $z < 2$ respectively.

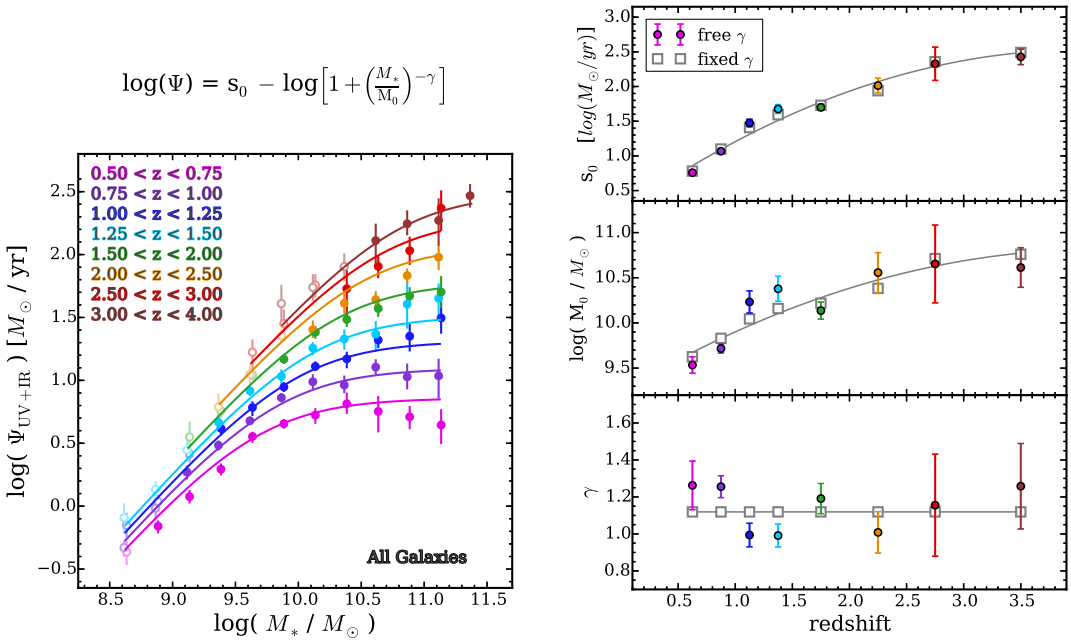

Figure 3.7: Parameterizing the SFR$-M_*$ Relation: All Galaxies. Our parameterization for the redshift evolution of the SFR$-M_*$ sequence of all galaxies. We start with Equation 3.2 (shown in the upper left) which is described by three free parameters: a power-law of slope γ at low masses which asymptotically approaches a peak star-formation rate s_0 at high masses with M_0 being the transition mass between the two behaviors. On the **right** we show these best-fitting parameters vs. redshift and results from the fitting procedure described in section 3.3. The panel on the **left** shows the the corresponding redshift-parameterized SFR$-M_*$ relations at the central redshift of each bin with points showing the stacked measurements from Figure 3.3.

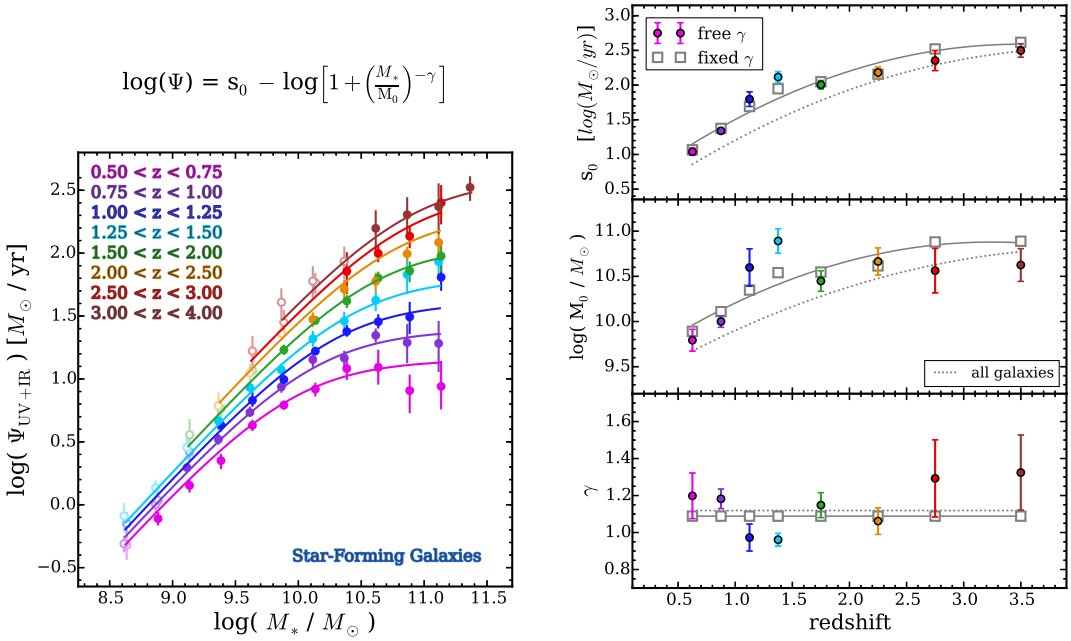

Figure 3.8: Parameterizing the SFR$-M_*$ Relation: Star-Forming Galaxies. Same as Figure 3.7 but for UVJ-selected star-forming galaxies only. Evolution in M_0 is still apparent indicating that this behavior is not driven exclusively by the buildup of massive quiescent galaxies at low redshift.

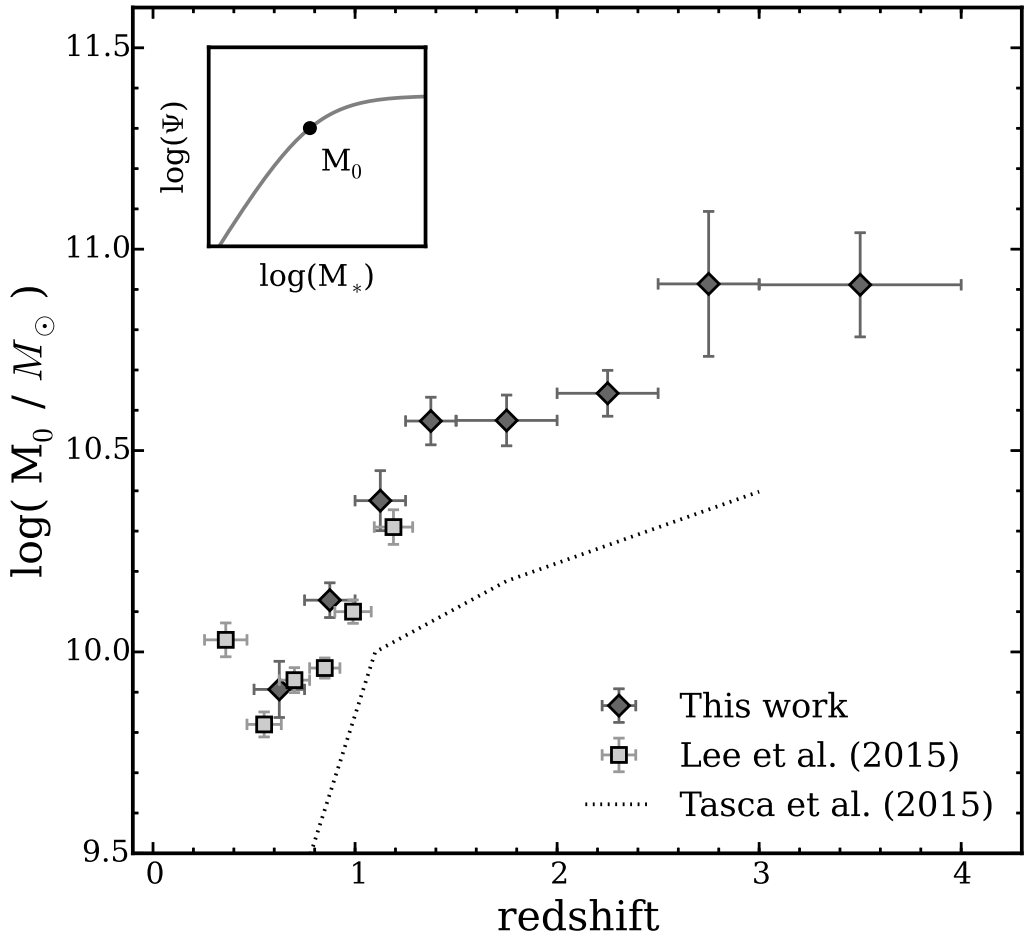

Figure 3.9: Evolution of the Turnover Mass.
Evolution of the turnover mass (M_0) in the SFR$-M_*$ relation of star-forming galaxies. An illustration of the location of M_0 as defined in equation 3.2 is shown in the upper left. Results shown from this work are from the "fixed γ" fitting procedure ($\gamma = 1.08$). The statistical significance of of our measured correlation is markedly high (Pearson correlation coefficient of $r = 0.92$). Also shown are recent measurements from literature. There is excellent agreement at the overlapping redshifts between our measurements and those of Lee et al. (2015). We do observe a roughly uniform offset of ≈ 0.5 dex with Tasca et al. (2014) which may be the result of the different technique used to measure the turnover mass.

3.3.2 Parameterization

In Figure 3.7 we parameterize the SFR$-M_*$ relation as a function of redshift. For this we adopt the same parameterization as Lee et al. (2015):

$$\log(\Psi) = \mathrm{s}_0 - \log\left[1 + \left(\frac{M_*}{\mathrm{M}_0}\right)^{-\gamma}\right] \tag{3.2}$$

where s_0 and M_0 are in units of $\log(M_\odot/\mathrm{yr})$ and $M_\odot$ respectively. This function behaves as a power-law of slope γ at low masses which asymptotically approaches a peak value s_0 above a transitional stellar mass M_0. Originally this parameterization was defined for star-forming galaxies, though we find it works similarly well for all galaxies (star-forming and quiescent) at the redshifts and stellar masses considered for this study. The righthand panels of Figure 3.7 show the best-fit parameters vs. redshift. We consider two cases for fitting: "free γ" and "fixed γ". In the "free γ" case, we allow all three parameters to vary independently for each redshift bin. Noticing that γ does not show strong evidence for evolution, we perform the "fixed γ" case by refitting with γ fixed to its mean value from the "free γ" fits. We then parameterize the evolution of s_0 and M_0 with second-order polynomials.

All Galaxies :

$$\begin{aligned} \mathrm{s}_0 &= 0.19 + 1.16z - 0.14z^2 \\ \log(\mathrm{M}_0) &= 9.24 + 0.75z - 0.09z^2 \\ \gamma &= 1.12 \end{aligned} \tag{3.3}$$

Evolution in the transition mass is a recent discovery, first reported quantitatively

by Lee et al. (2015) from a study of the COSMOS 2 deg^2 field. Results from the VUDS spectroscopic survey also suggest this evolution (Tasca et al. 2014). However, because we include all galaxies in the analysis presented here the observed evolution of M_0 may be a consequence of the increasing population of massive quenched galaxies at low-z. Therefore, we repeat this analysis for a sample of actively star-forming galaxies selected based on rest-frame (U−V) and (V−J) colors (see section 3.2.4). Evolution in M_0 is still apparent; results are shown in Figure 3.8. In Figure 3.9 we compare our measured values of the turnover mass to those of Lee et al. (2015) and Tasca et al. (2014).

$$\begin{aligned} \textbf{Star} - \textbf{Forming}: \\ s_0 &= 0.46 + 1.22z - 0.18z^2 \\ \log(M_0) &= 9.47 + 0.87z - 0.13z^2 \\ \gamma &= 1.09 \end{aligned} \tag{3.4}$$

We remind the reader that these parameterizations may not extrapolate well outside of the redshift and/or stellar mass ranges used here. Furthermore, mass-incompleteness may be affecting these fits, specifically at higher redshifts. Nevertheless, our low-mass slope of $\gamma \sim 1$ is consistent with the relative constancy of the low-mass slope $\alpha \sim -1.5$ of the SMF (Tomczak et al. 2014); if γ deviated significantly from unity then α would be expected to evolve strongly with redshift (Peng et al. 2010, Weinmann et al. 2012, Leja et al. 2015).

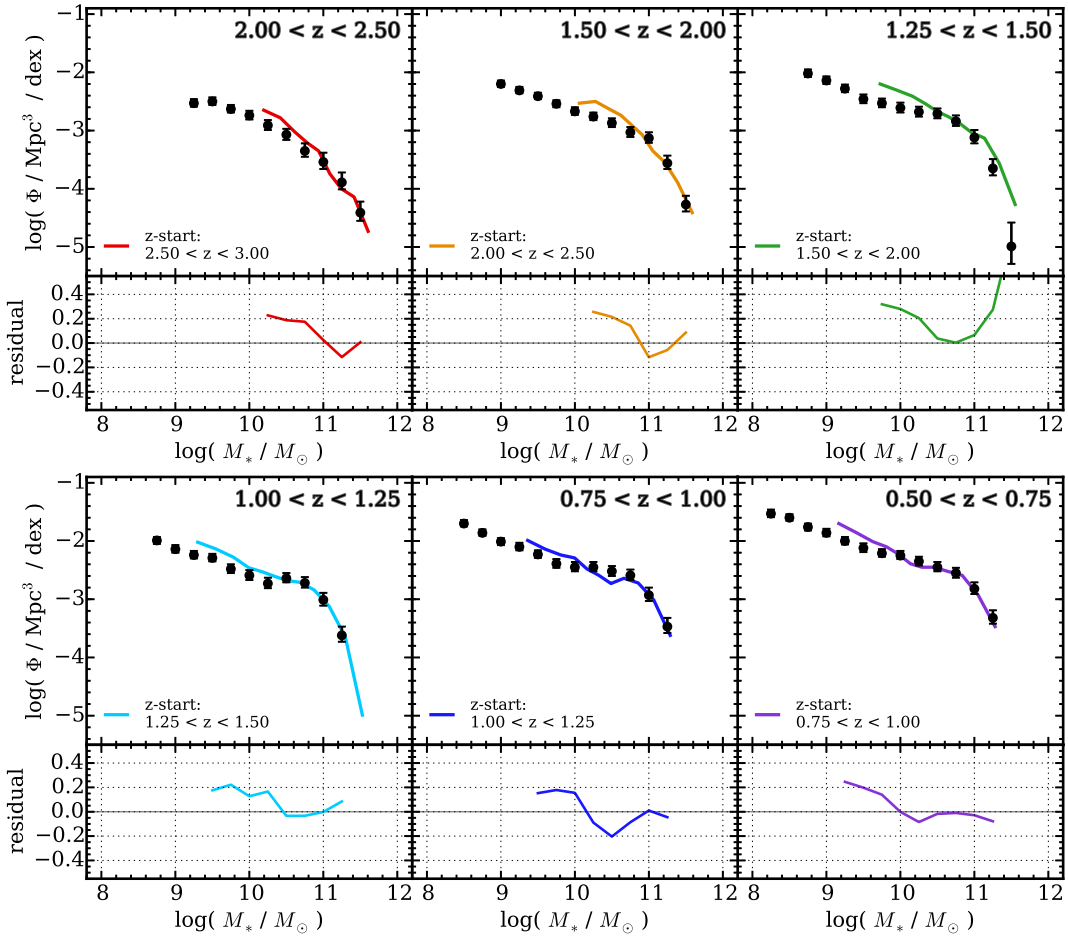

Figure 3.10: Inferring the Growth of the Galaxy Stellar Mass Function. Implied growth of the galaxy stellar mass function due to star-formation. Each panel shows the observed mass-complete SMF from Tomczak et al. (2014) at the redshifts indicated in the upper-right corner. Curves in each panel represent the SMF from the preceding redshift bin evolved evolved forward in time based on our parameterized SFR$-M_*$ relation. Redshifts of the original SMFs (i.e. "starting" redshifts) are indicated in the legend. Residuals between the evolved and observed SMFs for each redshift bin are shown in the lower panes. We observe that the numbers of galaxies at $M_* < 10^{10.5}\ M_\odot$ are consistently overproduced at each redshift by $\approx 0.2 - 0.3$ dex. It is important to note that galaxy merging is not accounted for in the inferred SMFs, thus, at least part of this offset must be caused by this effect.

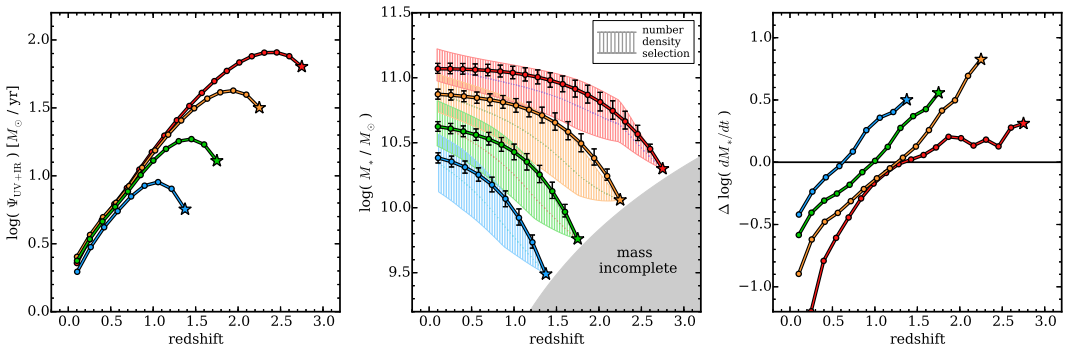

Figure 3.11: Empirical Star-Formation Histories.
Differential SFHs (**left**) and mass-growth profiles (**middle**) extracted from the evolution of the SFR$-M_*$ relation of all galaxies. To extend these measurements to $z \approx 0.1$ we use the SFR$-M_*$ relation of Salim et al. (2007). Star symbols indicate four arbitrary sets of initial conditions consistent with Equation 3.3 which are then propagated forward in time. Mass loss due to stellar evolution is accounted for according to Equation 16 of Moster et al. (2013). Hatched regions in the **middle** panel show the inferred growth profiles generated by mapping the predicted number density evolution (Behroozi et al. 2013) to the galaxy SMF as a function of redshift. Although there is broad agreement between these two techniques, we note that the integrated mass-growth curves are more accelerated, growing more rapidly at early times and slowing to lesser rates at later times. This is shown clearly in the **right** panel which plots the difference between the time derivatives of these two approaches. We note, however, that this is only a comparison of the median evolution and ignores the $\pm 1\sigma$ scatter.

3.4 Inferring Stellar Mass Growth

3.4.1 Growth of the Stellar Mass Function

The growth of galaxies as predicted from the SFR$-M_*$ relation can be compared directly to the evolution of the stellar mass function. Leja et al. (2015) performed such an analysis using stellar mass functions from Tomczak et al. (2014) and SFR$-M_*$ relations from Whitaker et al. (2012) finding that the inferred growth from star-formation greatly over-predicts the observed number densities of galaxies, even on short cosmic timescales ($<$ 1 Gyr). Those authors suggest that the SFR$-M_*$ relation must have a steeper slope ($\alpha > 0.9$) at masses below $10^{10.5}$ $M_\odot$ at $z < 2.5$, which is consistent with measurements from this work and recent literature (Whitaker et al. 2014, Lee et al. 2015, Schreiber et al. 2015).

Thus, we perform the same comparison using our updated SFR$-M_*$ relation. At each stellar mass for a given SMF at a given redshift, SFRs are calculated from the parameterized SFR$-M_*$ relation for all galaxies (Equations 3.2 and 3.3). In times steps of 80 Myr each mass bin is shifted by the amount of star formation added to that bin. SFRs are recalculated at each new time step. Mass loss due to stellar evolution is accounted for according to Equation 16 of Moster et al. (2013). Using this technique, we evolve the observed SMF in each redshift bin forward and compare it to the observed SMF in the next redshift bin; results are shown in Figure 3.10.

In general, we typically find reasonable agreement at intermediate stellar masses ($10^{10.5} < M_*/M_\odot < 10^{11}$). At lower masses, however, we find a consistent systematic offset in number density rising to $\approx 0.2 - 0.3$ dex. It is important to note that this method *does not* incorporate the effect of galaxy-galaxy mergers whereas the observed evolution galaxy SMF necessarily does. Therefore, the disparity between these two curves inherently includes a signature of merging; in fact, Drory & Alverez (2008) use

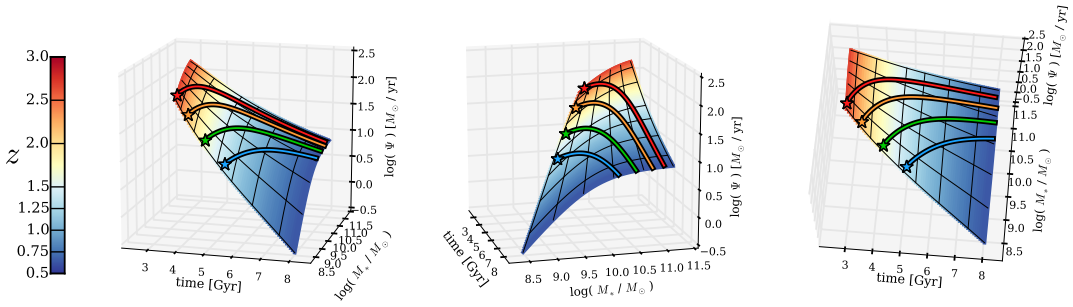

Figure 3.12: Modeling the SFR$-M_*-z$ Manifold.
A three dimensional representation for the redshift evolution of the SFR$-M_*$ sequence of all galaxies. Colored curves show the differential SFHs from Figure 3.11.

this difference to constrain galaxy growth rates due to merging. Mergers may help to alleviate the discrepancy we observe if these low-mass galaxies are merging with more massive galaxies, thereby reducing their number density. However this would require between $25-65\%$ of these galaxies to merge with a more massive galaxy per Gyr, which substantially exceeds current estimates of galaxy merger rates (e.g. Lotz et al. 2011, Williams et al. 2011, Leja et al. 2015). We therefore conclude that the SFRs are overestimated and/or the growth of the Tomczak et al. (2014) SMF is too slow.

3.4.2 Star-Formation Histories

The evolution of the SFR$-M_*$ relation can be used to infer typical star-formation histories and stellar mass-growth histories for individual galaxies. However, as seen in the previous subsection, there is tension between the growth of the galaxy population as inferred from the SFR$-M_*$ relation when comparing to the observed stellar mass function. Here we explore two different approaches two different approaches for empirically deriving galactic mass-growth histories: (1) integrating differential star-formation histories extracted from the SFR$-M_*$ relation and (2) identifying de-

scendents of high-z galaxies based on number density selected (NDS) samples (Figure 3.11). For the former, we start with the four sets of initial conditions (z_0, M_0, Ψ_0) indicated by the star symbols, where Ψ_0 is determined by our SFR parameterizations. Stellar mass is then incrementally added assuming constant star-formation over small time intervals of $\approx$ 80 Myr. At the end of each time step Ψ adjusted according to the SFR$-M_*$ parameterization $\Psi(z, M_*)$. At lower redshifts we interpolate between our Equation 3.2 and Equation 13 of Salim et al. (2007). Mass loss due to stellar evolution is accounted for according to Equation 16 of Moster et al. (2013).

In order to get a rough estimate of the scatter in these SFHs we run 1000 Monte Carlo simulations, resampling Ψ from a log-normal PDF with a mean value given by $\Psi(z, M_*)$ and $\pm$0.3 dex scatter. The approximate range of mass-growth for each galaxy sample is calculated from the 16^{th} and 84^{th} percentiles of the distribution. In Figure 3.12 we show a three dimensional representation of the SFR$-M_*$ relation's evolution throughout redshift with the same growth histories as in the preceding figure.

A number of studies have used this technique to estimate galaxy growth histories (e.g. Renzini et al. 2009, Peng et al. 2010, Leitner 2012). An important point that should be kept in mind is that in this section we use the SFR$-M_*$ relation for all galaxies $-$ not just actively star-forming ones $-$ as is appropriate for a comparison to NDS samples. Some other studies investigate the growth histories of galaxies that remain star-forming without ever quenching (Renzini et al. 2009, Leitner 2012).

Shaded regions in the middle panel of Figure 3.11 show the mass-growth profiles predicted from the NDS approach. Using the same initial conditions shown by the star symbols, we calculate the corresponding cumulative co-moving number density from the stellar mass functions of Tomczak et al. (2014) as parameterized by Leja et al. (2015). Note, this parameterization is limited to $z \leq 2.25$, beyond which we

interpolate between it and the best-fit Schechter function to the SMF at $2.5 < z < 3$. Next, using the code presented by Behroozi et al. (2013) we generate predictions for the subsequent number density evolution of these galaxies. This code uses results from a dark matter simulation to estimate how the cumulative number density of a given sample of galaxies changes with time due to mergers and variations in mass accretion histories. It can also be used to estimate scatter in growth histories. At each redshift we map the number density to the corresponding stellar mass using the SMFs. The width of the shaded regions indicate the 1σ scatter in this number density evolution.

Overall we find broad agreement between these two approaches. However there is a common systematic difference wherein the differential SFHs produce a steeper mass-growth rate for the same progenitor galaxy at early time which provides us with a different view of the discrepancy shown in Figure 3.10. This disparity is illustrated in the rightmost panel of Figure 3.11 which shows the difference in the mass-growth rates of both techniques from the middle panel. The differential SFHs build stellar mass more quickly at early times, but then slow down and are eventually overtaken by the NDS growth rates. We tested a wide range of initial conditions spanning $0.8 \leq z_0 \leq 2.75$ and $8.8 \leq \log(M_0/M_\odot) \leq 10.5$, always finding this systematic trend. Papovich et al. (2014) find similar results in their analysis of the progenitors of galaxies with present-day masses of the Milky Way and M31 galaxies. Finally, we have repeated this comparison using the SFR$-M_*$ parameterizations provided by Whitaker et al. (2014) and Schreiber et al. (2015) and in both cases we find similar disagreements.

3.5 Discussion

In this paper we present new measurements of the evolution of the SFR$-M_*$ relation utilizing deep imaging and high-quality photometric redshifts from the FourStar Galaxy Evolution Survey (ZFOURGE) in combination with ancillary far-IR imaging at 24μm, 100μm, and 160μm from *Spitzer* and *Herschel*. Bolometric IR luminosities (L_{IR}), used for calculating obscured star-formation rates, are obtained by scaling the IR spectral template introduced by Wuyts et al. (2008) to the $24-160\mu$m photometry. This luminosity-independent approach has been shown to be more appropriate for estimating infrared luminosities than luminosity-dependent approaches (Muzzin et al. 2010, Wuyts et al. 2011).

To test this with the present dataset we compare the derivation of L_{IR} from fitting the W08 template to the MIPS 24μm photometry only vs. fitting to the PACS 100+160μm photometry only. From a sample of 1050 individually detected galaxies we find consistent estimates of L_{IR} between both cases with no dominant systematic trends and a typical scatter of ≈ 0.2 dex over a wide range of redshifts and stellar masses ($0.2 < z < 3$ and $10^{9.5} < M_*/M_\odot < 10^{11}$). Interestingly, however, when we perform this comparison on stacked $24-160\mu$m photometry we do find a systematic trend wherein the MIPS-derived L_{IR} tends to exceed the PACS-derived L_{IR} for stacks of higher mass galaxies. Although this effect is not large (< 0.2 dex), it nevertheless suggests that the mean IR SED of the faint, non-detected galaxies must be different than the the mean IR SED of their brighter, detected counterparts.

Utilizing star-formation rates derived from the UV+IR stacking analysis we examine evolution of the SFR$-M_*$ relation at $0.5 < z < 4$. We perform this analysis for all galaxies as well as a sample of actively star-forming galaxies as selected by their rest-frame (U$-$V) and (V$-$J) colors. In agreement with recent results, we find

that SFRs are roughly proportional to stellar mass at low masses ($< 10^{10.2}$ $M_{\odot}$), but that this trend flattens at higher masses (see also Whitaker et al. 2014, Lee et al. 2015, Schreiber et al. 2015). Furthermore, although the evolution of the SFR$-M_*$ relation is still predominantly in normalization, the slope at high masses ($M_* > 10^{10.2}$ $M_{\odot}$) is also changing. Similar to Lee et al. (2015) and Tasca et al. (2014) we find that the transition mass at which this flattening occurs evolves with redshift; this is true whether or not quenched galaxies are included. Full parameterizations of the SFR$-M_*$ relation with respect to redshift, $\Psi(z, M_*)$, for both all and star-forming galaxies are presented in section 3.3.2.

Recent cosmological simulations from the Illustris collaboration (Nelson et al. 2015) and the Munich galaxy formation model (Henriques et al. 2014) also show a flattening at the high-mass end, however, are not able to reproduce its evolution accurately. Furthermore, these simulated SFR$-M_*$ relations are systematically lower than the observations by an offset ranging between $0.17 - 0.45$ dex at $0.5 < z < 4$ being largest at $z \sim 1$. Nevertheless, both simulations reproduce the slope at $< 10^{10}$ $M_{\odot}$, both in its value and its relative constancy with redshift.

Comparing measurements of the SFR$-M_*$ relation to recent literature at $0.5 < z < 4$ we find a typical scatter at fixed stellar mass of ≈ 0.2 dex (see section 3.3.1). This is consistent with the inter-publication scatter found by Speagle et al. (2014) which draws on a larger sample of published SFR$-M_*$ relations. An interesting outcome from our comparison, however, is the presence of a weak systematic trend at high masses, most apparent in the full sample at $z \sim 2$. Investigating this further we find that this discrepancy is likely caused by the inclusion of the *Herschel* PACS imaging for measuring L_{IR}. We perform a more extensive comparison of our SFR$-M_*$ relations to those of 3D-HST (Whitaker et al. 2014) which rely on much of the same public imaging, have had photometry performed using similar methods, and use the

same conversions to calculate UV+IR star-formation rates, with the main difference being that Whitaker et al. (2014) estimate L_{IR} from MIPS 24μm imaging only. When we remeasure our SFR$-M_*$ relations, excluding the *Herschel* PACS imaging, and compare to Whitaker et al. (2014) we find the systematic trend with stellar mass disappears.

However, it is important to note that this contrasts what was found for galaxies that are individually detected in the far-IR images which show no strong evidence of a systematic trend between L_{IR} and stellar mass (Figure 3.2). This suggests that faint, non-detected galaxies have SEDs that are not consistent with their more luminous counterparts (Muzzin et al. 2010, Wuyts et al. 2011). Nevertheless, this discrepancy is small being on the order of the observed inter-publication scatter.

We use two techniques to extract empirical star-formation and mass-growth histories from the observations. First, we integrate along the evolving SFR$-M_*$ sequence to estimate how galaxies should grow due to star-formation. Second, we estimate mass-growth histories from measurements of the galaxy stellar mass function using an evolving number density selection (NDS) criterion (Behroozi et al. 2013). It is worthwhile to note that both techniques used here provide *typical* SFHs along with a rough indication of the scatter, but that individual galaxies may follow very different evolutionary pathways (Kelson 2014, Abramson et al. 2015). In general we observe a systematic difference between these two approaches wherein the differential SFHs suggest more rapid mass evolution at higher redshifts than is inferred from the NDS samples. This disagreement in mass-growth rates is as high as $\sim$0.5 dex. At lower redshifts the NDS predict more rapid evolution; this can be naturally explained by galaxy mergers, and the size of the difference can be taken as a measure of the growth rate due to mergers (e.g. Drory & Alverez 2008, Moustakas et al. 2013).

The disagreement at $z < 1$ suggests that either our SFRs are overestimated, that

the rate of mass-growth inferred from the stellar mass function is underestimated, or both. Errors in star-formation rate measurements may arise from low-level AGN activity, an incorrect conversion of flux to bolometric UV/IR luminosities, the assumed IMF, and variations in star-forming duty cycles as probed by UV and IR indicators. Stellar masses were estimated by fitting models to the observed spectral energy distributions (SEDs) of individual galaxies. Various assumptions that go into the SED-fitting process that are possible sources for systematic errors include smooth exponentially declining SFHs, a single dust screen, a constant IMF, solar metallicity, and assuming that emission lines do not contribute significantly to the observed photometry (for detailed discussions see Conroy 2013, Courteau et al. 2014).

The measurements on which this study is based were performed using high-quality data and standard methods. Moreover, the use of the same ZFOURGE sample for measuring both the SMF and the SFR$-M_*$ relations helps provide internal consistency for this work. Although the broad qualitative agreement that we find in mass-growth histories is encouraging for current studies of galaxy evolution, the disagreements may highlight the need to move beyond the simplistic assumptions that underly current data analysis methods.

4. A CENSUS OF MID-INFRARED SELECTED ACTIVE GALACTIC NUCLEI IN MASSIVE GALAXY CLUSTERS AT $z < 1.3$*

4.1 Background Information

One fundamental observation is that dense environments at low redshifts are dominated by passive, early-type galaxies that define a narrow red sequence in an optical color-magnitude diagram (Sandage & Visvanathan 1978, Bower et al. 1992, Hogg et al. 2004), and studies of the cluster color-magnitude relation (CMR) show that the luminous red sequence members in galaxy clusters have not evolved significantly since $z \sim 0.8$ (Rudnick et al. 2009). In contrast, the less massive cluster members continue to migrate to the red sequence as studies at $z > 0.6$ show there are fewer faint red galaxies in clusters compared the field and to lower redshift clusters (De Lucia et al. 2007, Stott et al. 2007, Rudnick et al. 2009). Recent observations at $z > 1.4$ have now even found massive, star-forming galaxies in clusters (Tran et al. 2010, Hilton et al. 2010).

The question then remains as to what halts star formation in cluster galaxies? Possible environmental processes include ram-pressure stripping (Gunn & Gott 1972), tidal effects from the cluster potential (Farouki & Shapiro 1981), and galaxy-galaxy interactions (Richstone 1976), but none are completely effective at reproducing the star formation histories and scaling relations observed in galaxy clusters. Semi-analytic models that include AGN are able to reproduce observed mass/luminosity functions (Croton et al. 2006, Bower et al. 2006, Lagos et al. 2008). AGN can also affect the intra-cluster medium (ICM) where models find that including AGN produces

* Reprinted with permission from "A Census of Mid-infrared-selected Active Galactic Nuclei in Massive Galaxy Clusters at $0 < z < 1.3$" by Tomczak et al., 2011. The AstroPhysical Journal, 738, 65-77, Copyright 2011 by Adam Tomczak.

much better agreement with observations of X-ray properties of the ICM (Bower et al. 2008, Puchwein et al. 2008, McCarthy et al. 2010).

AGN feedback seems to be an ideal solution to resolve many outstanding discrepancies between models and observations (Gabor et al. 2010, Fontanot et al. 2010, Teyssier et al. 2011); however, there is not yet clear observational evidence that AGN contribute significantly to the quenching of star formation in cluster galaxies, making clusters into resting homes of passive galaxies. Several groups using primarily X-ray observations find the fractional density of X-ray selected active galactic nuclei (X-ray AGN) in cluster environments increases with redshift (Eastman et al. 2007, Martini et al. 2009). Similarly, using X-ray, infrared and radio selection at $z < 1.5$ Galametz et al. (2009) find that the AGN surface-density (N/arcmin^2) is greater for clusters than in the field and that the AGN volume-density (N/Mpc^3) for clusters increases with redshift. In contrast, a study of CL $0023 + 04$, a large scale system of four galaxy groups merging at $z \sim 0.83$, does not find an excess of X-ray sources relative to the field (Kocevski et al. 2009). In general, studies are hampered by the small number of X-ray AGN and the need to isolate a large sample of cluster galaxies at higher redshifts. Another important issue is that different diagnostics select different populations of AGN (Hart et al. 2009, Hickox et al. 2009, Griffith & Stern 2010) and so no single approach will be complete. Thus while CL $0023 + 04$ does not have an excess of X-ray sources, Lubin et al. (2009) do find a population of passive (no detectable Hα) members with [OII] emission that may be due to AGN.

4.2 Data and Reductions

4.2.1 Spitzer IRAC

Mid-infrared observations were taken with the IRAC instrument (Fazio et al. 2004) on board the *Spitzer Space Telescope* (Werner et al. 2004) and are publicly

available on the Spitzer archive. IRAC observes in four mid-infrared channels centered at 3.6, 4.5, 5.8 and 8.0 μm. These channels have transmission functions such that all emission between 3.1 and 9.4 μm will be detected. Furthermore, the edges of the channels are steep, so that as an emission feature becomes redshifted out of one bandpass it will promptly shift into the adjacent one. This ensures that spectral features (such as PAH emission from dusty star formation) can be traced fairly easily over a wide range in redshift.

For most of the cluster fields, multiple IRAC observations were conducted at different times. In the interest of increasing depth we make use of all available data. This also frequently served to increase the area of coverage allowing more cluster galaxies to be detected.

4.2.1.1 Mosaicking

Each observational campaign is composed of a series of dithered images referred to as Basic Calibrated Data (BCD). The depth of a final mosaic depends on the combination of exposure time and number of frames per sky position. BCDs are single-frame images that have been reduced and flux-calibrated on a basic level by the *Spitzer* pipeline. We performed further processing and mosaicking using MOPEX (18.3 rev 1, Makovoz et al. 2006), a set of reduction and analysis tools designed by the *Spitzer Science Center*. The software includes modules that flag and remove spurious detections that are not accounted for in the automatic pipeline reduction. Prior to mosaicking, images were inspected for artifacts such as "muxbleed" and column pull-up/down and were mitigated using the *cosmetic* module from MOPEX.

Overlapping is another necessary step in the image reduction process available as a package in MOPEX. Within a set of dithered frames, the individual backgrounds may vary to the point that the background of a final mosaic shows a checkered

Table 4.1: Cluster Properties.

Cluster	Coordinates[a]	z-range[b]	N_z[c]	$N_{\rm IRAC}$[d]	Log(L_X)[e]	Status[f]
Coma	12 59 35.7 +27 57 34	(0.013 - 0.033)	348	262	43.0	Relaxed
Abell 1689	13 11 29.5 −01 20 17	(0.17 - 0.22)	81	73	43.3	Relaxed
MS 1358+62	13 59 50.4 +62 31 03	(0.315 - 0.342)	171	133	43.0	Unrelaxed
CL 0024+17	00 26 35.7 +17 09 43	(0.373 - 0.402)	205	75	42.5	Unrelaxed
MS 0451−03	04 54 10.9 −03 01 07	(0.52 - 0.56)	242	90	43.3	Relaxed
MS 2053−04	20 56 21.3 −04 37 51	(0.57 - 0.60)	132	87	42.8	Unrelaxed
MS 1054−03	10 57 00.0 −03 37 36	(0.80 - 0.86)	153	120	43.2	Unrelaxed
RX J0152−13	01 52 43.9 −13 57 19	(0.81 - 0.87)	147	80	43.3	Unrelaxed
RDCS J1252−29	12 52 54.4 −29 27 18	(1.22 - 1.25)	38	29	42.8	Unrelaxed

Notes. All clusters in this sample have $M_{\rm vir} > 5 \times 10^{14} M_{\odot}$.

[a] Right ascension and Declination are for J2000.

[b] Range of redshifts for spectroscopically confirmed members from Saintonge et al. (2008) and Demarco et al. (2007)

[c] Total number of spectroscopically confirmed cluster members. Redshifts are from Rines et al. (2003, Coma), Duc et al. (2002, Abell 1689), Fisher et al. (1998, MS 1358), Moran et al. (2005, CL 0024), Moran et al. (2007a, MS 0451), Tran et al. (2005a, MS 2053), Tran et al. (2007, MS 1054), Demarco et al. (2005, RX J0152) and Demarco et al. (2007, RDCS J1252) respectively.

[d] Number of cluster galaxies with detections in at least three IRAC channels.

[e] Bolometric ICM X-ray luminosities (ergs s^{-1}) from Holden et al. (2007, Coma, MS 1358, MS 2053, MS 1054, RX J0152), Bardeau et al. (2007, A1689), Donahue et al. (1999, MS 0451), Zhang et al. (2005, CL 0024) and Rosati et al. (2004, RDCS J1252).

[f] Dynamical state of each cluster determined from redshift distributions and X-ray & weak lensing profiles. Unrelaxed systems are those that show signs of a cluster scale merger.

Table 4.2: IRAC Photometry.

Cluster	Aperture[a]	3.6μm[b]	4.5μm[b]	5.8μm[b]	8.0μm[b]
Coma	15”	20.3	20.1	18.8	18.1
1689	7.7”	19.6	19.9	19.7	19.0
1358	5.3”	20.8	21.1	20.4	20.2
0024	4.8”	20.6	20.9	20.2	20.0
0451	4.0”	20.9	21.0	20.3	20.0
2053	3.8”	20.8	20.9	20.3	20.1
1054	3.3”	21.1	21.2	20.7	20.5
0152	3.3”	21.1	21.4	20.1	20.3
1252	3.0”	21.0	21.3	20.6	20.6

[a] Fixed circular aperture corresponding to physical diameter of $\sim$ 25 kpc at cluster redshift except for Coma where the aperture corresponds to 6 kpc; see §3.2 for details.
[b] AB magnitude corresponding to 80% completeness limit; see §4.2.1.2 for details.

pattern/gradient. Performing overlap matches the backgrounds of all input frames and so removes this effect. After overlapping, BCDs are then stacked. Weight maps were also obtained for each mosaic as coverage varied between campaigns.

4.2.1.2 Photometry and Completeness

Fixed-aperture photometry was carried out on each mosaic using SExtractor 2.5.0 (Bertin & Arnouts 1996). In order to analyze cluster galaxies at varying z equally, apertures were chosen at constant proper sizes according to cluster redshifts (except for Coma, see §4.3.2.1). Ideally, apertures should be small so as to isolate the central engine and reduce possible contamination from, e.g. extended star forming regions in the host galaxy. However, the IRAC point spread functions (PSFs) are $\sim$1.66, 1.72, 1.88 and 1.98” in diameter for channels 1$-$4 respectively, and fluxes determined from apertures comparable to the IRAC pixel size ($\sim$ 1.22$''$ px^{-1}) are subject to sampling errors. These caveats constrain the minimum size of a reasonable aperture. Ultimately, we choose a radius of $\sim$12.6 kpc, which corresponds to an aperture

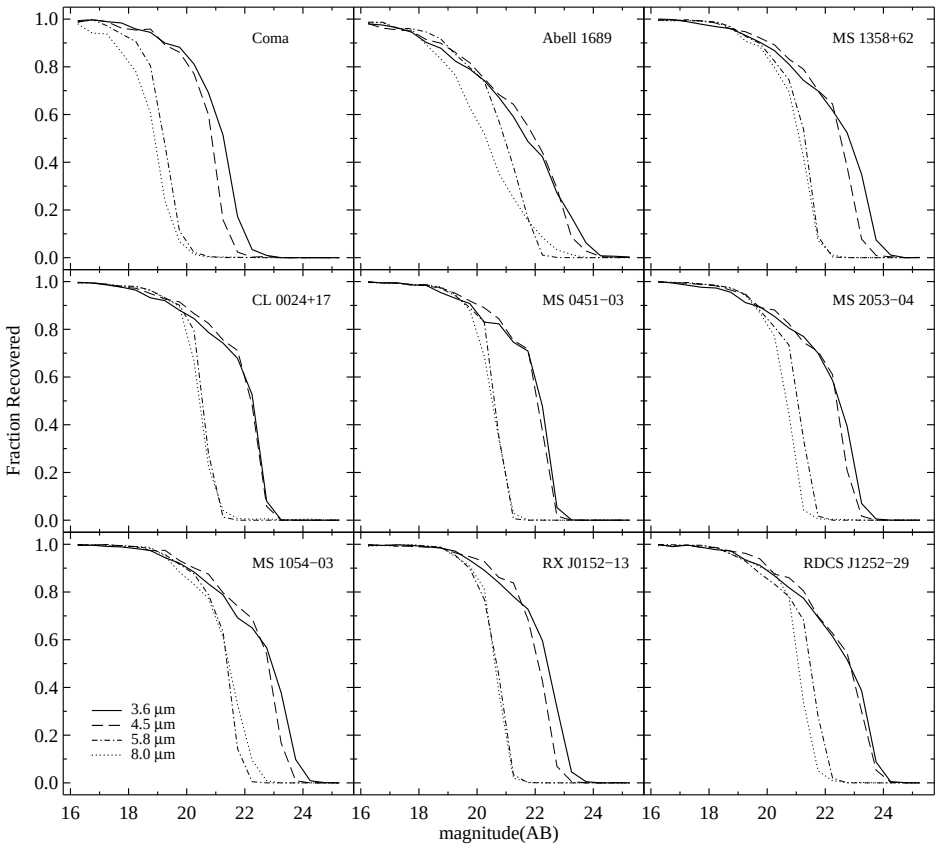

Figure 4.1: Infrared Photometric Completness.
Completeness functions for each cluster field showing the fraction of recovered sources versus their input magnitude. For each cluster, 1000 generated galaxies were randomly distributed in 0.5 magnitude bins in a 1.5×1.5 Mpc^2 box centered near the cluster core. Sources that were extracted with magnitudes brighter than their input value were rejected as blendings. The 3.6 and 4.5μm channels exhibit a more gradual decline in completeness due to source confusion from greater crowding (see Barmby et al. 2008) which increases the likelihood of blendings.

diameter of 3" for the most distant cluster (see Table 4.2 for all aperture sizes). We note that a 12.6 kpc aperture is much larger than would be "ideal" for this type of a study; however, we feel that accepting this limitation is preferred over varying the physical sizes of apertures, which would likely introduce a selection bias.

Aperture corrections were determined from IRAC calibration stars (Reach et al. 2005) as discussed in Ashby et al. (2009)), except for Coma where theoretical aperture corrections for extended sources were used. Although some galaxies in our other low-z clusters are resolved, the discrepancy between extended- and point-source aperture corrections is not enough to affect our results. Further discussion regarding these corrections can be found in the IRAC Instrument Handbook. IRAC fluxes are calibrated based on $24''$ (diameter) apertures and an appropriate correction needs to be applied to photometry using apertures of different sizes. Aperture corrections are defined as the difference between the magnitude of a point-sources from a $24''$ aperture and the magnitude from the aperture of interest. We determined aperture corrections from five standard stars (HD-165459, 1812095, KF06T1, NPM1p66.0578, NPM1p67.0536) using the average as the final value. Because Galactic extinction is negligible at these wavelengths (< 0.01 mag) the corrections are less than the measurement uncertainties, we do not correct the IRAC magnitudes; however, we do correct for Galactic extinction in the optical filters.

Completeness was measured using the *gallist* and *mkobjects* modules in IRAF*. For each mosaic, 1000 artificial galaxies in half-magnitude bins between $16 \leq m \leq 25$ were distributed randomly. Source extraction was then carried out for these fake sources with identical parameters as used for the real sources. Fake sources that were extracted with magnitudes brighter than their input value were discarded as blendings. In order to get a sense of the completeness within each cluster, sources were added in 1.5×1.5 Mpc boxes centered on the core of each cluster. Measurements

of completeness are shown in Figure 4.1 and Table 4.2.

In performing source matching, we start with the coordinates of a galaxy from optical images. We then search for the nearest source in each IRAC catalog within a 2" radius, i.e. slightly larger than the IRAC PSF. In a few cases, e.g. in the cores of the high redshift clusters, there is some blending of IRAC sources. We deblend and separate sources using the SExtractor parameters DEBLEND NTHRESH=64 (for all channels) and DEBLEND MINCONT=0 and 0.005 (for channels 1,2 and 3,4 respectively). Visual inspection confirms that these parameters are effective at deblending sources with only 2 pairs/groups of galaxies still blended in the $z > 0.8$ clusters; only one of these has an IR-AGN signature (see §3.2.8).

4.2.2 Optical Photometry and Spectroscopy

Catalogs of optical and near infrared photometry as well as optical spectroscopy were obtained from multiple sources. Observed photometry was converted to rest-frame values using KCorrect v0.2.1, an extension of *kcorrect* (Blanton & Roweis 2007) developed for Python by Taro Sato. Extensive spectroscopic catalogs were used to confirm membership for each cluster. General properties of each galaxy cluster are shown in Table 4.1. Here we summarize additional details of each dataset.

- *Coma*: Photometry was taken from Mobasher et al. (2001) which consists of measurements in the B and R bands. Completeness was assessed to be 22.5 mag and 21 mag in B and R respectively. Spectroscopy for the Coma cluster was taken as part of the Cluster and Infall Nearby Survey (CAIRNS: Rines et al. 2003). Galaxies targeted in this survey were selected from digitized images of the POSS I 103aE (red) plates which are complete down to E=15-16.

∗ IRAF is distributed by the National Optical Astronomy Observatory (NOAO), which is operated by the Association of Universities for Research in Astronomy, Inc., under cooperative agreement with the National Science Foundation.

- *Abell 1689*: Data for Abell 1689 (Duc et al. 2002) were taken as follow-up to the photometric observations conducted by Dye et al. (2001). Photometry was acquired for the BVR bands and is complete to 23.0, 22.7 and 22.7 mag respectively. Spectra were obtained for most($\sim$75%) of the photometric cluster members at $R \leq 17.75$ mag which drops to $\sim$40% at $R \leq 19.5$ mag.

- *MS 1358+62*: Observations of MS 1358 taken from Fisher et al. (1998) including photometry in the V and R bands and spectroscopy. Spectroscopic completeness was determined to be >80% at $R \leq 21$ mag when compared to photometric observations which were complete to $R \sim 23.5$ mag.

- *CL 0024+17 and MS 0451-03*: Data for CL 0024 and MS 0451, including photometry from the HST WFPC2 instrument, are discussed in detail in Treu et al. (2003) and Moran et al. (2005, 2007a). Photometry was measured to be complete to $I \sim 25$ (Vega mags)† for CL 0024 and spectroscopic completeness was found to be $> 65\%$ at $I < 21.1$ and $I < 22.0$ mag for CL 0024 and MS 0451 respectively. Additional ground-based photometry was also obtained in the $BVRIJK_s$ bands reaching 3σ depths of 27.8, 26.9, 26.6, 25.9, 21.6 & 19.7 mag for CL 0024 and 28.1, 27.0, 27.3, 25.9, & 20.2 mag for MS 0451 (Moran et al. 2007a).

- *MS 2053-04 and MS 1054-03*: Spectroscopy for MS 2053 is detailed in Tran et al. (2005a) and completeness determinations were assessed according to sampling and success rates. The success rate is defined as the number of spectroscopic redshifts obtained divided by the number of spectroscopic targets. Spectroscopic completeness was determined to be $\sim$70% at $m_{814} < 22$ mag. Similar methods were applied for MS 1054 (Tran et al. 2007) which found

† Here the I-band refers to the F814W filter from the WFPC2 instrument

completeness to be >75% at $m_{814} \leq 21.2$ mag. Photometry for both MS 2053 and MS 1054 were acquired from the *HST*/WFPC2 F606W and F814W filters.

- *RX J0152-13 and RDCS J1252-29*: Photometry for RX J0152 (Blakeslee et al. 2006) was obtained from the ACS instrument onboard the *HST* in the F625W, F775W and F850LP bandpasses. Incompleteness for these observations begins to set in at ∼23.5, 22.5 and 22. Demarco et al. (2005) determined spectroscopic membership for RX J0152 confirming 102 cluster galaxies out of 262 targets. Observations of RDCS 1252 is outlined in Demarco et al. (2007). Photometry was taken in the $B, V, R, i_{775}, z_{850}, J, K_s$ filters reaching 5σ limiting magnitudes of 26.5 & 26 mag in the J & K_s filters respectively. The spectroscopic success rate for RDCS J1252 was found to show a rapid decline at $K_s = 21.5$ mag, dropping from 85% to 20%.

4.3 Results

4.3.1 IRAC Color Selection of AGN

Mid-IR emission from an AGN is widely accepted as thermal continuum from circumnuclear dust (Andreani et al. 2003, Kuraszkiewicz et al. 2003). As radiation from the accretion disk bombards the surrounding dust, it is heated to temperatures in the range of $\sim 20 - 1000$ K (below dust sublimation at $T \sim 2000$ K, Sanders et al. 1989). IRAC colors alone can be an effective method for separating star forming galaxies from those hosting AGN at redshifts up to $z \sim 2$ (Lacy et al. 2004, Stern et al. 2005). It is worth noting that $> 50\%$ of a galaxy's mid-IR emission must originate from the nuclear component (Hickox et al. 2007, Hopkins et al. 2009, Atlee et al. 2011) in order to be selected by the criteria of Stern et al. (2005). Thus, due to various limitations in measuring IRAC fluxes in our sample, we are only able to select galaxies that are dominated by AGN emission in the mid-IR.

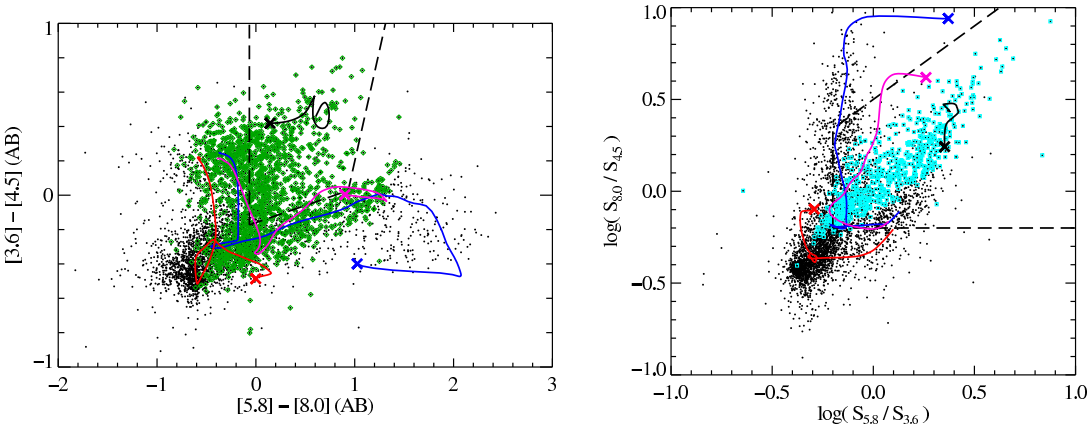

Figure 4.2: IR Color Selection of AGN.
Combined IRAC color-color plots as defined by Stern et al. (2005) and Lacy et al. (2004) derived from 3" apertures. Plotted are all detected sources in the IRAC mosaics for each cluster field. Curves in both panels are redshift-tracks for M82 (a local starbursting galaxy; blue), VCC 1003 (a local passively evolving galaxy; red), Mrk231 (Seyfert 1 AGN; black) and a Seyfert 2 template (pink); tracks begin at $z = 0$ marked with Xs and go to $z = 2$ (Devriendt et al. 1999, Polletta et al. 2007). The areas enclosed by the dashed lines are empirically defined regions designed to select galaxies dominated by emission from an AGN. Sources that fall in the wedge on the **left** are overlaid with cyan squares on the **right** whereas sources in the wedge on the **right** are overlaid with green diamonds on the **left**. Only ∼33% of Lacy IR-AGN are selected as Stern IR-AGN, whereas ∼89% of Stern IR-AGN are selected as Lacy IR-AGN. Furthermore, the Stern criteria determine an AGN fraction of 15%, whereas using the Lacy criteria it is 40%. We adopt the Stern IR selection for our analysis as it seems to suffer less contamination from non-AGN sources. See Barmby et al. (2006) and Donley et al. (2008) for a more in depth analysis of mid-IR color evolution in galaxies with and without AGN.

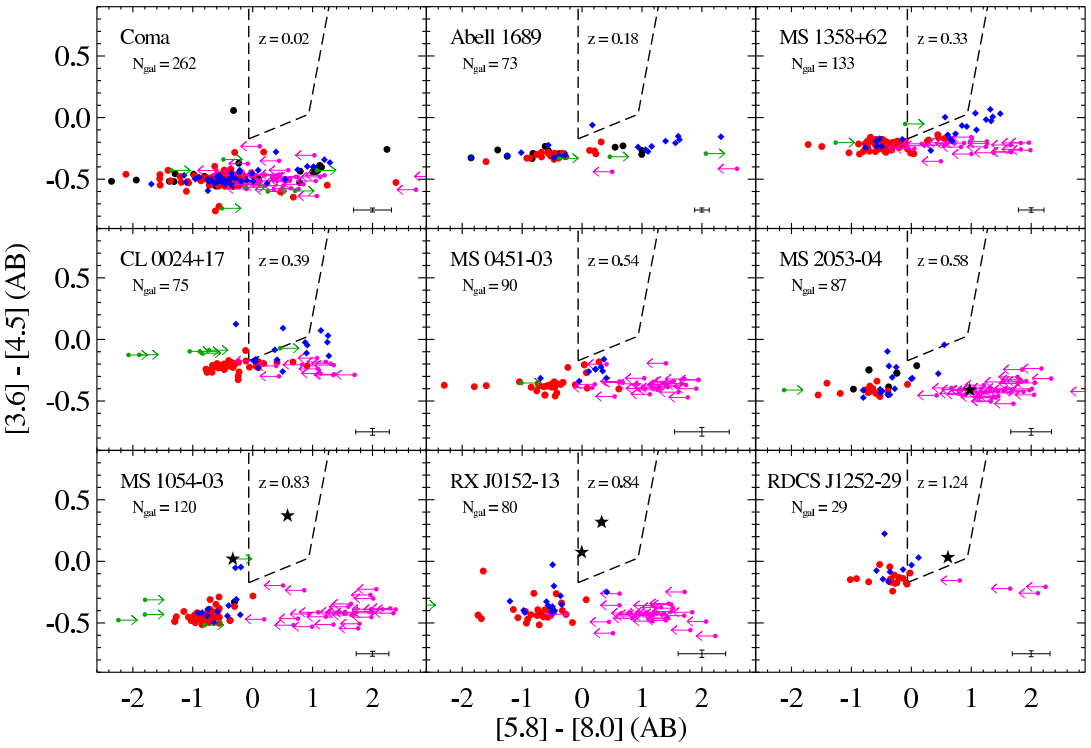

Figure 4.3: Identification of IR-AGN in the Cluster Sample.
IRAC color-color plots used to select active galactic nuclei (IR-AGN; Stern et al. 2005) for the galaxy clusters in our study. Cluster redshift and number of confirmed members are shown in each panel. Data points correspond to morphologically classified early-type members (red circles), late-types (blue diamonds) and unclassified/mergers (black circles). Upper limits are determined for galaxies lacking detections in a particular channel (green and pink arrows, see §4.3). X-ray sources are indicated as stars. Mean uncertainties are shown in the lower-right corner of each panel. Early-type galaxies with blue IRAC colors populate the lower-left region in each plot (the "passive cloud") whereas IR-AGN populate the area enclosed by the dashed lines. Our cluster IR-AGN are predominantly hosted by late-type galaxies.

The optical to mid-IR spectral energy distribution (SED) of AGN are typically well characterized by a rising power law with a few notable PAH features, thus causing these objects to appear increasingly red in the IRAC window (Polletta et al. 2007). Consequently, AGN tend to populate a separate region in mid-IR color space. Furthermore, studies have shown that various types of Seyferts have very similar mid-IR properties (Gandhi et al. 2009 and references therein). Radiation at these wavelengths is relatively insensitive to extinction and thus gives a reliable measure of reprocessed emission from the central engine. However, it is worth noting that highly obscured sources ($A_V > 30$) may be pushed outside the IRAC selection wedge (see Fig. 1 of Hickox et al. 2007).

Figure 4.2 shows the empirical color selection criteria from both Stern et al. (2005) and Lacy et al. (2004) for all IRAC sources detected in our nine cluster fields (including the cluster galaxies). Included in Figure 4.2 are color tracks of template galaxy SEDs from Devriendt et al. (1999): M82 (local starbursting galaxy; blue), VCC 1003 (local passively evolving galaxy; red), Mrk231 (Seyfert 1 AGN; black), and a Seyfert 2 template (pink). Tracks begin at $z = 0$ marked with Xs and go to $z = 2$ (Polletta et al. 2007). We refer the reader to Barmby et al. (2006) and Donley et al. (2008) for a more detailed discussion of the mid-IR color evolution for galaxies including limitations of mid-IR selection.

To compare the selection methods of Lacy et al. (2004) and Stern et al. (2005) we determine IR-AGN fractions for all galaxies (field and cluster) detected in all four bands of our IRAC imaging. We obtain fractions of 40% and 15% for the Lacy and Stern criteria respectively. In Figure 4.2, the green diamonds in the Stern plot correspond to sources that are selected as AGN using the Lacy criteria, whereas cyan squares in the Lacy plot correspond to sources that are selected as AGN using the Stern criteria. Approximately 89% of the Stern-selected AGN are Lacy-selected

AGN; however, the reverse shows that only ∼33% of all Lacy-selected AGN are also selected based on the Stern criteria. The higher IR-AGN fraction measured using the Lacy criteria is not surprising given that the track for M82 falls in the Lacy wedge. Because the Lacy criteria do not exclude starburst galaxies as effectively as the Stern criteria, we adopt the Stern criteria throughout the rest of this paper.

4.3.2 Individual Clusters

IRAC color plots for the nine massive galaxy clusters are shown in Figure 4.3. Only galaxies that have been spectroscopically confirmed as members with $\geq 3\sigma$ detections in at least 3 IRAC channels are shown. Data points indicate morphologically classified elliptical/S0 galaxies (red circles), late-type galaxies (blue diamonds), unclassified/merger (black circles), sources with no detection in channel 4 only (pink arrows) and no detection in channel 3 only (green arrows). For sources that lacked detections in a single bandpass, upper/lower limits were determined by assuming the 80% completeness magnitude for the respective bandpass (Table 4.2). Applying these limits mostly reveals a fainter population of passive galaxies. Considering that channels 1 & 2 (shorter wavelength) probe to fainter magnitudes than channels 3 & 4 (longer wavelength), galaxies in the "passive cloud" (with declining mid-IR SEDs) tend not to be detected at longer wavelengths while galaxies with IR-AGN (with increasing mid-IR spectra) are more likely to be detected in all four channels. This is why no potential candidate AGN are identified by our limit determinations. We use optically-determined coordinates for cluster galaxies to locate their IRAC counterparts. Using a matching radius of 2" (6" for Coma) we find the rate of detecting a false positive to be $< 1\%$.

4.3.2.1 Coma

The Coma cluster is one of the richest and most closely studied galaxy clusters and is known to be dominated by passively evolving systems with early-type morphologies (Michard & Andreon 2008). IRAC imaging for this cluster in all four channels covers roughly a 51.1'×62.5' region centered on NGC 4874, a field of view that includes 348 spectroscopically confirmed cluster galaxies from the CAIRNS (Rines et al. 2003). Determining photometry with *Spitzer* data for resolved galaxies is not as straightforward as for the mostly unresolved galaxies in the distant clusters (see the IRAC Instrument Handbook for details). We decide against using flexible-aperture photometry from SExtractor because of the differently sized apertures used for the same galaxy across the IRAC channels. Instead, we use a constant 15″ diameter aperture (6 kpc at Coma's mean redshift) and apply aperture corrections to the extended objects as detailed in the IRAC Instrument Handbook.

Not surprisingly, we find that an overwhelming majority of Coma galaxies occupy the "passive cloud" in IRAC color space and well below the AGN wedge. The dispersion in the [5.8]−[8.0] color is likely due to PAH features from star formation at 6.2μm and 7.7μm being detected in IRAC's 8.0μm bandpass; note that Coma's proximity means we detect even the faintest members. There is one member with a significantly redder [3.6]−[4.5] color that is a disk galaxy viewed at an intermediate angle, but it is not an IR-AGN from the Stern et al. (2005) criteria and is not classified as an optical AGN in the recent survey of Coma by Mahajan et al. (2010).

4.3.2.2 Abell 1689

Spectroscopically confirmed members and their photometry are from Duc et al. (2002). The scatter in [5.8]−[8.0] color among members can be attributed to PAH features at 3.3, 6.2 and 7.7μm in dusty star forming galaxies where the latter two

features both shift into the 8.0μm channel. However, the 3.3μm PAH feature shifts to the boundary between channels 1 & 2. We find one candidate IR-AGN for this low redshift cluster that has also been classified as a Seyfert 1 AGN based on optical spectroscopy Duc et al. (2002). This prior study of Abell 1689 included mid-IR measurements from ISOCAM and the authors concluded that dusty star formation in this cluster is responsible for the vast majority of the observed mid-IR emission. Our results support this conclusion as we find no other members with infrared AGN signatures.

4.3.2.3 MS 1358+62

Photometry and spectroscopic information of MS 1358 members is from Fisher et al. (1998). At $z = 0.33$, the 3.3 and 6.2μm PAH features shift into IRAC channels 2 & 4 respectively and colors along both axes are redder. This explains the dispersion seen in Figure 4.3 for late-type galaxies that are likely to be star forming. The spectroscopic study of this cluster by Fisher et al. (1998) revealed a number of emission line galaxies (ELGs). Not surprisingly, nearly all of the galaxies that depart from the "passive cloud" are also ELGs. Of the galaxies in this cluster, we find one candidate AGN that is hosted by a late-type spiral. Martini et al. (2009) find no X-ray AGN in this cluster with L(2-8 keV) $\geq 10^{43}$ ergs s^{-1}. The one galaxy that we select as an AGN is detected as an ELG located roughly 860 kpc from the cluster center.

4.3.2.4 CL 0024+17

Spectroscopy and photometry for CL 0024 is from Moran et al. (2007a). star forming members with PAH emission are subject to the same effects as described for MS 1358 and thus produce a similar scatter in mid-IR color-color space. The scatter here makes it difficult to discern the nature of the galaxies that are found near the

boundary of the wedge. We do find two galaxies in the AGN-wedge (one appears to be sitting on the boundary). For the galaxy on the boundary, it is probable that star formation is producing its colors, though it is not ruled out as hosting an IR-weak AGN. The other candidate AGN we find shows colors consistent with a power-law spectrum placing it well inside the IRAC wedge. Zhang et al. (2005) have conducted an X-ray observation of this cluster locating a handful of point sources at $L_X > 10^{42}$ ergs s^{-1}. However, none of the X-ray point sources overlap with any cluster galaxies from the spectroscopic catalog, i.e. these X-ray sources are in the field.

CL 0024 is known to have numerous substructures as traced by three techniques: weak-lensing map (Kneib et al. 2003), X-ray shock fronts (Zhang et al. 2005) and a Dressler-Shectman test (Moran et al. 2007a, Dressler & Schectman 1988). This implies that many galaxies are in groups that have been recently accreted (or are in the process) into the main cluster. Furthermore, the redshift distribution of galaxies shows a bimodality that suggests a recent merger along the line of sight with a large galaxy group (Czoske et al. 2001, 2002). The one candidate AGN that is well inside the wedge has two close neighbors (confirmed spectroscopically) and is located ∼0.84 Mpc from the cluster center (see Figure 4.4). Redshifts of these galaxies are consistent with the main cluster. The candidate IR-AGN that we find near the edge of the IRAC-wedge is also within the main cluster; it is closer to the cluster core (∼340 kpc) but is >80 kpc from the nearest neighboring galaxy.

4.3.2.5 MS 0451-03

Spectroscopy and photometry for MS 0451 are also from Moran et al. (2007a). At $z = 0.54$, the 6.2μm PAH feature shifts nearly outside the IRAC window. This reduces the scatter in mid-IR color due to star formation for members. X-ray data have shown that the distribution of the cluster ICM is predominantly elliptical (Don-

ahue et al. 2003), and the redshift distribution of cluster galaxies is broadly Gaussian (Moran et al. 2007a). This indicates that MS 0451 is predominantly virialized with no substantial infalling galaxies. We detect no IR-AGN and no cluster galaxies are detected as X-ray sources based on a *Chandra* survey (Molnar et al. 2002), further indicating a lack of strong nuclear activity in MS 0451.

4.3.2.6 MS 2053-04

Spectroscopic and photometric information of galaxies in this cluster come from Tran et al. (2005a). Detailed spectroscopic and gravitational lensing studies of MS 2053-04 (Verdugo et al. 2007, Tran et al. 2005a) show that it is a merger of two structures with 113 and 36 confirmed members respectively. Galaxies in the smaller structure (2053-B) have similar properties to field galaxies not associated with the cluster. This, coupled with the high fraction of star forming members ($\sim$44%), suggests that MS 2053 has yet to completely virialize.

Observations with *Spitzer*/MIPS also find that a fairly high fraction ($\sim$18%) of cluster members are detected at 24μm (Saintonge et al. (2008)), and the large population of star forming members clearly separates from the passive members in mid-IR color. Given the high level of activity in MS 2053, it is surprising then that it only has one weak IR-AGN candidate. Using archival *Chandra* data, Eastman et al. (2007) find five X-ray sources at the redshift of MS 2053 with $L_{X,H} > 10^{42}$ ergs/s. However, three are not classified as cluster members due to their distances from the cluster center ($r > r_{200}$) and another is the BCG which is thought to be contaminated by X-ray emission from the ICM. This leaves only one cluster X-ray AGN which has a [3.6]$-$[4.5] color that is bluer than the IR-AGN selection region (Figure 4.3).

4.3.2.7 MS 1054-03

Spectroscopically confirmed members and photometry are taken from Tran et al. (2007). One cluster X-ray source was not included in the photometric catalog, but optical and X-ray data for this galaxy are available from Martel et al. (2007). Weak-lensing and X-ray analyses of MS 1054 show a clumpy nature to the dark matter and ICM profiles (Jee et al. 2005b). The presence of such substructure indicates that the cluster experienced a merger and has yet to become fully virialized.

Earlier studies of MS 1054 reveal that it contains two members hosting X-ray AGN (Johnson et al. 2003) and 8 radio sources that can be powered by AGN or star formation (Best et al. 2002). We find only one infrared AGN at a distance >1 Mpc from the cluster center that is also detected as both an X-ray and radio source. The second X-ray source lies near the edge of the IRAC footprints and is not detected at 5.8μm. Though this does not allow it to be identified as IR-AGN, it is not ruled out based on its [3.6]−[4.5] color (Figure 4.3).

4.3.2.8 RX J0152-13

Spectroscopic membership of cluster galaxies is from Demarco et al. (2005) and photometry from Blakeslee et al. (2006). This cluster shows signs of having gone through a large-scale merger event recently as indicated by its X-ray emission, luminosity distribution and weak-lensing profile (Jee et al. 2005a).

We detect two IR-AGN in this cluster, both of which are classified as X-ray QSOs (Martel et al. 2007); no other cluster galaxies are detected as X-ray sources. One of the IR+X-ray AGN is about 800 kpc from the cluster core while the second appears to be in a merging system. The latter detection is associated with five cluster galaxies within a projected radius of 30 kpc (Figure 4.4, neighboring cluster galaxies are labeled). Due to their proximity and the IRAC PSF, these galaxies are

blended into one mid-IR source where galaxy a is the closest ($\sim$0.7") to the centroid of the mid-IR emission. Redshifts in this quintet are 0.867, 0.864, 0.834, 0.832 and 0.836 for galaxies a, b, c, d and e respectively. Based on these redshifts, recessional velocities ($w.r.t.$ to galaxy c) are 3743, 3408, 0, -231 and 231 km/s for galaxies a, b, c, d and e respectively. Since galaxies a & b have velocities within 400 km/s and galaxies c, d & e have velocities within 500 km/s (typical of galaxy groups) we suspect a & b are a bound system and c, d & e are another bound system. Note, however, that a chance alignment of two groups such as this is $\sim$0.1% likely to occur at random assuming a spherical cluster geometry with $R \approx 1$ Mpc. Of course, due to the complex morphology and substructure in RX J0152 (Jee et al. 2005a) this probability may increase.

4.3.2.9 RDCS J1252-29

At $z = 1.24$, RDCS 1252 is the most distant cluster in our sample yet has a virial mass similar to those of the lower redshift clusters as well as other properties (Rosati et al. 2004). Close inspection of the ICM in the cluster core reveals the presence of a shock front, signaling a recent merger with a cluster sub-clump. A detailed spectroscopic follow-up (Demarco et al. 2007) verifies that the system is a merger of two groups that have yet to viralize, and weak lensing shows that the centroid of the dark matter mass profile is offset from the optical/X-ray centroid by $\sim$8" (Lombardi et al. 2005). Yet despite its young dynamical age, RDCS 1252 already has a population of luminous early-type galaxies that show little sign of ongoing star formation.

At this redshift, emission from stellar populations begins to encroach into the IRAC window. This effect can be seen in Figure 4.3 as an upward shift in the the "passive cloud" relative to the lower-z clusters. This unfortunately brings the

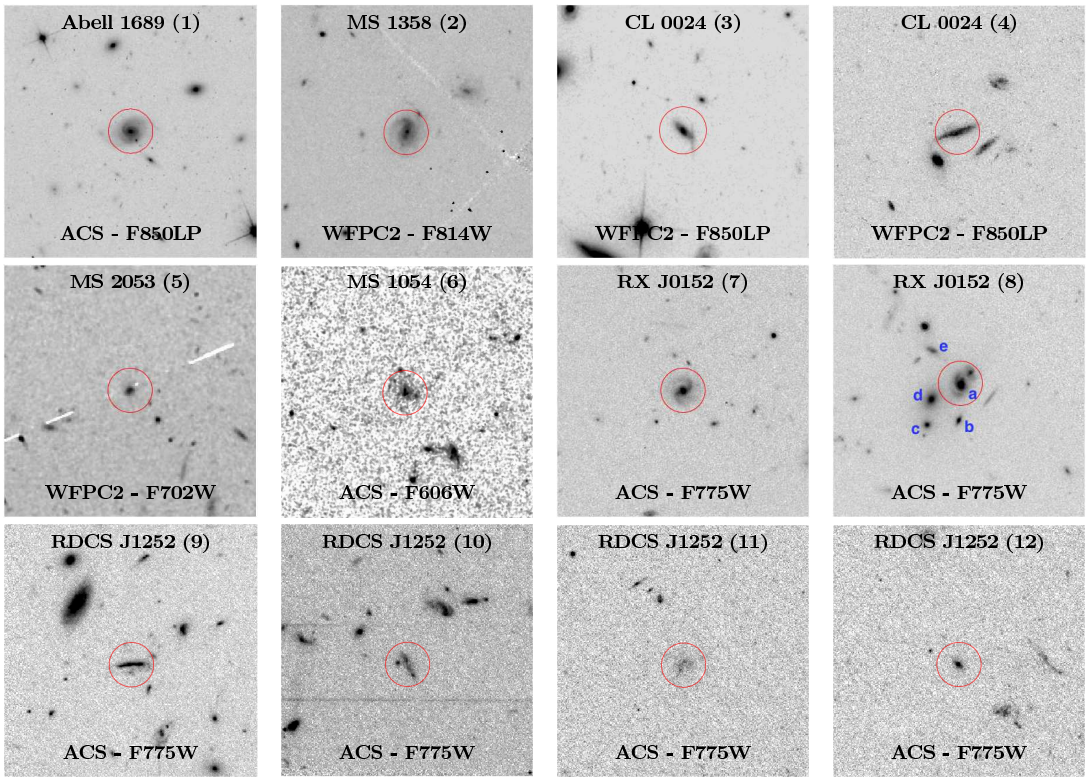

Figure 4.4: Thumbnails of Cluster IR-AGN.
Thumbnails of our sample of infrared-selected AGN; images are from the *Hubble* Space Telescope. Numbers in parentheses correspond to the ID from Table 4.3. All images are ∼150×150 kpc and are oriented North-up, East-left. Red circles correspond to the aperture of constant size ($r \approx 12.6$ kpc) used to perform photometry on the IRAC images. See §4.3.2.8 for an explanation of the labels in panel 8.

"passive cloud" closer to the AGN-wedge, possibly introducing contamination. Of the twenty nine RDCS 1252 members shown in Figure 4.3, four are inside the AGN-wedge, of which one has been previously identified as an X-ray AGN (Martel et al. 2007, Demarco et al. 2007). Three of the four candidate IR-AGN are hosted by morphologically irregular galaxies (Figure 4.4) that are likely to be gravitationally disrupted because of the large-scale cluster merger or by galaxy-galaxy mergers (*HST* image from Blakeslee et al. (2003) and Demarco et al. (2007).

Table 4.3: IRAC-selected Cluster AGN.

ID	Cluster	RA (J2000)	Dec (J2000)	z^a	R_{proj} [b]	$M_{3.6}$[c]	HR[d]	log(L_X)[e]	Morph.[f]
1	Abell 1689	13 11 35.5	−01 20 12.8	0.2000 (1)	0.30	-21.66±0.04	—	—	Sc
2	MS 1358	13 59 24.0	+62 31 08.0	0.3236 (2)	0.86	-21.64±0.03	—	—	Sc
3	CL 0024	00 26 40.0	+17 09 41.8	0.3955 (3)	0.33	-21.36±0.05	—	—	Sa+b
4	CL 0024	00 26 33.7	+17 12 19.8	0.3964 (3)	0.84	-21.64±0.05	—	—	Sc+d
5	MS 2053	20 56 21.0	−04 37 22.8	0.5763 (4)	0.19	-21.48±0.10	—	—	S0/a
6	MS 1054	10 57 02.7	−03 39 43.6	0.8319 (5)	1.02	-24.12±0.07	0.03±0.18	43.23	Irr
7	RX J0152	01 52 43.8	−13 59 01.3	0.8201 (5)	0.78	-23.61±0.08	-0.62±0.05	44.18	Sb
8	RX J0152	01 52 39.8	−13 57 40.7	0.8300 (5)	0.48	-24.88±0.07	-0.09±0.07	44.52	merger
9	RDCS 1252	12 52 55.6	−29 27 09.7	1.2274 (6)	0.15	-21.85±0.12	—	—	Irr
10	RDCS 1252	12 52 57.4	−29 27 32.0	1.2322 (6)	0.35	-22.28±0.12	—	—	Irr
11	RDCS 1252	12 52 49.8	−29 27 54.7	1.2382 (6)	0.59	-22.95±0.12	0.20±0.31	43.15	Irr
12	RDCS 1252	12 52 49.7	−29 28 03.7	1.2382 (6)	0.65	-22.61±0.12	—	—	S0

[a] Spectroscopic redshift: (1) Duc et al. (2002) ; (2) Fisher et al. (1998) ; (3) Moran et al. (2007a) ; (4) Tran et al. (2005a) ; (5) Holden et al. (2007) ; (6) Demarco et al. (2007).

[b] Projected distance from the cluster center in Mpc.

[c] Rest-frame 3.6μm absolute magnitude.

[d] X-ray hardness ratio from Martel et al. (2007) for AGN with X-ray detections.

[e] Hard X-ray (2-10 keV) luminosity in ergs s^{-1} from Martel et al. 2007.

[f] Morphology references: Coma: Michard & Andreon (2008), Abell 1689: Duc et al. (2002), MS 1358: Fabricant et al. (2000), CL0024: Moran et al. (2007a), MS 0451: Moran et al. (2007a), MS2053: Tran et al. (2005b), MS 1054: Blakeslee et al. (2006), RXJ0152: Blakeslee et al. (2006)and RDCS J1252: Demarco et al. (2007).

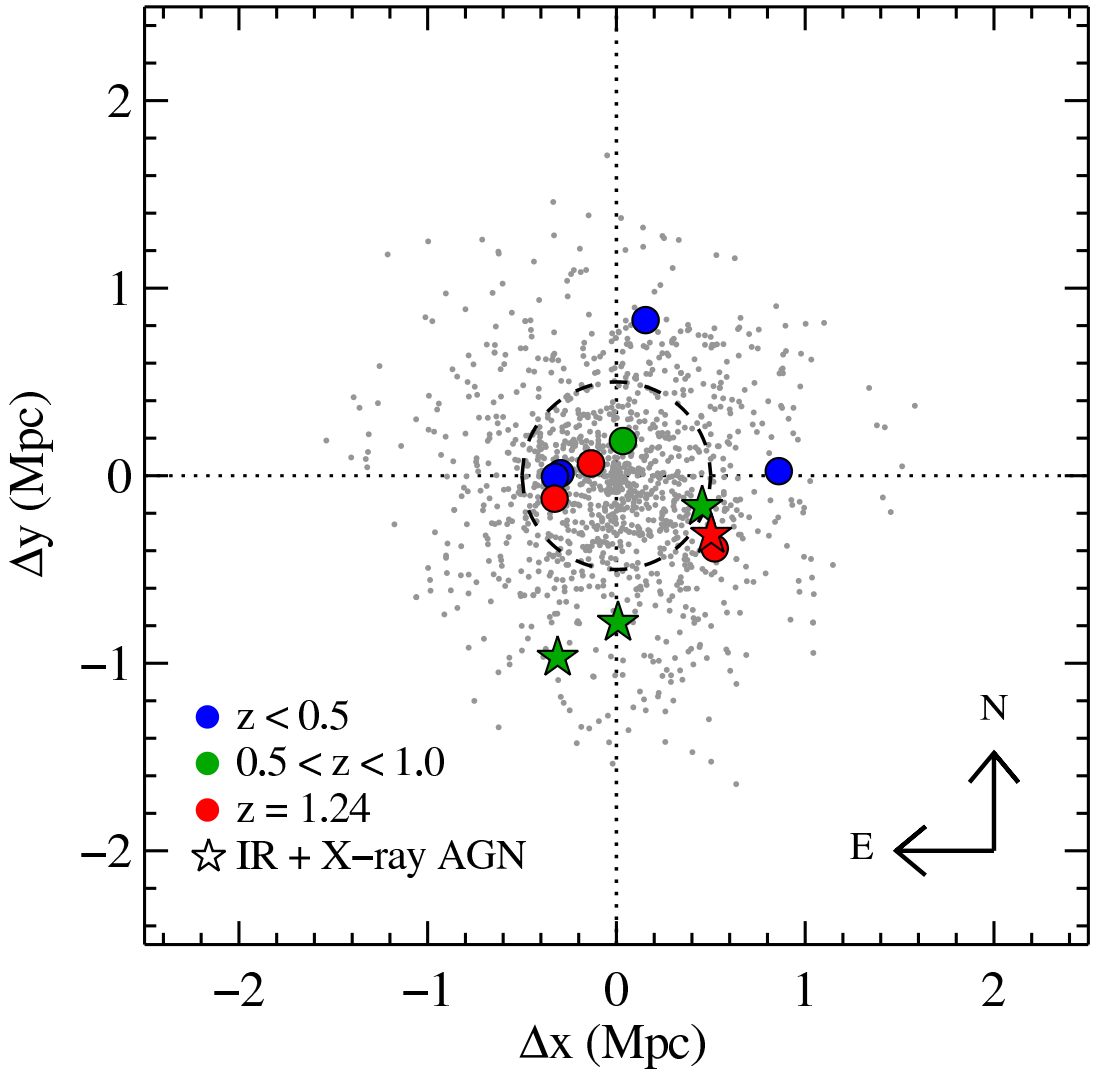

Figure 4.5: Spatial Distribution of Cluster IR-AGN.
Combined sky-plot for each cluster showing the projected locations of galaxies with respect to their cluster centers. IRAC-selected AGN are shown as circles (or stars for X-ray sources) and the dashed circle corresponds to a physical radius of 0.5 Mpc. Colors correspond to three bins is redshift, $z < 0.5$ (blue), $0.5 < z < 1.0$ (green) and $z = 1.24$ (red). A Kolmogorov-Smirnov test shows that the radial distribution of the IR-AGN is >99% likely to come from the same parent population as the normal cluster galaxies (gray points).

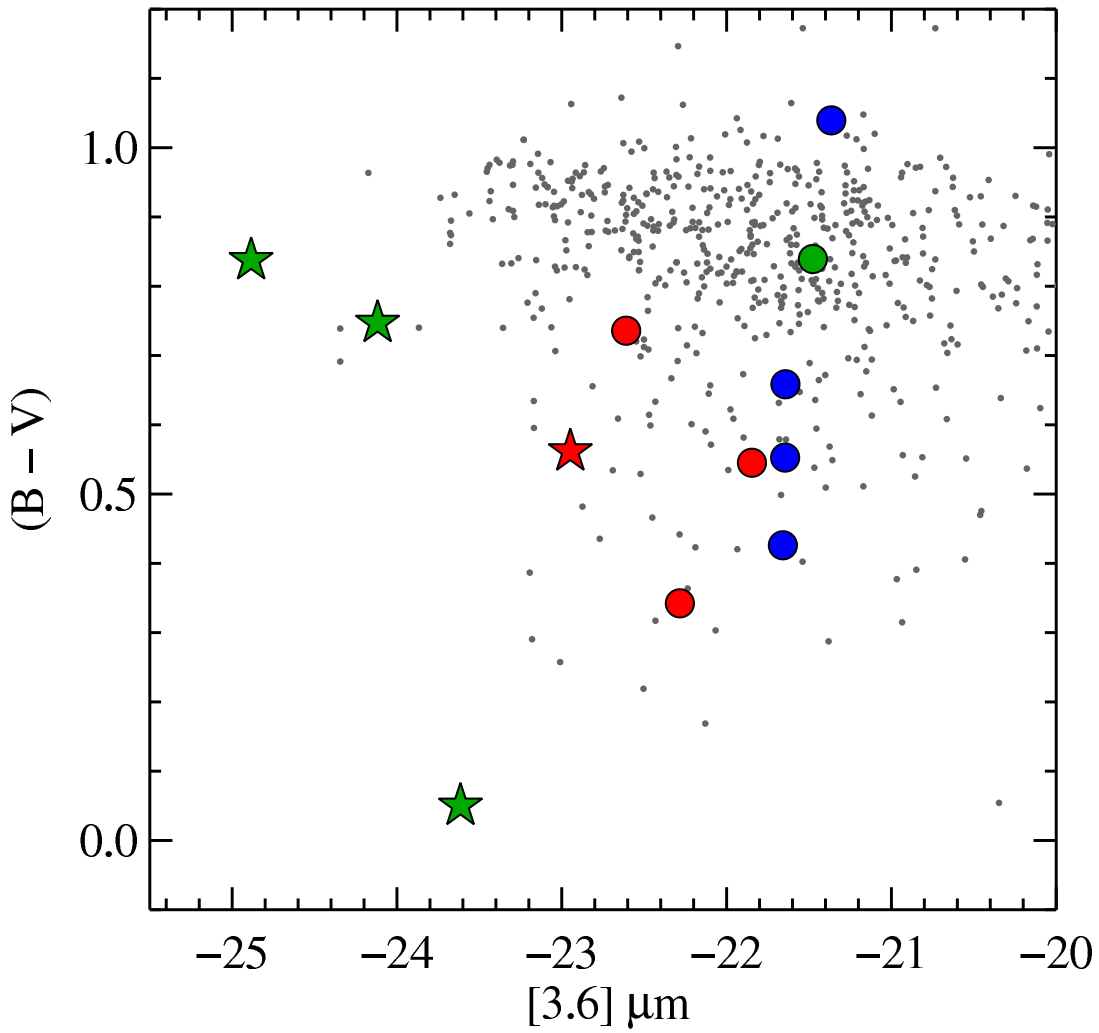

Figure 4.6: CMR of Cluster IR-AGN.
Rest-frame color-magnitude relation (optical color vs. 3.6μm absolute magnitude); symbols are the same as in figure 4.5. Host galaxies of IR-AGN tend to have blue optical colors, thus these IR-AGN hosts have recent/ongoing star formation. Also, the four most luminous cluster IR-AGN are also X-ray sources.

4.4 Discussion

4.4.1 Cluster IR-AGN Properties

Recent studies of field galaxies find that infrared-selected AGN share similar properties (Hickox et al. 2009, Griffith & Stern 2010): their host galaxies typically have late-type morphologies and tend to have blue optical colors. The properties of our 12 cluster IR-AGN agree with these earlier studies. We find the majority of our IR-selected AGN (10/12) are in late-type galaxies (Table 4.3) that are blue (Fig. 4.6) and so have recent/ongoing star formation. The remaining two cluster IR-AGN are hosted by S0 galaxies that lie on/near the IR-AGN boundary (Fig. 4.3) and these members are consistent with being spiral galaxies transitioning to early-type systems in the cluster environment (Dressler et al. 1997, Moran et al. 2007a).

It is worth noting that optical light from host galaxies may be contaminated by emission from an AGN, thus their colors could be biased blue-wards. Our bluest AGN host, for example, is likely contaminated by the central engine since it is such a strong outlier. Figure 4.4 shows ACS & WFPC-2 images of our IR-selected AGN, nearly all at rest-frame blue wavelengths. Upon careful visual inspection we find that the majority of these galaxies have extended morphologies and are not strongly dominated by a central point source. Furthermore, Hickox et al. (2009) calculated color contamination to be < 0.3 mag in ${}^{0.1}(u-r)^{*}$. When considering that the optical filters we use $(B-V)$ are closer together in wavelength space and that AGN generally contribute more flux at bluer wavelengths, we expect color contamination in our sample to be less than what Hickox et al. (2009) find. Therefore, although point source contamination may be impacting some of our sample, we conclude that color contamination of our IR-AGN hosts is not significant enough to bias our results.

$*$ This color is computed by blueshifting the SDSS u & r filters by $z = 0.1$

We find that a third (4/12) of our cluster IR-AGN are also known X-ray sources (Martel et al. 2007, Johnson et al. 2003), a fraction that is nominally consistent with results from the AGN and Galaxy Evolution Survey (AGES) where $\sim 50\%$ of IR-AGN are also X-ray sources (Hickox et al. 2009). However, it is worth mentioning here that X-ray flux limits are not the same among these studies, and so agreement on this ratio is not necessarily implied. The X-ray sources are also the four most luminous 3.6μm IR-AGN (rest-frame; Figure 4.6); however, note that the most luminous cluster IR+X-ray AGN is the blended source in RX J0152 (see §3.2.8).

Figure 4.5 shows the projected distances of the 12 IR-AGN relative to confirmed members in all nine galaxy clusters. We find the radial distribution of the IR-AGN is drawn from the same parent population as the cluster galaxies with $> 99\%$ confidence using a Kolmogorov-Smirnov test. However, the four IR+X-ray AGN are all outside the cluster cores at $R_{proj} > 0.5$ Mpc. This result is consistent with Eastman et al. (2007) and Atlee et al. (2011) who find that X-ray sources in galaxy clusters are not strongly centrally concentrated. Our observations may suggest that IR+X-ray AGN represent a different population than IR-only AGN; however, we are limited by the size of our sample and so cannot further postulate on the uniqueness of these AGN based on their spatial distribution and 3.6μm luminosities.

4.4.2 Infrared-AGN Fractions

To measure the fraction of IR-AGN in our cluster sample and test for evolution, we separate our sample into three redshift bins: low redshift (< 0.5), intermediate redshift ($0.5 < z < 1.0$), and a high redshift point at $z = 1.24$ (RDCS 1252) containing 543, 377 and 29 IRAC detected members respectively. To ensure robustness, we consider two different galaxy samples selected optically and in the mid-IR. We also take into account the varying spatial coverage of the IRAC mosaics and set the max-

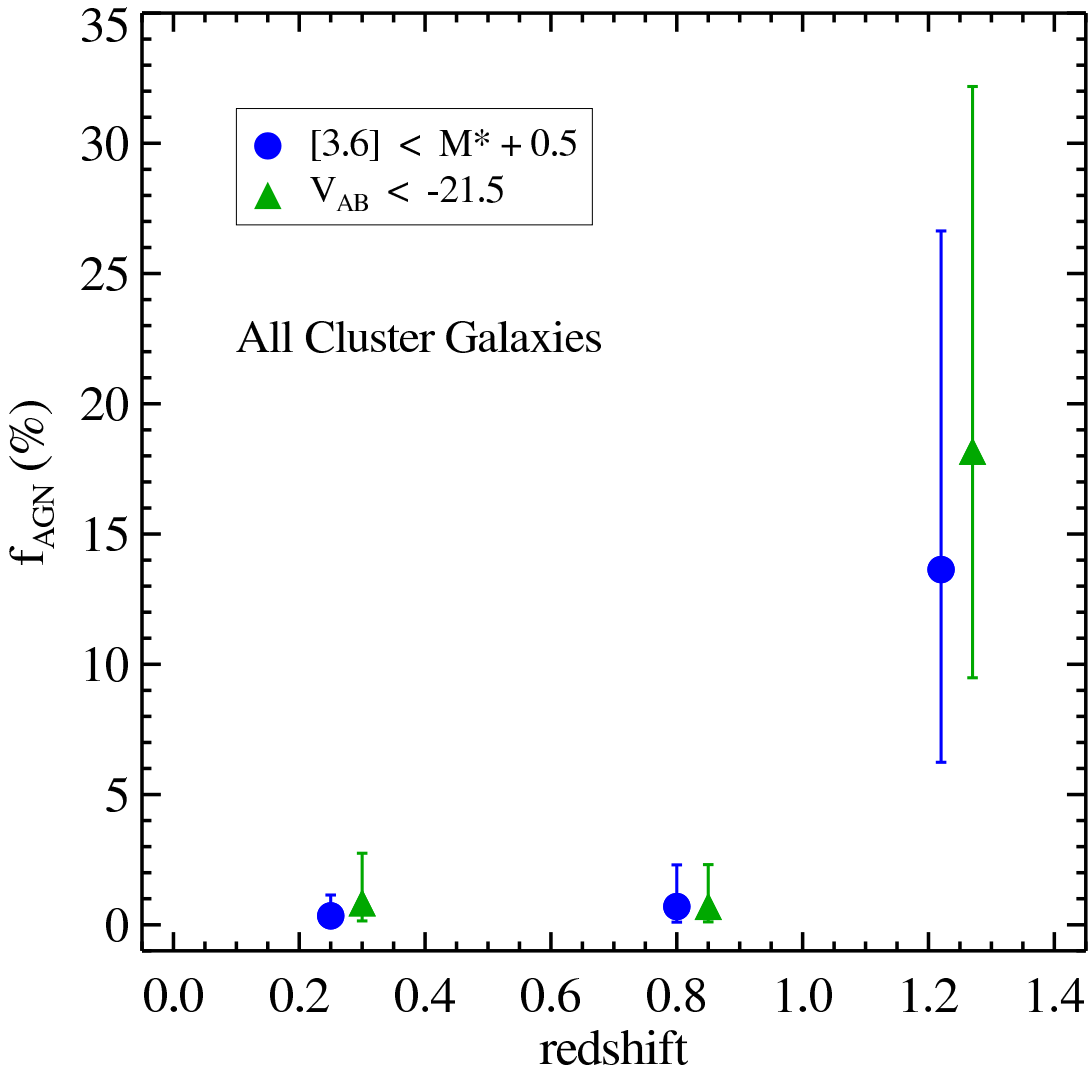

Figure 4.7: Cluster IR-AGN Fractions: Total.
Cluster IR-AGN fraction as a function of redshift for optically selected members brighter than $V_{AB} = -21.5$ mag (green triangles) and mid-IR selected members brighter than $(M^*_{3.6} + 0.5)$ (blue circles). We consider three redshift bins: low redshift ($z < 0.5$), intermediate redshift ($0.5 < z < 1.0$), and a high redshift point at $z = 1.24$ (RDCS 1252) that contain 543, 377, and 29 IRAC-detected members respectively. The IR-AGN fraction is uniformly $< 3\%$ at $z < 1$ and only measurably higher in RDCS 1252 at $z = 1.24$. Error bars represent 1σ Poisson uncertainties derived using statistics from Gehrels (1986).

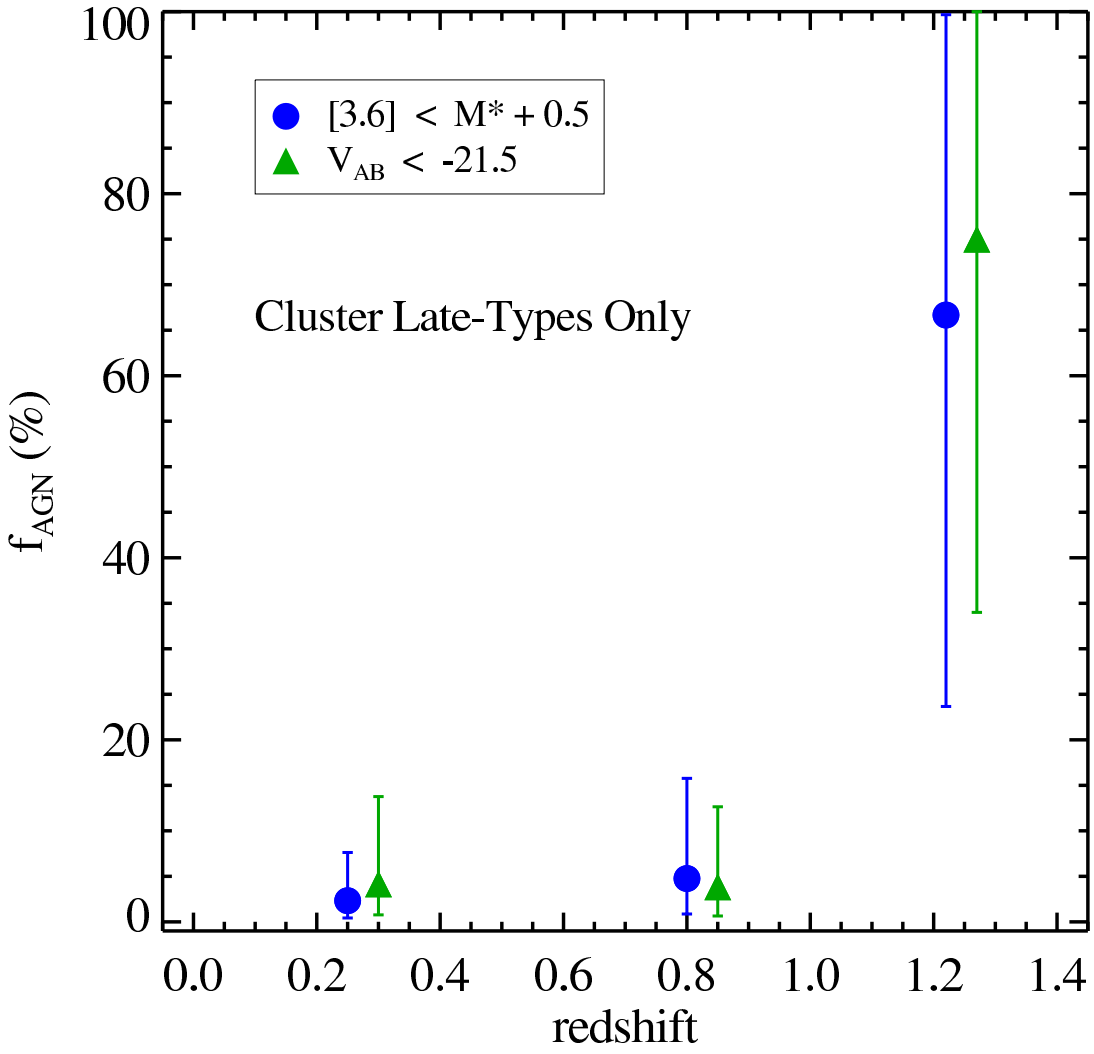

Figure 4.8: Cluster IR-AGN Fractions: Late Types.
Same as Fig. 4.7 but only considering late-type galaxies (i.e. excluding E/S0 galaxies). The IR-AGN fraction remains $< 5\%$ at $z < 1$ and is higher only at $z = 1.24$.

Table 4.4: IR-AGN Fractions.

Selection[a]	z-bin	N_{AGN}	N_{tot}	$f_{\rm IR-AGN}$[b]
All Cluster Members	$(z < 0.5)$	1	291	$0.3^{+0.8}_{-0.3}$ %
$M_{3.6} < M^*_{3.6} + 0.5$ mag	$(0.5 < z < 1.0)$	1	143	$0.7^{+1.6}_{-0.6}$ %
	$z = 1.24$	3	22	$13.6^{+13}_{-7.4}$ %
All Cluster Members	$(z < 0.5)$	1	118	$0.8^{+1.9}_{-0.7}$ %
$V_{AB} < -21.5$ mag	$(0.5 < z < 1.0)$	1	141	$0.7^{+1.6}_{-0.6}$ %
	$z = 1.24$	4	22	$18.2^{+14}_{-8.7}$ %
Late-Types Only	$(z < 0.5)$	1	43	$2.3^{+5.3}_{-1.9}$ %
$M_{3.6} < M^*_{3.6} + 0.5$ mag	$(0.5 < z < 1.0)$	1	21	$4.7^{+11}_{-3.9}$ %
	$z = 1.24$	2	3	67^{+33}_{-43} %
Late-Types Only	$(z < 0.5)$	1	24	$4.1^{+9.6}_{-3.4}$ %
$V_{AB} < -21.5$ mag	$(0.5 < z < 1.0)$	1	26	$3.8^{+8.8}_{-3.2}$ %
	$z = 1.24$	3	4	75^{+25}_{-41} %

[a] Selections are based on rest-frame 3.6μm and V_{AB} respectively.
[b] Uncertainties represent 1σ Poisson errors determined from Gehrels (1986).

imum field of view with the Coma cluster where the IRAC footprint only includes galaxies within $R_{proj} \sim 760$ kpc of the cluster center. In the higher redshift clusters, we therefore exclude members that are at $R_{proj} > 760$ kpc from their cluster center.

Our first cluster galaxy sample is composed of optically-selected members brighter than $V = -21.5$ (this corresponds to where the V-magnitude distribution turns over for RDCS 1252, our most distant cluster); this yields 118, 141 and 22 galaxies in our three redshift bins. Note we do not correct for passive evolution given that the host galaxies of the IR-AGN tend to have blue optical colors, i.e. are likely star forming systems. The IR-AGN fraction for this optically-selected sample is $\sim 1\%$ for both redshift bins at $z < 1$ and is only measurably non-zero at $z = 1.24$ with $f_{\rm IR-AGN}$=$18.2^{+14}_{-8.7}$% (Table 4.4; Fig. 4.7). All errors in $f_{\rm IR-AGN}$ are asymmetric 1σ Poisson uncertainties as determined by Gehrels (1986) for small number samples.

Our second cluster galaxy sample is composed of members selected based on rest-frame 3.6μm luminosity. Because the evolution of the 3.6μm luminosity function is well-characterized by passively evolving galaxies that formed at $z > 1.5$ (Muzzin et al. 2008), this luminosity selection is effectively a stellar mass cut. To isolate comparable samples of cluster members over our redshift range, we combine values of $M^{\star}(z)[3.6\mu\mathrm{m}]$ (the characteristic turning point in the Schechter luminosity function; Schechter 1976) from Muzzin et al. (2008) with the 80% limiting magnitude for our most distant cluster and thus select members brighter than rest-frame $(\mathrm{M}^{*}_{3.6}(z)[3.6\mu\mathrm{m}] + 0.5)$. We find that the cluster IR-AGN fraction is again uniformly $\sim 1\%$ at $z < 1$ and only measurably non-zero at $z = 1.24$ with $f_{\mathrm{IR-AGN}}$=$13.6^{+13}_{-7.4}\%$ (RDCS 1252; Table 4.4; Fig. 4.7).

Thus far we have included all cluster galaxies regardless of morphology in determining $f_{\mathrm{IR-AGN}}$, but this may introduce a bias given that: 1) our cluster IR-AGN are predominantly hosted by late-type galaxies and 2) the morphological mix in clusters evolves with redshift (Dressler et al. 1997, Fasano et al. 2000, Postman et al. 2005, Capak et al. 2007b). In Fig. 4.8 we now exclude all morphologically classified E/S0 members and measure a higher $f_{\mathrm{IR-AGN}}$ at all redshifts (Table 4.4). However, $f_{\mathrm{IR-AGN}}$ remains $< 5\%$ at $z < 1$ in both of our selected galaxy samples. Only in the most distant cluster (RDCS 1252) does $f_{\mathrm{IR-AGN}}$ for late-type* members increase to $\sim 70\%$.

Although the number of cluster IR-AGN is small, we stress that our analysis is based on a sample of $\sim$ 1500 spectroscopically confirmed cluster galaxies at $0 < z < 1.3$, thus we place a strong upper limit on the IR-AGN fraction of $< 3\%$ for all members in massive clusters at $z < 1$. One caveat to consider is that while the IR color selection does identify $\sim 90\%$ of broad-line AGN, it misses $\sim 60\%$ of

* Here we mean all members except for E/S0s.

narrow-line AGN (Stern et al. 2005) and so we may be underestimating $f_{\rm IR-AGN}$. However, strongly starbursting galaxies may also contaminate our IR-AGN sample (up to $\sim 50\%$; Donley et al. 2008), and accounting for these actually decreases the IR-AGN fraction. Addressing these two competing effects is beyond the scope of our current analysis.

The low IR-AGN fraction of $\sim 1\%$ in our massive clusters at $z < 1$ is consistent with Martini et al. (2009) who estimate an X-ray AGN fraction of $0.13 - 1.00\%$ in clusters at $\bar{z} \sim 0.2$ to $\bar{z} \sim 0.7$ and with Hickox et al. (2009) who find the IR-AGN fraction in AGES is comparable to the X-ray AGN fraction at $0.25 < z < 0.8$. However, we cannot say for certain that there is strong evolution in the cluster IR-AGN fraction with redshift given our small numbers. This is in contrast to the observed increase in the fraction of (dusty) star forming members in these same clusters (Saintonge et al. 2008), thus the bulk of their 24μm flux is due to star formation and not AGN. Our single galaxy cluster at $z > 1$ does suggest that IR-AGN have a more prominent role at this epoch, but we recognize that 1) RDCS 1252 may be unusually active and 2) the IRAC color selection starts to suffer contamination from passive galaxies at these redshifts. Given their rarity, a larger survey of IR-AGN in massive galaxy clusters, particularly at $z > 1$, is needed to robustly identify any evolution in IR-AGN with redshift.

Another interesting comparison we can study is the variation in $f_{\rm IR-AGN}$ with environment. Using magnitude cuts similar to our $V \leq -21.5$ limit, the $f_{\rm IR-AGN}$ in the Boötes field sample from the AGES ($0.25 < z < 0.8$) is $\sim$2% (R. Hickox, private communication). This is well within our upper 1σ uncertainty (Table 4.4) at similar redshifts, thus there is no clear variation in $f_{\rm IR-AGN}$ based on local density. The possibility of AGN playing a more influential role at $z > 1$ still remains.

5. SUMMARY

To summarize, it has long been recognized that the formation and evolution of galaxies is complex and non-linear. In contrast, the evolution of individual stars is quite well understood as it has been found to be predominantly dependent on only one property, mass at the time of formation. Research in galaxy evolution, however, has identified a multitude of relevant properties and processes including radiative transfer, morphology, environment, metallicity, mass of the host dark matter halo and hydrodynamical interactions with supernovae and active galactic nuclei. Furthermore, these processes span a large range of physical scales including interactions within individual star clusters (∼pc) up to large-scale galactic environments (∼Mpc). This complicates the creation of a coherent evolutionary model capable of explaining the wide diversity in the observed galaxy population. In this work we present a series of measurements and analyses of the bulk population of galaxies with a focus on the buildup of stellar matter using cutting-edge datasets from ZFOURGE, CANDELS, and the *Spitzer* and *Herschel* space observatories. These improved observational constraints will be important for informing the construction of models of galaxy formation/evolution.

5.1 Updating the Observed Stellar Mass Function*

We start with measuring the galaxy stellar mass function over a broad redshift range ($0.2 < z < 3$). Using the deep H_{160}-band imaging from CANDELS, we detect mass-complete samples of red and blue galaxies. This in combination with medium-band near-IR imaging from ZFOURGE allows us to construct a large sample of

* Reprinted with permission from "Galaxy Stellar Mass Functions from ZFOURGE/CANDELS: An Excess of Low-mass Galaxies since z = 2 and the Rapid Buildup of Quiescent Galaxies" by Tomczak et al., 2014. The AstroPhysical Journal, 783, 85-99, Copyright 2014 by Adam Tomczak.

galaxies complete to low stellar masses with accurate photometric redshifts. Our final sample covers a combined area of 316 arcmin^2 to a depth of $H_{160} = 25.9$. We also include data from NMBS in our sample which adds $\sim$1300 arcmin^2 at a 5σ depth of $K_s < 22.8$ to help constrain the high-mass end. Our data allow us to probe the SMF down to stellar masses of $\approx 10^{9.5} M_\odot$ at $z < 2.5$.

We show in Figure 2.7 that the low-mass end of the quiescent SMF exhibits rapid evolution between $z = 1.5$ and today. We calculate greater than a factor of 10 increase in the number of quiescent galaxies at stellar masses $< 10^{10} M_\odot$. Since the expected source of low-mass quiescent galaxies is low-mass star-forming galaxies that have become quenched, this leads to the question of what is/are the dominant quenching process/processes for low-mass galaxies. This effect could be the result of a growing population of low-mass galaxies being accreted onto larger halos and having their star-formation quenched in the process. Several studies have suggested that environmental processes become increasingly important in the quenching of star formation at low masses (e.g. Hogg et al. 2003, Peng et al. 2010, Geha et al. 2012, Quadri et al. 2012), implying that the differential buildup in the quiescent SMF is at least partially due to the evolving role of environment.

The SMF at $z \leq 1.5$ has been known to exhibit a steepening of the faint-end slope at $\log(M_*/M_\odot) < 10$, and is thus not well-characterized by a single-Schechter function (e.g. Baldry et al. 2008, Ilbert et al. 2013, Muzzin et al. 2013). We fit both single- and double-Schechter functions to all of our SMFs and assess which parameterization is better based on the reduced chi-squared statistic ($\chi^2_{\rm red}$). Our results show that a low-mass upturn is present in the SMF up to at least $z = 2$. We find no evidence for evolution in the characteristic mass ($M^* \approx 10^{10.65} M_\odot$) or the slope at low masses ($\alpha \approx -1.5$) at $0.2 < z < 2$ in our best-fit double-Schechter parameterizations. We also observe evidence of multiple-component behavior in the

star-forming and quiescent SMFs independently (see also Drory et al. 2009, Gilbank et al. 2011). It is important to note that the low-mass end of the SMF is dominated by star-forming galaxies with very blue colors at all redshifts. Such galaxies may be subject to systematic uncertainties in their redshift and mass estimates; while our photometric redshifts appear to be well-constrained (see Fig. 2.1), spectroscopic confirmation is necessary.

We also examine the growth in the SMFs of the star-forming and quiescent populations. We find that the SMF of star-forming galaxies increases moderately with cosmic time, by 1.5 - 2.5× since $z \sim 2$, but that the shape of the SMF does not change strongly. These results are consistent with previous work which has generally found that the star-forming SMF evolves relatively weakly with redshift (Bell et al. 2007, Pozzetti et al. 2010, Brammer et al. 2011, Muzzin et al. 2013). For quiescent galaxies we observe much more rapid growth in number density, and also a change in shape of the SMF. From $z = 2$ to $z = 0$ we find a ∼6× increase at masses $> 10^{10} M_{\odot}$ and ∼15 - 30× increase at masses $< 10^{10} M_{\odot}$.

Finally, we calculate the evolution of the cosmic stellar mass density at $z < 3$ integrated between $9 < \log(M_*/M_{\odot}) < 13$. We compare our results to measurements from UltraVISTA (Ilbert et al. 2013, Muzzin et al. 2013), which covers a much larger area but at a much shallower depth, as well as measurements from Santini et al. (2012), which reach a similar depth but over ∼$1/10^{\text{th}}$ of our survey area. Overall, we find good agreement with Santini et al. (2012) and Ilbert et al. (2013) at all redshifts. Results at $1.5 < z < 2.5$ from Muzzin et al. (2013), however, are less than what we find. We also compare to the inferred mass density from Reddy & Steidel (2009) derived from a rest-frame UV-selected galaxy sample corrected for incompleteness. From this corrected SMF Reddy & Steidel (2009) measure a value for the cosmic stellar mass density at $1.9 < z < 3.4$ that is similar to ours, despite

the use of very different types of data and different methods.

5.2 Deriving Empirical Star-Formation Histories

From here, we use deep far-IR (>20μm) imaging that overlaps with the ZFOURGE footprint from the *Spitzer* and *Herschel* space telescopes to measure the evolution of SFR$-M_*$ relation over much of the same redshift range as for the SMF. These far-IR data probe the obscured star-formation in galaxies which, in combination with the unobscured star-formation from rest-frame UV data, allow for the measurement of total star-formation rates. In agreement with recent results (Whitaker et al. 2014, Schreiber et al. 2015, Lee et al. 2015), we find that the SFR$-M_*$ relation is not consistent with a single power-law of the form SFR $\propto M_*^{\beta}$ at any redshift; it has a power-law slope of $\beta \sim 1$ at low masses, and becomes shallower above a turnover mass (M_0) that ranges from $10^{9.5}$–$10^{10.8}$ $M_\odot$, with evidence that M_0 increases with redshift. For the first time we parameterize the evolution of the transition mass finding evidence that it increases with redshift; this is true whether or not quenched galaxies are included. From our measurements we parameterize the evolution of the SFR$-M_*$ relation with respect to redshift: $\Psi(z, M_*)$.

We use two techniques to extract empirical star-formation and mass-growth histories from the observations. First, we integrate along the evolving SFR$-M_*$ sequence to estimate how galaxies should grow due to star-formation. Second, we estimate mass-growth histories from measurements of the galaxy stellar mass function using an evolving number density selection (NDS) criterion (Behroozi et al. 2013). It is worthwhile to note that both techniques used here provide *typical* SFHs along with a rough indication of the scatter, but that individual galaxies may follow very different evolutionary pathways (Kelson 2014, Abramson et al. 2015).

In contrast to the dramatic disagreement found in some previous studies that

were based on older measurements (Renzini 2009, Weinmann et al. 2012, Leja et al. 2015), we find broad agreement between the inferred evolution of star-formation rates and stellar masses of individual galaxies. However in detail there is a systematic difference in that the differential SFHs suggest more rapid mass evolution at higher redshifts than is inferred from the NDS samples. This disagreement in mass-growth rates is as high as $\sim$0.5 dex. At lower redshifts the NDS predict more rapid evolution; this can be naturally explained by galaxy mergers, and the size of the difference can be taken as a measure of the growth rate due to mergers (e.g. Drory & Alverez 2008, Moustakas et al. 2013).

The disagreement at $z < 1$ suggests that either our SFRs are overestimated, that the rate of mass-growth inferred from the stellar mass function is underestimated, or both. Errors in star-formation rate measurements may arise from low-level AGN activity, an incorrect conversion of flux to bolometric UV/IR luminosities, the assumed IMF, and variations in star-forming duty cycles as probed by UV and IR indicators. Stellar masses were estimated by fitting models to the observed spectral energy distributions (SEDs) of individual galaxies. Various assumptions that go into the SED-fitting process that are possible sources for systematic errors include smooth exponentially declining SFHs, a single dust screen, a constant IMF, solar metallicity, and assuming that emission lines do not contribute significantly to the observed photometry (for detailed discussions see Conroy 2013, Courteau et al. 2014).

The measurements on which this study is based were performed using high-quality data and standard methods. Moreover, the use of the same ZFOURGE sample for measuring both the SMF and the SFR$-M_*$ relations helps provide internal consistency for this work. Although the broad qualitative agreement that we find in mass-growth histories is encouraging for current studies of galaxy evolution, the disagreements may highlight the need to move beyond the simplistic assumptions that

underly current data analysis methods.

5.3 Investigating the Prevalence of AGN Feedback*

Lastly, we study in detail the prevalence of one possible mechanism responsible for quenching star-formation in galaxies: the presence of an active galactic nucleus (AGN). Active galactic nuclei are super-massive black holes at the centers of galaxies that are actively accreting matter from their surroundings. It has become apparent over the past decade that AGN are a necessary component in galaxy evolution models as a source of feedback to prevent the overcooling of gas and, consequently, overproducing stellar mass. We present the first census of mid-infrared selected active galactic nuclei (IR-AGN) in massive galaxy clusters ($M_{\rm vir} > 5 \times 10^{14} M_{\odot}$) at $0 < z < 1.3$ by combining archival *Spitzer*/IRAC imaging with extensive optical spectroscopic catalogs (public and private) and deep optical photometry of ~ 1500 confirmed members in nine clusters. Our clusters are selected to be the most massive well-studied systems currently known. Using the four IRAC channels (3.6, 4.5, 5.8 and 8.0μm) and established mid-IR color selection techniques (Stern et al. 2005, Lacy et al. 2004), we identify 949 members that are detected ($> 3\sigma$) in at least three of the four IRAC channels and isolate 12 that host dust-enshrouded AGN. Similar to IR-selected AGN in recent field studies (Hickox et al. 2009, Griffith & Stern 2010), the host cluster galaxies tend to be late-type members with blue optical colors that indicate recent/ongoing star formation. The IR-AGN have the same radial distribution as the cluster members, but the four most IR-luminous AGN lie outside of their cluster cores ($R_{proj} > 0.5$ Mpc) and are also known X-ray sources. This suggests that very bright IR+X-ray AGN are not centrally concentrated in their clusters, consis-

* Reprinted with permission from "A Census of Mid-infrared-selected Active Galactic Nuclei in Massive Galaxy Clusters at $0 < z < 1.3$" by Tomczak et al., 2011. The AstroPhysical Journal, 738, 65-77, Copyright 2011 by Adam Tomczak.

tent with the results for bright X-ray sources by Martini et al. (2009). Our results also suggest that IR+X-ray AGN may not be the same population as the IR-only AGN, but we are too limited by our sample to make any assertion.

To measure the fraction of IR-AGN and test for evolution, we compare two complete samples of cluster galaxies: 1) an optically-selected sample with members brighter than $V_{\rm AB} = -21.5$ (rest-frame) and 2) a mid-IR selected sample with members brighter than $(M^{\star}(z)[3.6\mu{\rm m}] + 0.5)$ (Muzzin et al. 2008) that is essentially a stellar mass cut. For the eight galaxy clusters at $z < 1$, we place a strong upper limit of $< 3\%$ on the fraction of IR-AGN for both cluster samples. Because IR-AGN tend to be hosted by late-type galaxies and the morphological mix in clusters evolves (Dressler et al. 1997, Postman et al. 2005), we also consider only late-type members and find that the fraction with IR-AGN is $< 5\%$ for both samples. These low IR-AGN fractions are surprising given that the fraction of (dusty) star formation in these same clusters increases by about a factor of four at $0 < z < 1$ (Saintonge et al. 2008, Bai et al. 2010). However, an IR-AGN fraction of $\sim 1\%$ is consistent with the low fraction of X-ray AGN in galaxy clusters ($\leq 1\%$ Martini et al. 2009) and the relative populations of X-ray vs. IR AGN (Hickox et al. 2009).

In contrast, our single galaxy cluster at $z = 1.24$ (RDCS 1252) has a measurably higher IR-AGN fraction of $\sim 15\%$ (all galaxy types) and $\sim 70\%$ (late-types only). However, RDCS 1252 may simply be an unusually active cluster. Also, the IR color selection starts to suffer stronger contamination from non-AGN members at $z > 1.2$.

We also compare our $f_{\rm IR-AGN}$ measurements in dense clusters at $z < 1$ to that of the Boötes field from the AGES, which probes sparser galactic environments over a similar range in redshift ($0.25 < z < 0.8$). Using optical magnitude cuts similar to this study, $f_{\rm IR-AGN}$ is measured to be $\sim$2% in the field (R. Hickox, private communication). Consequently, we do not see a statistically significant variation in

$f_{\rm IR-AGN}$ here that would be caused by local galaxy density. However, the question still remains as to whether or not IR-AGN have a more profound impact at $z > 1$.

We note that while the IR color selection successfully identifies $\sim 90\%$ of broad-line AGN, it does miss $\sim 60\%$ of narrow-line AGN (Stern et al. 2005) and so $f_{\rm IR-AGN}$ is undoubtedly incomplete, i.e. underestimated. On the other hand, contamination may arise from star forming galaxies falsely identified as IR-AGN; thus we may also be overestimating $f_{\rm IR-AGN}$. Such contamination can be as high as 20–50% (Donley et al. 2008, Hickox et al. 2009) and is more influential at low luminosities. For simplicity, we ignore these two competing effects because they are beyond the scope of our analysis and do not change our general conclusions.

Taken as a whole, our results show that IR-AGN and star formation are not strongly correlated at $z < 1$ because the IR-AGN fraction is uniformly very low ($\sim 1\%$) at $z < 1$ whereas several of these clusters have star forming fractions of $> 20\%$ (Saintonge et al. 2008).

5.4 Future Prospects

Ultimately, a full and complete picture of galaxy evolution still evades us. It is clear that some of this is caused by our incomplete understanding of star formation/evolution and interdependencies of various galactic properties that are poorly constrained. For example, the stellar initial mass function (the number of stars formed as a function of their mass) is known to be non-universal and several variants of it are currently known to exist. However, it is not understood what causes these variations or even if stars in the early universe formed according to a different, unknown IMF. To simplify modeling of stellar populations, typically a single IMF is assumed and applied universally. This type of simplification is also taken with other galactic properties that are known to be complex but are similarly poorly un-

derstood. Some examples include effects of metal enrichment, attenuation of light from interstellar dust, and the spatial distribution of interstellar dust in galaxies (for detailed discussions on these topics see Conroy 2013 and Courteau et al. 2013).

Nevertheless, a similarly large (if not larger) cause for the incomplete picture of galaxy evolution comes from current technical limitations. Although modern datasets have improved by orders of magnitude in terms of depth and coverage over the past decade, many current observational studies are limited to noise-dominated measurements when testing new/existing models. Similarly, computers are still not powerful enough to simulate galaxies at the necessary resolution to accommodate both small-scale and large-scale physics simultaneously, limiting the interpretations that can be drawn from them. Fortunately, next-generation observatories and instrumentation have either recently been commissioned (e.g. the Atacama Large Millimeter Array: ALMA, the Dark Energy Survey:DES, the Multi-Object Spectrometer For Infra-Red Exploration: MOSFIRE, and the Multi Unit Spectroscopic Explorer: MUSE) or are in the process of being commissioned within the next decade (e.g. the Giant Magellan Telescope: GMT, the Thirty Meter Telescope: TMT, the James Webb Space Telescope: JWST, and the Large Synoptic Survey Telescope: LSST). These forthcoming facilities and resources will undoubtedly advance our understanding in many fields of astronomy, among which the formation and evolution of galaxies is a high priority.

REFERENCES

Abramson L. E., Gladders M. D., Dressler A., Oemler Jr. A., Poggianti B., et al. 2015, ApJ, 801, 12

Allen S. W., & Fabian A. C. 1998, MNRAS, 297, 63

Andreani P., Cristiani S., Grazian A., La, Franca F., & Goldschmidt P. 2003, AJ, 125, 444

Arabadjis J. S., Bautz M. W., & Garmire G. P. 2002, ApJ, 572, 66

Arnold T. J., Martini P., Mulchaey J. S., Berti A., & Jeltema T. E. 2009, ApJ, 707, 1691

Arnouts S., Walcher C. J., Le Fèvre O., Zamorani G., Ilbert O., et al. 2007, A&A, 476, 137

Ashby M. L. N., Stern D., Brodwin M., Griffith R., Eisenhardt P., et al. 2009, ApJ, 701, 428

Atlee D. W., Martini P., Assef R. J., Kelson D. D., & Mulchaey J. S. 2011, ApJ, 729, 22

Avni Y., & Bahcall J. N. 1980, ApJ, 235, 694

Bai L., Rasmussen J., Mulchaey J. S., Dariush A., Raychaudhury S., et al. 2010, ApJ, 713, 637

Baldry I. K., Glazebrook K., Brinkmann J., Ivezić Ž., Lupton R. H., et al. 2004, ApJ, 600, 681

Baldry I. K., Glazebrook K., & Driver S. P. 2008, MNRAS, 388, 945

Baldry I. K., Driver S. P., Loveday J., Taylor E. N., Kelvin L. S., et al. 2012, MNRAS, 421, 621

Balestra I., Mainieri V., Popesso P., Dickinson M., Nonino M., et al. 2010, A&A, 512, 12

Bardeau S., Soucail G., Kneib J. P., Czoske O., Ebeling H., et al. 2007, A&A, 470, 449

Barmby P., Alonso-Herrero A., Donley J. L., Egami E., Fazio G. G., et al. 2006, ApJ, 642, 126

Barmby P., Huang J. S., Ashby M. L. N., Eisenhardt P. R. M., Fazio G. G., et al. 2008, ApJS, 177, 431

Behroozi P. S., Marchesini D., Wechsler R. H., Muzzin A., Papovich C., et al. 2013, ApJ, 777, 10

Bell E. F., 2003, ApJ, 586, 794

Bell E. F., Papovich C., Wolf C., Le Floc'h E., Caldwell J. A. R., et al. 2005, ApJ, 625, 23

Bell E. F., Zheng X. Z., Papovich C., Borch A., Wolf C., et al. 2007, ApJ, 663, 834

Bertin E., & Arnouts S. 1996, A&AS, 117, 393

Best P. N., van Dokkum P. G., Franx M., & Röttgering H. J. A. 2002, MNRAS, 330, 17

Blakeslee J. P., Franx M., Postman M., Rosati P., Holden B. P., et al. 2003, ApJ, 596, 143

Blakeslee J. P., Holden B. P., Franx M., Rosati P., Bouwens R. J., et al. 2006, ApJ, 644, 30

Blanton M. R., Lupton R. H., Schlegel D. J., Strauss M. A., Brinkmann J., et al. 2005, ApJ, 631, 208

Blanton M. R., & Roweis S. 2007, AJ, 133, 734

Bower R. G., Benson A. J., Malbon R., Helly J. C., Frenk C. S., et al. 2006, MNRAS, 370, 645

Bower R. G., Lucey J. R., & Ellis R. S. 1992, MNRAS, 254, 589

Bower R. G., McCarthy I. G., & Benson A. J. 2008, MNRAS, 390, 1399

Brammer G. B., Whitaker K. E., van Dokkum P. G., Marchesini D., Franx M., et al. 2011, ApJ, 739, 24

Brammer G. B., van Dokkum P. G., & Coppi P. 2008, ApJ, 686, 1503

Brinchmann J., Charlot S., White S. D. M., Tremonti C., Kauffmann G., et al. 2004, MNRAS, 351, 1151

Bruzual G., & Charlot S. 2003, MNRAS, 344, 1000

Calzetti D., 2000, ApJ, 533, 682

Capak P., Aussel H., Ajiki M., McCracken H. J., Mobasher B., et al. 2007a, ApJS, 172, 99

Capak P., Abraham R. G., Ellis R. S., Mobasher B., Scoville N., et al. 2007b, ApJS, 172, 284

Chabrier G. 2003, PASP, 115, 763

Chang Y. Y., van der Wel A., Rix H. W., Holden B., et al. 2013, ApJ, 773, 149

Chary R., & Elbaz D. 2001, ApJ, 556, 562

Chung S. M., Gonzalez A. H., Clowe D., Markevitch M., & Zaritsky D. 2010, ApJ, 725, 1536

Conroy C. 2013, ARA&A, 51, 393

Conroy C., Gunn J. E., & White M. 2009, ApJ, 699, 486

Cooray A. R., Grego L., Holzapfel W. L., Joy M., & Carlstrom J. E. 1998, AJ, 115, 1388

Courteau S., Cappellari M., de Jong R. S., Dutton A. A., & Emsellem E., et al. 2014, Reviews of Modern Physics 86, 47

Cowley M., et al. in preparation

Croton D. J., Springel V., White S. D. M., De Lucia G., Frenk C. S., et al. 2006, MNRAS, 365, 11

Czoske O., Kneib J. P., Soucail G., Bridges T. J., Mellier Y., et al. 2001, A&A, 372, 391

Czoske O., Moore B., Kneib J. P., & Soucail G. 2002, A&A, 386, 31

Dale D. A., & Helou G. 2002, ApJ, 576, 159

Davis M., Guhathakurta P., Konidaris N. P., Newman J. A., Ashby M. L. N., et al. 2007, ApJ, 660, 1

De Lucia G., Poggianti B. M., Aragón-Salamanca A., White S. D. M., Zaritsky D., et al. 2007, MNRAS, 374, 809

de Propris R., Stanford S. A., Eisenhardt P. R., Dickinson M., & Elston R. 1999, AJ, 118, 719

Demarco R., Rosati P., Lidman C., Homeier N. L., Scannapieco E., et al. 2005, A&A, 432, 381

Demarco R., Rosati P., Lidman C., Girardi M., Nonino M., et al. 2007, ApJ, 663, 164

Devriendt J. E. G., Guiderdoni B., & Sadat R. 1999, A&A, 350, 381

Doherty M., Bunker A. J., Ellis R. S., & McCarthy P. J. 2005, MNRAS, 361, 525

Dolphin A. E., Saha A., Skillman E. D., et al. 2003, AJ, 126, 187

Domínguez ánchez H., Pozzi F., Gruppioni C., et al., 201,MNRAS, 417, 900

Donahue M., Voit G. M., Scharf C. A., Gioia I. M., Mullis C. R., et al. 1999, ApJ, 527, 525

Donahue M., Gaskin J. A., Patel S. K., Joy M., Clowe D., et al. 2003, ApJ, 598, 190

Donley J. L., Rieke G. H., Pérez-González P. G., & Barro G. 2008, ApJ, 687, 111

Dressler A., & Shectman S. A. 1988, AJ, 95, 985

Dressler A., Oemler Jr. A., Couch W. J., Smail I., Ellis R. S., et al. 1997, ApJ, 490, 577

Drory N., & Alvarez M. 2008, ApJ, 680, 41

Drory N., Bundy K., Leauthaud A., Scoville N., Capak P., et al. 2009, ApJ, 707, 1595

Duc P. A., Poggianti B. M., Fadda D., Elbaz D., Flores H., et al. 2002, A&A, 382, 60

Dunne L., Ivison R. J., Maddox S., et al. 2009, MNRAS, 394, 3

Dye S., Taylor A. N., Thommes E. M., Meisenheimer K., Wolf C., et al. 2001, MNRAS, 321, 685

Eastman J., Martini P., Sivakoff G., Kelson D. D., Mulchaey J. S., et al. 2007, ApJ, 664, 9

Eckart M. E., McGreer I. D., Stern D., Harrison F. A., & Helfand D. J. 2010, ApJ, 708, 584

Eisenhardt P. R., Stern D., Brodwin M., Fazio G. G., Rieke G. H., et al. 2004, ApJS, 154, 48

Elbaz D., Dickinson M., Hwang H. S., Díaz-Santos T., Magdis G., et al. 2011, A&A, 533, 119

Elvis M., Wilkes B. J., McDowell J. C., Green R. F., Bechtold J., et al. 1994, ApJS, 95, 1

Fabian A. C., 2012, ARA&A, 50, 455

Fabricant D., Franx M., & van Dokkum P. 2000, ApJ, 539, 577

Farouki R., & Shapiro S. L. 1981, ApJ, 243, 32

Fasano G., Poggianti B. M., Couch W. J., Bettoni D., Kjaergaard P., & Moles M. 2000, ApJ, 542, 673

Fazio G. G., Hora J. L., Allen L. E., Ashby M. L. N., Barmby P., et al. 2004, ApJS, 154, 10

Fioc M., & Rocca-Volmerange B. 1997, A&A, 326, 950

Fisher D., Fabricant D., Franx M., & van Dokkum P. 1998, ApJ, 498, 195

Fontanot F., Pasquali A., De Lucia G., van den Bosch F. C., Somerville R. S., et al. 2011, MNRAS, 413, 957

Fumagalli M., Labbé I., Patel S. G., Franx M., van Dokkum P., et al. 2014, ApJ,

796, 35

Gabor J. M., Davé R., Finlator K., & Oppenheimer B. D. 2010, MNRAS, 407, 749

Galametz A., Stern D., Eisenhardt P. R. M., Brodwin M., Brown M. J. I., et al. 2009, ApJ, 694, 1309

Gandhi P., Horst H., Smette A., Hönig S., Comastri A., et al. 2009, A&A, 502, 457

Geha M., Blanton M. R., Yan R., & Tinker J. L. 2012, ApJ, 757, 85

Gehrels N. 1986, ApJ, 303, 336

Giacconi R., Zirm A., Wang J., Rosati P., Nonino M., et al. 2002, ApJS, 139, 369

Gilbank D. G., Bower R. G., Glazebrook K., Balogh M. L., Baldry I. K., et al. 2011, MNRAS, 414, 304

Gilmour R., Gray M. E., Almaini O., Best P., Wolf C., et al. 2007, MNRAS, 380, 1467

Griffith R. L., & Stern D. 2010, AJ, 140, 533

Grogin N. A., Kocevski D. D., Faber S. M., Ferguson H. C., Koekemoer A. M., et al. 2011, ApJS, 197, 35

Gunn J. E, & Gott III J. R 1972, ApJ, 176, 1

Häring N., & Rix H. W., 2004, ApJL, 604, 89

Hart Q. N., Stocke J. T., & Hallman E. J. 2009, ApJ, 705, 854

Heavens A., Panter B., Jimenez R., & Dunlop J. 2004, Nature, 428, 625

Henriques B., White S., Thomas P., et al. 2014, ArXiv e-prints, arXiv:1410.0365

Hickox R. C., Jones C., Forman W. R., Murray S. S., Brodwin M., et al. 2007, ApJ, 671, 1365

Hickox R. C., Jones C., Forman W. R., Murray S. S., Kochanek C. S., et al. 2009, ApJ, 696, 891

Hilton M., Lloyd-Davies E., Stanford S. A., Stott J. P., Collins C. A., et al. 2010, ApJ, 718, 133

Hoekstra H., Franx M., Kuijken K., & Squires G. 1998, ApJ, 504, 636

Hogg D. W., Blanton M. R., Eisenstein D. J., Gunn J. E., Schlegel D. J., et al. 2003, ApJ, 585, 5

Hogg D. W., Blanton M. R., Brinchmann J., Eisenstein D. J., Schlegel D. J., et al. 2004, ApJ, 601, 29

Holden B. P., Illingworth G. D., Franx M., Blakeslee J. P., Postman M., et al. 2007, ApJ, 670, 190

Hopkins P. F., & Hernquist L. 2006, ApJS, 166, 1

Hopkins P. F., Hickox R., Quataert E., Hernquist L. 2009, MNRAS, 398, 333

Ilbert O., Salvato M., Le Floch E., et al. 2010, ApJ, 709, 644

Ilbert O., McCracken H. J., Le Fèvre O., Capak P., Dunlop J., et al. 2013, A&A, 556, 55

Jee M. J., White R. L., Benítez N., Ford H. C., Blakeslee J. P., et al. 2005, ApJ, 618, 46

Jee M. J., White R. L., Ford H. C., Blakeslee J. P., Illingworth G. D., et al. 2005, ApJ, 634, 813

Johnson O., Best P. N., & Almaini O. 2003, MNRAS, 343, 924

Karim A., Schinnerer E., Martínez-Sansigre A., et al. 2011, ApJ, 730, 61

Kawinwanichakij L., Papovich C., Quadri R. F., Tran K.-V. H., Spitler L. R., et al. 2014, ApJ, 792, 103

Kelson D. D. 2014, ArXiv e-prints, arXiv:1406.5191

Kneib J. P., Hudelot P., Ellis R. S., Treu T., Smith G. P., et al. 2003, ApJ, 598, 804

Kocevski D. D., Lubin L. M., Lemaux B. C., Gal R. R., Fassnacht C. D., et al. 2009, ApJ, 703, 33

Koekemoer A. M., Faber S. M., Ferguson H. C., Grogin N. A., Kocevski D. D., et al. 2011, ApJS, 197, 36

Kriek M., van Dokkum P. G., Labbé I., Franx M., Illingworth G., et al. 2009, ApJ, 700, 221

Kuraszkiewicz J. K., Wilkes B. J., Hooper E. J., McLeod K. K., Wood K., et al. 2003, ApJ, 590, 128

Labbé I., Huang J., Franx M., Rudnick G., Barmby P., et al. 2005, ApJ, 624, 81

Labbé I., Bouwens R., Illingworth G. D., & Franx M. 2006, ApJ, 649, 67

Lacy M., Storrie-Lombardi L. J., Sajina A., Appleton P. N., Armus L., et al. 2004, ApJS, 154, 166

Lacy M., Wilson G., Masci F., Storrie-Lombardi L. J., Appleton P. N., et al. 2005, ApJS, 161, 41

Lacy M., Petric A. O., Sajina A., Canalizo G., Storrie-Lombardi L. J., et al. 2007, AJ, 133, 186

Lagos C. D. P., Cora S. A., & Padilla N. D. 2008, MNRAS, 388, 587

Lawrence A., Warren S. J., Almaini O., Edge A. C., Hambly N. C., et al. 2007, MNRAS, 379, 1599

Lee N., Sanders D. B., Casey C. M., Toft S., Scoville N. Z., et al. 2015, ApJ, 801, 80

Le Fèvre O., Vettolani G., Garilli B., Tresse L., Bottini D., et al. 2005, A&A, 439, 845

Leitner S. N. 2012, ApJ, 745, 149

Leja J., van Dokkum P. G., Momcheva I., Brammer G., Skelton R. E., et al. 2013, ApJ, 778, 24

Leja J., van Dokkum P. G., Franx M., & Whitaker K. E. 2015, ApJ, 798, 115

Li C. & White S. D. M., 2009, MNRAS, 398, 2177

Lilly S. J., Le Brun V., Maier C., et al. 2009, ApJS, 184, 218

Lombardi M., Rosati P., Blakeslee J. P., Ettori S., Demarco R., et al. 2005, ApJ, 623, 42

Lotz J. M., Jonsson P., Cox T. J., et al. 2011, ApJ, 742, 103

Lubin L. M., Gal R. R., Lemaux B. C., Kocevski D. D., & Squires G. K. 2009, AJ, 137, 4867

Lutz D., Poglitsch A., Altieri B., et al. 2011, A&A, 532, 90

Lutz D., Maiolino R., Spoon H. W. W., & Moorwood A. F. M. 2004, A&A, 418, 465

Madau P., & Dickinson M. 2014, ARA&A, 52, 415

Mahajan S., Haines C. P., & Raychaudhury S. 2010, MNRAS, 404, 1745

Makovoz D., Roby T., Khan I., & Booth H. 2006, ApJ, 6274, 673

Mancone C., & Gonzalez A. 2012, MNRAS, 398, 2177

Maraston C. 2005, MNRAS, 362, 799

Marchesini D., van Dokkum P. G., Förster, Schreiber N. M., Franx M., et al. 2009, ApJ, 701, 1765

Marchesini D., Whitaker K. E., Brammer G., et al. 2010, ApJ, 725, 1277

Martel A. R., Menanteau F., Tozzi P., Ford H. C., & Infante L. 2007, ApJS, 168, 19

Martini P., Mulchaey J. S., & Kelson D. D. 2007, ApJ, 664, 761

Martini P., Sivakoff G. R., & Mulchaey J. S. 2009, ApJ, 701, 66

McCarthy I. G., Schaye J., Ponman T. J., Bower R. G., Booth C. M., et al. 2010, MNRAS, 406, 822

McCracken H. J., Milvang-Jensen B., Dunlop J., Franx M., Fynbo J. P. U., et al. 2012, A&A, 544, 156

Merloni A. & Heinz S. 2008, MNRAS, 388, 1011

Messias H., Afonso J., Salvato M., Mobasher B., & Hopkins A. M. 2012, ApJ, 754, 120

Michard R., & Andreon S. 2008, A&A, 490, 923

Mobasher B., Bridges T. J., Carter D., Poggianti B. M., Komiyama Y., et al. 2001, ApJS, 137, 279

Molnar S. M., Hughes J. P., Donahue M., & Joy M. 2002, ApJ, 573, 91

Moran S. M., Ellis R. S., Treu T., Smail I., Dressler A., et al. 2005, ApJ, 634, 977

Moran S. M., Ellis R. S., Treu T., Smith G. P., Rich R. M., et al. 2007a, ApJ, 671, 1503

Moran S. M., Miller N., Treu T., Ellis R. S., & Smith G. P. 2007b, ApJ, 659, 1138

Moster B. P., Naab T., & White S. D. M. 2013, MNRAS, 428, 3121

Moster B. P., Somerville R. S., Newman J. A., & Rix H. W. 2011, ApJ, 731, 113

Moustakas J., Coil A. L., Aird J., Blanton M. R., Cool R. J., et al. 2013, ApJ, 767, 50

Muzzin A., Wilson G., Lacy M., Yee H. K. C., Stanford S. A. 2008, ApJ, 686, 966

Muzzin A., van Dokkum P., Kriek M., et al. 2010, ApJ, 725, 742

Muzzin A., Marchesini D., Stefanon M., Franx M., McCracken H. J., et al. 2013, ApJ, 777, 18

Nelson D., Pillepich A., Genel S., et al. 2015, ArXiv e-prints, arXiv:1504.00362

Noeske K. G., Weiner B. J., Faber S. M., Papovich C., Koo D. C., et al. 2007, ApJ, 660, 43

Nomoto K., Kobayashi C., & Tominaga N. 2013, ARA&A, 51, 457

Papovich C., Cool R., Eisenstein D., Le Floc'h E., Fan X., et al. 2006, AJ, 132, 231

Papovich C., Moustakas L. A., Dickinson M., Le Floc'h E., Rieke G. H., et al. 2006, ApJ, 640, 92

Papovich C., Rudnick G., Floch E. L., et al. 2007, ApJ, 668, 45

Papovich C., Finkelstein S. L., Ferguson H. C., Lotz J. M., & Giavalisco M. 2011, MNRAS, 412, 1123

Papovich C., Labbé I., Quadri R., Tilvi V., Behroozi P., et al. 2014, ArXiv e-prints, arXiv:1412.3806

Park S. Q., Barmby P., Willner S. P., Ashby M. L. N., Fazio G. G., et al. 2010, ApJ, 717, 118

Patel S. G., Fumagalli M., Franx M., van Dokkum P. G., van der Wel A., et al. 2013,

ApJ, 778, 115

Patel S. G., Holden B. P., Kelson D. D., Franx M., van der Wel A., et al. 2012, ApJ, 748, 27

Peng Y. J., Lilly S. J., Kovač K., Bolzonella M., Pozzetti L., et al. 2010, ApJ, 721, 193

Peng Y. J., Lilly S. J., Renzini A., & Carollo M. 2012, ApJ, 757, 4

Pérez-González P. G., Rieke G. H., Villar V., Barro G., Blaylock M., et al. 2008, ApJ, 675, 234

Persson S. E., Murphy D. C., Smee S., Birk C., Monson A. J., et al. 2013, PASP, 125, 654

Pier E. A., & Krolik J. H. 1992, ApJ, 401, 99

Pilbratt G. L., Riedinger J. R., Passvogel T., et al. 2010, A&A, 518, 1

Planck Collaboration 2015, ArXiv e-prints, arXiv:1502.01589

Polletta M., Tajer M., Maraschi L., Trinchieri G., Lonsdale C. J., et al. 2007, ApJ, 663, 81

Popesso P., Dickinson M., Nonino M., Vanzella E., Daddi E., et al. 2009, A&A, 494, 443

Postman M., Franx M., Cross N. J. G., Holden B., Ford H. C., et al. 2005, ApJ, 623, 721

Pozzetti L., Bolzonella M., Zucca E., Zamorani G., Lilly S., et al. 2010, A&A, 523, 13

Puchwein E., Sijacki D., & Springel V. 2008, ApJ, 687, 53

Quadri R. F., & Williams R. J. 2010, ApJ, 725, 794

Quadri R. F., Williams R. J., Franx M., & Hildebrandt H. 2012, ApJ, 744, 88

Reach W. T., Megeath S. T., Cohen M., Hora J., Carey S., et al. 2005, PASP, 117, 978

Reddy N. A., & Steidel C. C. 2009, ApJ, 692, 778

Renzini A. 2009, MNRAS, 398, 58

Richstone D. O. 1976, ApJ, 204, 642

Rines K., Geller M. J., Kurtz M. J., & Diaferio A. 2003, AJ, 126, 2152

Rodighiero G., Cimatti A., Gruppioni C., et al. 2010, A&A, 518, 25

Rosati P., Tozzi P., Ettori S., Mainieri V., Demarco R., et al. 2004, AJ, 127, 230

Rudnick G., von der Linden A., Pelló R., Aragón-Salamanca A., Marchesini D., et

al. 2009, ApJ, 700, 1559

Saintonge A., Tran K.-V. H., & Holden B. P. 2008, ApJ, 685, 113

Salim S., Rich R. M., Charlot S., Brinchmann J., Johnson B. D., et al. 2007, ApJS, 173, 267

Sandage A., & Visvanathan N. 1978, ApJ, 223, 707

Sandage A., Tammann G. A., & Yahil A. 1979, ApJ, 232, 352

Sanders D. B., Phinney E. S., Neugebauer G., Soifer B. T., & Matthews K. 1989, ApJ, 347, 29

Santini P., Fontana A., Grazian A., Salimbeni S., Fontanot F., et al. 2012, A&A, 538, 33

Schechter P. 1976, ApJ, 203, 297

Schreiber C., Pannella M., Elbaz D., Béthermin M., Inami H., et al. 2015, A&A, 575, 74

Silk J. 2013, ApJ, 772, 112

Simpson C., Rawlings S., Ivison R., Akiyama M., Almaini O., et al. 2012, MNRAS, 421, 3060

Smail I., Sharp R., Swinbank A. M., Akiyama M., Ueda Y., et al. 2008, MNRAS, 389, 407

Sparre M., Hayward C. C., Springel V., et al. 2015, MNRAS, 447, 3548

Speagle J. S., Steinhardt C. L., Capak P. L., & Silverman J. D. 2014, ApJS, 214, 15

Stern D., Eisenhardt P., Gorjian V., Kochanek C. S., Caldwell N., et al. 2005, ApJ, 631, 163

Stott J. P., Smail I., Edge A. C., Ebeling H., Smith G. P., et al. 2007, ApJ, 661, 95

Szokoly G. P., Bergeron J., Hasinger G., Lehmann I., Kewley L., et al. 2004, ApJS, 155, 271

Tasca L. A. M., Le Fèvre O., Hathi N. P., et al. 2014, ArXiv e-prints, arXiv:1411.5687

Teyssier R., Moore B., Martizzi D., Dubois Y., & Mayer L. 2011, MNRAS, 414, 195

Thomas D., Maraston C., Bender R., & Mendes de Oliveira C. 2005, ApJ, 621, 673

Thompson G. D., Levenson N. A., Uddin S. A., & Sirocky M. M. 2009, ApJ, 697, 182

Tomczak A. R., Quadri R. F., Tran K.-V. H., Labbé I., Straatman C. M. S., et al. 2014, ApJ, 783, 85

Tran K.-V. H., van Dokkum P., Franx M., Illingworth G. D., Kelson D. D., et al.

2005a, ApJ, 627, 25

Tran K.-V. H., van Dokkum P., Illingworth G. D., Kelson D., Gonzalez A., et al. 2005b, ApJ, 619, 134

Tran K.-V. H., Franx M., Illingworth G. D., van Dokkum P., Kelson D. D., et al. 2007, ApJ, 661, 750

Tran K.-V. H., Papovich C., Saintonge A., Brodwin M., Dunlop J. S., et al. 2010, ApJ, 719, 126

Treu T., Ellis R. S., Kneib J. P., Dressler A., Smail I., et al. 2003, ApJ, 591, 53

Trump J. R., Impey C. D., Elvis M., et al. 2009, ApJ, 696, 1195

Urry C. M., & Padovani P., 1995, PASP, 107, 803

van Dokkum P. G., Franx M., Kelson D. D., Illingworth G. D., Fisher D., et al. 1998, ApJ, 500, 714

van Dokkum P. G., Labbé I., Marchesini D., Quadri R., Brammer G. B., et al. 2009, PASP, 121, 2

van Dokkum P. G., Whitaker K. E., Brammer G., Franx M., Kriek M., et al. 2010, ApJ, 709, 1018

Vanzella E., Cristiani S., Dickinson M., Giavalisco M., Kuntschner H., et al. 2008, A&A, 478, 83

Verdugo T., de Diego J. A., & Limousin M. 2007, ApJ, 664, 702

Viero M. P., Moncelsi L., Quadri R. F., Arumugam V., Assef R. J., et al. 2013, ApJ, 779, 32

Weinmann S. M., Pasquali A., Oppenheimer B. D., Finlator K., Mendel J. T., et al. 2012, MNRAS, 426, 2797

Werner M. W., Roellig T. L., Low F. J., Rieke G. H., Rieke M., et al. 2004, ApJS, 154, 1

Whitaker K. E., Labbé I., van Dokkum P. G., Brammer G., Kriek M., et al. 2011, ApJ, 735, 86

Whitaker K. E., van Dokkum P. G., Brammer G., & Franx M. 2012, ApJ, 754, 29

Whitaker K. E., Franx M., Leja J., van Dokkum P. G., Henry A., et al. 2014, ApJ, 795, 104

Williams R. J., Quadri R. F., & Franx M. 2011, ApJ, 738, 25

Williams R. J., Quadri R. F., Franx M., van Dokkum P., & Labbé I. 2009, ApJ, 691, 1879

Wuyts S., Labbé I., Franx M., Rudnick G., van Dokkum P., et al. 2007, ApJ, 655,

51

Wuyts S., Labbé I., Schreiber N. M. F., Franx M., Rudnick G., et al. 2008, ApJ, 682, 985

Wuyts S., Förster Schreiber N. M., Lutz D., et al. 2011, ApJ, 738, 106

Zhang F., Han Z., Li L., & Hurley J. R. 2004, MNRAS, 350, 710

Zhang Y. Y., Böhringer H., Mellier Y., Soucail G., & Forman W. 2005, A&A, 429, 85